

POLITECNICO DI TORINO

---

Corso di Laurea Magistrale in Ingegneria Aerospaziale

Tesi di Laurea Magistrale

Development of a Schlieren System  
for a Mobile Rocket Combustion Chamber



Relatore:

Prof. DARIO G. PASTRONE

Candidato:

GIUSEPPE SCARLATELLA

s231906

---

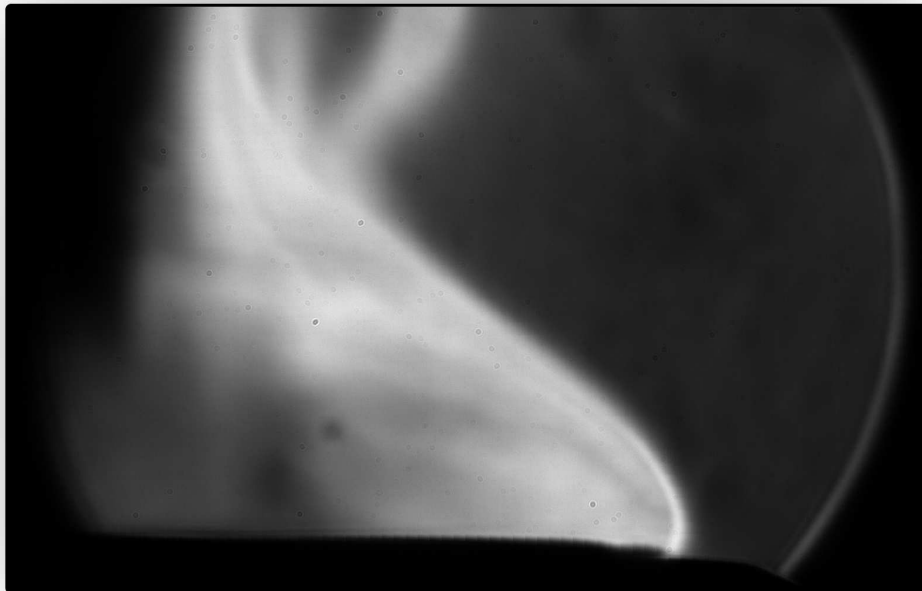
A.A. 2018/19



POLITECNICO DI TORINO

IN COLLABORATION WITH TECHNISCHE UNIVERSITÄT MÜNCHEN

# DEVELOPMENT OF A SCHLIEREN SYSTEM FOR A MOBILE ROCKET COMBUSTION CHAMBER



GIUSEPPE SCARLATELLA

February 25, 2019

# Abstract

The optical system has been developed in order to investigate a mobile rocket combustion chamber through schlieren technique. The design process has been presented in a consecutive perspective, despite of the non-sequentiality that characterizes any decision-making route, in order to facilitate the reading. A brief introduction to the combustion chamber test bench, as well as to the rising interest of space industry and agencies in green propellants, is promptly followed by theoretical background about schlieren technique and its application in an optical diagnostic perspective. It is also presented a computational method for numerical evaluation, implemented in a Matlab<sup>®</sup> routine for image-processing.

The project design develops from studies on conventional and novel configurations up to detail design and optimization, including in the process also cost-benefits analysis for the selection of components, Matlab<sup>®</sup> routines for sizing and verification purposes, as well as developing of a complete CAD model as a tool for calibration procedures. Indeed, it is offered a step-by-step calibration procedure to the operator, that includes a specific section dedicated to most common practical issues and alternative solutions. The design process ends up by drafting a brief list of possible improvements in order to increase its reliability for future applications.

A brief summary of main results, coming from a preliminary test session on a flat flame burner, is offered to the reader, in order to outline a standard setting for a correct calibration of the system. A specific test campaign aims to highlight the optical system sensitivity to changes in temperature and density due to mixture ratio variations.

# Acknowledgement

The accomplishment of this project would not have been possible without the efforts of our workforce from Politecnico and the sturdy network that they built over the years with TUM. This gave me the opportunity to face new challenges, deal with stimulating projects and meet wonderful colleagues. Special mentions go to Fernanda Winter for her endorsement and unquestioned trust, to prof. Pastrone for his openness and confidence, and to the talented colleagues from Politecnico for their contribution and passion.

The warmest gratitude goes to my family, that supported me all over my experience in Turin and Munich, the most stimulating and challenging years to me until today. We faced every difficulty together, like an unbreakable core, sharing every joyful moment like a milestone for something bigger to come. I sincerely hope you can see this like the first instalment of my boundless gratefulness.

The closing thanks goes to a special person who believed in a fragile promise that today holds stronger than ever, who stood by my side during the toughest moments, feeding me with patience and love. This defining achievement evenly belongs to both of us.

# Contents

<b>1</b>	<b>Introduction</b>	<b>1</b>
<b>2</b>	<b>Theoretical Background</b>	<b>3</b>
2.1	Basic Concepts . . . . .	3
2.2	Schlieren Technique . . . . .	7
2.2.1	Illuminance . . . . .	9
2.2.2	Contrast & Sensitivity . . . . .	11
2.3	Resolutive Algorithm . . . . .	13
2.4	Computational Implementation . . . . .	16
2.4.1	Study of Variables and Boundary Conditions . . . . .	17
2.4.2	Integration Method . . . . .	19
2.4.3	Window Correction . . . . .	20
<b>3</b>	<b>Project Design</b>	<b>23</b>
3.1	Conceptual Design . . . . .	23
3.1.1	Conventional and Novel Configurations . . . . .	23
3.1.2	Project Requirements . . . . .	28
3.2	Preliminary Design . . . . .	30
3.2.1	List of Components . . . . .	30
3.2.2	Cost Analysis . . . . .	40
3.2.3	Sizing . . . . .	42
3.3	Detail Design . . . . .	44
3.3.1	<i>Tilt Angle</i> Optimization . . . . .	44
3.3.2	CAD Model . . . . .	47
3.3.3	<i>Matlab® Image Analysis Routine</i> . . . . .	48
3.4	Future Improvements . . . . .	50
<b>4</b>	<b>Experimental Setup</b>	<b>54</b>
4.1	Calibration Procedures . . . . .	54

---

4.1.1	Basic Calibration . . . . .	54
4.1.2	Advanced Calibration . . . . .	61
4.2	Practical Issues . . . . .	65
<b>5</b>	<b>Test Sessions</b>	<b>73</b>
5.1	Test Bench Arrangement . . . . .	73
5.1.1	Schlieren Optical System . . . . .	73
5.1.2	Flat Flame McKenna Burner . . . . .	74
5.1.3	Feed System and Sequence Definition . . . . .	75
5.2	Test Campaign for System Calibration . . . . .	77
5.2.1	Common Inputs . . . . .	77
5.2.2	Cut-Off Amount Regulation . . . . .	81
5.2.3	Shutter Speed Setting . . . . .	83
5.2.4	Window Test Sessions . . . . .	84
5.3	Test Campaign for Flame Study . . . . .	87
	<b>References</b>	<b>96</b>
<b>A</b>	<b>Matlab<sup>®</sup> Image Analysis Routine</b>	<b>100</b>
A.1	Program Structure Tree . . . . .	101
A.2	Flow-field Models . . . . .	103
<b>B</b>	<b>Technical Drawings</b>	<b>104</b>
<b>C</b>	<b>Components List</b>	<b>109</b>

# List of Figures

1.1	<i>Technological Foundations for the Design of Thermally and Mechanically Highly Loaded Components of Future Space Transportation Systems</i> joint research center. . . . .	1
1.2	<i>Mobile Rocket Combustion Chamber Test Bench</i> (MoRaP) CAD model, latest version by S.A. Artene, special thanks to M.Sc. F. Winter. . . . .	2
2.1	Picture made by the Schlieren method, shows a bullet travelling through the air above two candle flames [55]. . . . .	3
2.2	Diagram of elemental light refraction by a refractive-index gradient $dn/dy$ [34, p.339]. . .	5
2.3	Two famous images by Hubert Schardin [32]. <b>a</b> Schlieren photo of a bullet and a candle-flame. <b>b</b> Shadowgram of shockwave diffraction around a triangular block. . . . .	7
2.4	Diagram of parallel-light <i>direct shadowgraph</i> observation of a dense spherical schliere [34, p.31]. . . . .	7
2.5	General arrangement for schlieren imaging. Enlarged regions within circles illustrate deflection by the rays at the boundary between two refractive indices and the resultant blocking of the deflected rays by the aperture. Note that for clarity this schematic drawing shows only a single beam being refracted, while in reality all beams passing through the jet would experience refraction [17]. . . . .	8
2.6	Diagram of a simple schlieren system with an extended light source [34, p.34]. . . . .	9
2.7	Schematic drawing of the path of the light beam in a schlieren system made of lenses [28, p.30]. . . . .	9
2.8	Knife-edge plane for a rectangular source image at 50% cut-off, with height $a$ remaining unobscured. Due to refraction in the test area, a weak elemental source image is shifted. Its unobscured height, $a + \Delta a$ , passes extra light to a corresponding point in the schlieren image [34, p.36]. . . . .	10
2.9	Illuminance ratio $E/E_0$ vs. %cutoff and experimental data for various $E_0$ [34, p.50]. . . .	10
2.10	View of undisturbed and deflected light beam cross-sections at the knife-edge of a schlieren system [28, p.30]. . . . .	12
2.11	Pictures reporting <i>mean values</i> relative to a test campaign on a <i>candle test</i> , carried out in laboratory by the author and post-processed by a Matlab® Image Analysis routine. . . .	16
2.12	View from above of an " <i>AllDomain</i> " flow-field model. . . . .	17
2.13	View from above of an example of a " <i>Diamond</i> " flow-field model. . . . .	18
2.14	Pictures reporting <i>mean values</i> relative to a test campaign on a <i>candle test</i> , carried out in laboratory by the author. The Eq.2.24 and Eq.2.25 have been solved by adopting Matlab® routines for differential equations, more specifically ode45 and ode15s. . . . .	20

2.15	Geometrical construction scheme of light beam path altered by presence of a window [28, p.34]. . . . .	21
3.1	Dual-field-lens schlieren arrangement [33][34, p.41]. . . . .	24
3.2	Z-type schlieren arrangement [32][33][34, p.42]. . . . .	25
3.3	Z-type 2-parabolic-2-flat-mirrors schlieren arrangement [28, p.25]. . . . .	25
3.4	Two single-mirror possible arrangements [34, p.47]. . . . .	26
3.5	Diagram of Schardin's schlieren method no. 4, the lens-and-grid technique [34, p.89]. . . . .	26
3.6	Typical BOS scheme. An optical ray passes through a phase object and its displacement is compared with the undistorted imaging ray [28, p.37]. . . . .	27
3.7	BOS installation in ACS, the camera views the background image on the monitor through the nitrogen gas simulated rocket exhaust plume [49]. . . . .	27
3.8	Parallel beam shadow of a flame illustrating diffraction effects obtained by a laser source [26]. . . . .	28
3.9	Example of a possible fully-functional <i>Z-type 2-parabolic-2-flat-mirror schlieren system</i> configuration, designed for quantitative-evaluation of refractive-index variations. . . . .	29
3.10	<i>Light Source Block</i> CAD model. . . . .	30
3.11	A scheme of the light source block [34, p.173]. . . . .	31
3.12	Detail of the Light Source Block CAD model. Starting from the left, we find the <i>LED lamp</i> , the <i>light-amount regulator</i> , the <i>condenser lens</i> and the widened <i>source slit</i> . . . . .	32
3.13	20DC1000ER.1 concave mirror reflectance (%) vs. wavelength ( $\mu m$ ) [23]. . . . .	33
3.14	<i>1ST concave mirror support</i> (left) and <i>2ND concave mirror support</i> (right) CAD models. . . . .	34
3.15	<i>Actual</i> (left) and <i>future</i> (right) <i>flat mirror setups</i> , CAD models. . . . .	34
3.16	<i>Camera Block</i> CAD model. . . . .	35
3.17	Preliminary concept (left) and definitive version (right) of the <i>knife-edge filter</i> , CAD models. . . . .	36
3.18	<i>Tangential focus</i> in a Z-type schlieren system, horizontal smearing of a rectangular source image while applying a horizontal knife-edge filter for vertical evaluations [34, p.45]. . . . .	37
3.19	Diagram of 2ND mirror field, notations for <i>magnification factor</i> and focusing lens [34, p.73]. . . . .	38
3.20	Pictures of the components for the camera setup. . . . .	39
3.21	Effect of an <i>extension tube</i> on overall FL [9]. . . . .	40
3.22	Isometric view of the MoRaP ( <i>previous version</i> ), special thanks to M.Sc. F. Winter. . . . .	42
3.23	CAD models from the <i>schlieren system</i> aluminium rail structure. . . . .	42
3.24	CAD models from the definitive <i>schlieren system</i> . . . . .	43
3.25	Regulation excursion ( $\pm 155.5 mm$ ) of the <i>mounting brackets</i> , CAD model. . . . .	43
3.26	Point of double passage of light in the striation region [1]. . . . .	44
3.27	Preliminary configurations through <i>commercial basic</i> (a) and <i>freeware</i> (b) software. . . . .	46
3.28	Multiple views from the CAD model of the definitive system configuration. . . . .	47
3.29	A <i>Quick User Guide</i> is within the program folder, available for the end user. . . . .	48
3.30	User interface of main functions from <i>Matlab® Image Analysis Routine</i> . . . . .	49
4.1	Schlieren system just after the <i>basic calibration</i> procedure, photo by the author. . . . .	60
4.2	<i>Distance</i> of the 1ST Concave Mirror from the clamping carrier (1) and mounting bracket <i>height</i> (2). . . . .	61
4.3	Updating the <i>alignment distance</i> for right block on CAD Model. . . . .	62

4.4	<i>Distance of the 2ND Concave Mirror from the clamping carrier (1) and mounting bracket height (2).</i> . . . . .	63
4.5	Effect on the schlieren image of knife-edge displacement along the optical axis for a horizontal knife-edge entering the beam from below. <b>a</b> knife-edge too close to mirror, <b>b</b> correct adjustment, <b>c</b> knife-edge too far from mirror [34, p.181]. . . . .	68
4.6	<b>(a)</b> 95% cut-off, revealing diffraction "shadows", <b>(b)</b> 100% cut-off reverses the diffraction shadow illumination [34, p.69]. . . . .	69
4.7	Examples of $f/no.$ for the lens aperture [42]. . . . .	70
4.8	Pictures of a shock-wave boundary-layer at Mach 3 [34, p.190]. The turbulence seen in <b>(a)</b> ( $1\mu s$ shutter speed) is mostly optical noise from wind-tunnel side-wall boundary-layers, and is completely averaged out in frame <b>(b)</b> ( $10ms$ shutter speed). . . . .	71
5.1	Test bench for the <i>system calibration</i> and <i>flame study</i> campaigns. . . . .	73
5.2	<i>McKenna flat flame standard bronze burner</i> with standard shroud ring, photo by the author. . . . .	74
5.3	<i>McKenna flat flame burner</i> , technical specs [10] and example of flow conditions [4] for air/ $GCH_4$ mixture. . . . .	74
5.4	Example of a <i>T junction</i> along the feed lines, photo by the author. . . . .	75
5.5	Sequence before <b>(a)</b> and after the ignition, showing the blasting and anchoring of the flame at $O/F = 2.2$ , captured by the author. . . . .	76
5.6	Output from <i>Matlab<sup>®</sup> Image Analysis Routine</i> on the $O/F = 2.2$ sequence in Fig.5.5. . . . .	76
5.7	1ST concave mirror arrangement, photo by the author. . . . .	77
5.8	Pictures representing the area evaluated by <i>Matlab<sup>®</sup> Image Analysis Routine</i> for a corresponding $1000 \times 1000px$ portion of raw pictures. . . . .	78
5.9	Different options for flow-field modelling by <i>Matlab<sup>®</sup> Image Analysis Routine</i> . . . . .	79
5.10	Pictures for comparative evaluations between two knife-edge filter configurations with different <i>cut-off amounts</i> . . . . .	81
5.11	<i>Contrast</i> mean values for the entire sequence, comparative between two knife-edge filter configurations with different cut-off amounts. . . . .	82
5.12	<i>Average temperature along x-axis</i> , comparative between two knife-edge filter configurations with different cut-off amounts. . . . .	82
5.13	Pictures for comparative evaluations between two different <i>shutter speed</i> setting. . . . .	83
5.14	<i>Average temperature along x-axis</i> , comparative between two different <i>shutter speed</i> setting. . . . .	83
5.15	Synthetic fused silica glass SQ1 model by Sico <sup>®</sup> Technology GmbH. . . . .	84
5.16	Example of a <i>window-on</i> arrangement, photo by the author. . . . .	85
5.17	<i>Contrast</i> mean values, comparative between <i>window-off</i> and <i>windows-on</i> solutions with no alteration in input data. . . . .	85
5.18	Comparative evaluation on <i>average temperature along x-axis</i> for different window configuration, in <b>(c)</b> an example of computational correction for windows by <i>Matlab<sup>®</sup> routine</i> . . . . .	86
5.19	Blasting and anchorage of the flame at $O/F = 2.2$ , captured by the author. . . . .	87
5.20	Blasting and anchorage of the flame at $O/F = 3.0$ , captured by the author. . . . .	88
5.21	Blasting and anchoring of the flame at $O/F = 3.4$ , captured by the author. . . . .	88
5.22	Comparative evaluation on <i>average brightness</i> for different $O/F$ . . . . .	89
5.23	Comparative evaluation on <i>average contrast</i> for different $O/F$ . . . . .	89
5.24	Comparative evaluation on <i>average density</i> for different $O/F$ . . . . .	90

5.25	Comparative evaluation on <i>average density along x-axis</i> for different O/F. . . . .	90
5.26	Comparative evaluation on <i>average temperature</i> for different O/F. . . . .	91
5.27	Comparative evaluation on <i>average temperature along x-axis</i> for different O/F. . . . .	91
5.28	Comparative evaluation on <i>average density gradient</i> for different O/F. . . . .	92
5.29	Comparative evaluation on <i>average temperature shape</i> for different O/F by <i>thresholding</i> post-processing technique. . . . .	92
5.30	Comparative between flame inclination angles (in average) for $O/F = 2.2$ <b>(a)</b> and $O/F =$ $3.0$ <b>(b)</b> respectively. . . . .	94
A.1	Pictures covering 6 types of flow-field models included in the Matlab <sup>®</sup> Image Analysis routine, optical axis along $z$ . . . . .	103

# List of Tables

3.1	20DC1000ER.1 <i>technical specifications</i> [23]. . . . .	33
3.2	20SJ00ER.3 <i>technical specifications</i> [24]. . . . .	35
3.3	Toshiba BU205M <i>technical specifications</i> [45]. . . . .	39
3.4	Concave mirror and mirror mount components <i>comparative</i> from different suppliers (differences in price reported at <i>time of purchase</i> ). . . . .	41
3.5	Total price quotation <i>comparative</i> for concave mirror and mirror mount components from different suppliers (differences in price reported at <i>time of purchase</i> ). . . . .	41
5.1	<i>Surrounding medium</i> properties (referred to air in SLS conditions). . . . .	77
5.2	<i>Schlieren setup</i> properties. . . . .	78
5.3	SQ1 model by Sico <sup>©</sup> Technology GmbH, technical specifics [39]. . . . .	84
5.4	Comparative evaluation on <i>average temperature overall mean value</i> for different O/F, $\Delta T$ and percentage results with respect to $T_{amb} = 288.15\text{ K}$ . . . . .	93
5.5	Comparative evaluation on <i>average temperature distribution along x-axis</i> for different O/F at specific x-coordinates. . . . .	93

# Nomenclature

## Latin Symbols

$a$	[m]	Vertical Extension of Image at specific point
$b$	[m]	Horizontal Extension of Image at specific point
$B$	[cd · m <sup>-2</sup> ]	Luminance of a Light Beam
$c$	[m/s]	Speed of Light in medium
$c_0$	[m/s]	Speed of Light in vacuum
$C$	[adim]	Contrast <i>or</i> Species Concentration
$D$	[mm]	Schlieren Object Distance from 2ND Mirror
$D_{1,2}$	[mm]	1ST and 2ND Concave Mirror Diameter
$f$	[mm]	Concave Mirror (or Lens) Focal Length
$f/no.$	[adim]	F-Number (or Focal Ratio) of an Optical Element
$H_v$	[lx · s]	Exposure Level
$I$	[lx, cd · sr · m <sup>-2</sup> ]	Illuminance of a Light Beam
$k$	[cm <sup>3</sup> /g]	Gladstone-Dale coefficient
$L$	[m]	Depth of Flow-field along Optical Path
$m$	[adim]	Magnification Factor
$M$	[adim]	Molar Mass of Gas Mixture
$n$	[adim]	Refractive Index
$O/F$	[adim]	Mixture Ratio
$p$	[Pa]	Static Pressure
$R$	[J/Kg · K]	Specific Gas Constant
$\bar{R}$	[J/Kmol · K]	Gas Constant
$s$	[m]	Diff. between <i>Schliere</i> Distance from mirror and $f_2$
$S$	[adim]	Sensitivity of Schlieren System
$t$	[s]	Exposure Time (or Shutter Speed)

## Greek Symbols

$\alpha''$	[rad]	Angular Ray Deflection emerging from Test Area
$\beta$	[rad]	Transmission Deflection Angle inside of an Optical Window
$\gamma$	[adim]	Heat Capacity Ratio
$\delta$	[rad]	Final Deflection Angle emerging from an Optical Window
$\varepsilon$	[rad]	Angular Ray Deflection
$\theta$	[deg]	Nominal concave mirror Tilt Angle
$\theta_{L,R}$	[deg]	Effective 1ST and 2ND concave mirror Tilt Angle
$\lambda$	[m]	Light Wavelength
$\rho$	[kg/m <sup>3</sup> ]	Gas Density

## Abbreviations

1ST	First
2ND	Second
BC	Boundary Condition
BDF	Backward Differentiation Formula
BOS	Background Oriented Schlieren
DAE	Differential-Algebraic Equation
DOF	Depth of Field
EFL	Effective Focal Length
FDM	Finite Difference Method
FL	Focal Length
FOV	Field of View
GCH <sub>4</sub>	Gaseous Methane
GOX	Gaseous Oxygen
IDE	Integrated Development Environment
LED	Light Emitting Diode
LES	Light Emitting Surface
MS	Margin of Safety
NDF	Numerical Differentiation Formula
ODE	Ordinary Differential Equation
PC	Chamber Pressure Transducers
PL	Path of Light
SLS	Standard-Sea-Level Conditions
TC	Chamber Thermocouples
VSVO	Variable-Step, Variable-Order



# Chapter 1

## Introduction

$SFB^1-TRR40^2$  is a joint research centre of the Technical University of Munich, the Technical University of Aachen, the Technical University of Braunschweig, the University of Stuttgart, the German Aerospace Center DLR and Ariane Group. It is funded by  $DFG^3$  and aims to future generations of space-transportation and launcher systems.

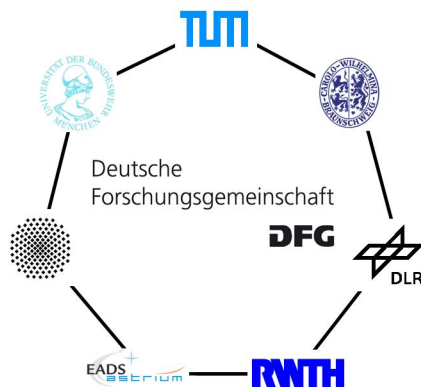


Figure 1.1: *Technological Foundations for the Design of Thermally and Mechanically Highly Loaded Components of Future Space Transportation Systems* joint research center.

TB<sup>4</sup>-K deals with the *thrust chamber*, which is central to the TRR40 structure and represents the application backbone jointly with the industrial TRR40 partner Airbus Defense and Space (formerly Astrium). It focuses on cheaper, more reliable, and more efficient thrust chambers, which primarily will rely on *chemical propulsions systems* (best compromise between development and production cost for the foreseeable future), converging on the impact of injector design and heat loads for gas/gas and gas/liquid propellant combinations. It is also involved in research programs about other specific innovative technologies:

- new nozzle concepts
- alternative fuels
- aft-body flow control
- innovative cooling methods

---

<sup>1</sup>Sonderforschungsbereich, or *Collaborative Research Centres*.

<sup>2</sup>TRANSREGIO 40.

<sup>3</sup>Deutsche Forschungsgemeinschaft, or *German Research Foundation*.

<sup>4</sup>Teilbereiche, German word for *division*.

For what concerns *alternative fuels* solutions, space industries and agencies around the world show rising interest in the propellant combination Oxygen/Methane. In this perspective, the Technische Universität München (TUM) role is pivotal. As leading member, TUM actively introduces students as well as the general public to the topic of *green propellants* [2]. The Institute of Flight Propulsion (LFA) supervised the students of the Scientific Workgroup for Rocketry and Spaceflight (WARR) in the design of a Mobile Rocket Combustion Chamber Test Bench (MoRaP<sup>5</sup>), in Fig.1.2, which operates with gaseous oxygen (GOX) and gaseous methane (GCH<sub>4</sub>) [36] and is provided with an optical access.

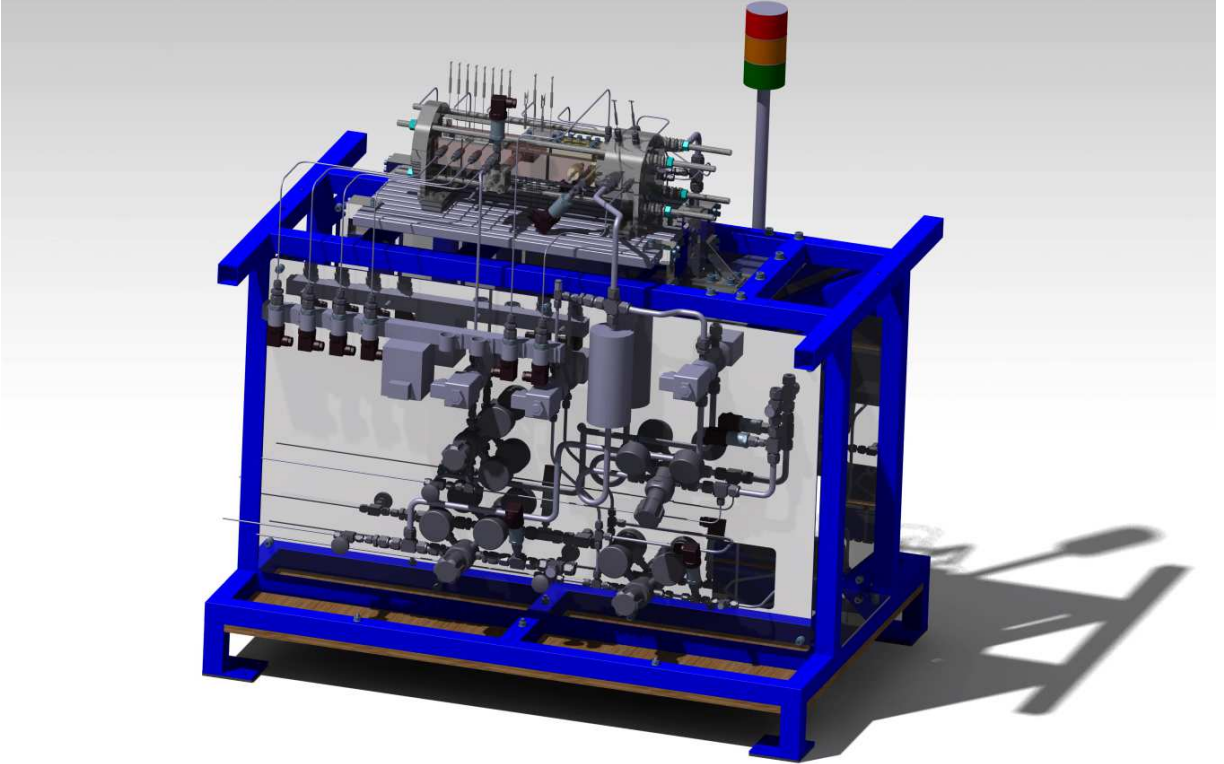


Figure 1.2: *Mobile Rocket Combustion Chamber Test Bench* (MoRaP) CAD model, latest version by S.A. Artene, special thanks to M.Sc. F. Winter.

The GOX/GCH<sub>4</sub> alternative is a relatively new propellant combination, which requires further in-depth analyses before any widespread commercial application. In this perspective, TUM is on the front line, considering its latter optical diagnostic campaign on MoRaP[54]. More recently, LFA has shown interest in including also an optical system for diagnostic with *schlieren* technique. It is the purpose of this master thesis to describe the design process that led to the realization of this machinery.

<sup>5</sup>*Mobiler Raketen Prüfstand*, German expression for *Mobile Rocket Test Bench*.

## Chapter 2

# Theoretical Background

## 2.1 Basic Concepts

Light propagates uniformly through homogeneous media, but the atmosphere shows many disturbances due to turbulence, thermal convection, weather phenomena and many others that result as inhomogeneities in light propagation. These disturbances change the atmospheric density on a relatively-small scale. We can experience these phenomena in everyday routine when a particularly hot day occurs and the air seems to tremble, projecting on the asphalt its characteristic shadow. These inhomogeneities can be studied in optics as *schliere* (german word for optical defects in glass) objects or *streak* objects, which represent a thin region of locally different *refractive index* in a transparent medium.

The first to experience inhomogeneous media with optical observation was R. Hooke (1635-1703) [34, p.2]. A rigorous method of optical investigation was introduced by J. B. L. Foucault (1819-1868) in the middle of 19th century, but the modern application in studying inhomogeneities in the flow of gases (e.g. in wind tunnels) is due to A. Toepler (1836-1912). It was this application that gave the method its name [30].



Figure 2.1: Picture made by the Schlieren method, shows a bullet travelling through the air above two candle flames [55].

Light incident on the *schliere* emerges in a different direction from the direction it would take in the absence of any such inhomogeneity. The change in direction is a measure of the inhomogeneity (or of the irregularity in the surface of an object if the light is reflected) [30]. Human eyes (as ordinary cameras) are unable to discern the phase differences in a light beam, but schlieren methods can translate them into amplitude and contrast differences, to which we result to be very sensitive [34, p.25].

Light speed ( $3 \times 10^8$  m/s in vacuum) decreases upon interacting with matter. In order to measure these change in a transparent medium, we define the *refractive index*  $n = c_0/c$ , where  $c$  and  $c_0$  are the light speed in the medium and vacuum, respectively.

Refractive-index based techniques depend on the unique *refractive index-density* relationship for transparent media [28, p.26][3]. Called the *Lorentz-Lorenz formula*, it is expressed as:

$$\frac{(n^2 - 1)}{\rho(n^2 + 2)} = \text{constant} \quad (2.1)$$

where  $n$  is refractive index and  $\rho$  the density. For air and other gases ( $n \approx 1$ ), the Eq.2.1 reduces to a simple linear relationship, known as *Gladstone-Dale equation*:

$$n - 1 = k\rho \quad (2.2)$$

The Gladstone-Dale coefficient,  $k$ , is about  $0.23 \text{ cm}^3/\text{g}$  for air at standard conditions, while for other gases it may vary roughly from 0.1 to 1.5. On the other hand, the refractive index  $n$  of common gases varies only in the third or fourth decimal place. Air, for example, at  $0^\circ\text{C}$  and  $1 \text{ bar}$  pressure has  $n = 1.000292$  when trans-illuminated by light from the Sodium-D spectral line. As we can see from Eq.2.2,  $n$  is only weakly dependent upon  $\rho$ . A change of two orders of magnitude in air density causes only a 3% change of  $n$ , requiring very sensitive optics to detect small density variations [34, p.26].

From Eq.2.2, we assume *refractivity* ( $n - 1$ ) as dependent only upon gas composition, temperature and density, and the wavelength of illumination ( $k$  increases slightly with increasing light wavelength  $\lambda$ ).

For all the cases of interest, we want to correlate the bending or refraction of light rays with the (measurable) changes in the refractive index due to changes in local density. In order to do so, we assume the z-axis of a right-handed Cartesian  $x, y, z$  coordinate system as the "normal" direction: the optical propagation direction of undisturbed rays approaching a zone of optical inhomogeneity. Now,  $x, y$  pairs describe planes perpendicular to the normal z-direction.

It can be demonstrated (Vasiliev [46] develops it all the way from Maxwell's Equations) that optical inhomogeneities refract or bend light rays in proportion to their gradients of refractive index in an x,y-plane. The present version is thus kept appropriately brief, following Burton [5] in the simple view of geometric optics (see Fig.2.2).

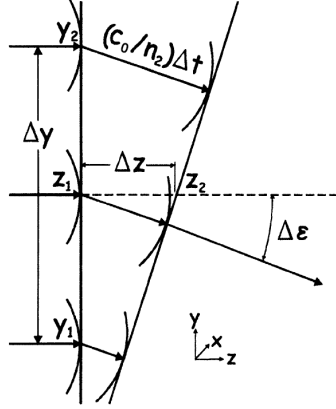


Figure 2.2: Diagram of elemental light refraction by a refractive-index gradient  $dn/dy$  [34, p.339].

By definition of *refractive index*  $n = c_0/c$ , the local value of the light speed  $c$  is  $c_0/n$ .

From the scheme in Fig.2.2, we have:

$$\Delta \varepsilon = \frac{c_0/n_2 - c_0/n_1}{\Delta y} \Delta t$$

The differential time  $\Delta t$  can further be expressed as:

$$\Delta t = \Delta z \frac{n}{c_0}$$

Combining these expressions,

$$\Delta \varepsilon = \frac{n}{c_0} \frac{c_0/n_2 - c_0/n_1}{\Delta y} \Delta z$$

and simplifying terms,

$$\Delta \varepsilon = \frac{n}{n_1 n_2} \frac{n_1 - n_2}{\Delta y} \Delta z$$

The term  $n/n_1 n_2$  in this equation can be simplified to  $1/n$  in the limit, as  $\Delta y$  tends to zero. Letting all the finite differences approach zero, then, we obtain:

$$\frac{d\varepsilon}{dz} = \frac{1}{n} \frac{dn}{dy} \quad (2.3)$$

But since  $\varepsilon$  (also known as  $\alpha$  in literature) is a very small angle, it is approximately equivalent to  $dy/dz$ , the slope of the refracted ray, according to the geometrical construction in Fig.2.2. In this hypothesis, writing the total derivatives as partials to account for the general case in which other refractive-index gradients are present, one obtains:

$$\frac{\partial^2 y}{\partial^2 z} = \frac{1}{n} \frac{\partial n}{\partial y} \quad , \quad \frac{\partial^2 x}{\partial^2 z} = \frac{1}{n} \frac{\partial n}{\partial x} \quad (2.4)$$

which relates the curvature of the refracted ray to the magnitude of the responsible refractive-index gradient [34, p.340]. The second expression is given for the other component,  $\partial n/\partial x$ , in a generic 2-D gradient field.

Integrating once, assuming that the factor  $1/n$  within the integrand does not change greatly through the test section [28, p.29], then the components of the angular ray deflection in the x- and y- directions are:

$$\varepsilon_x = \frac{1}{n} \int \frac{\partial n}{\partial x} dz, \quad \varepsilon_y = \frac{1}{n} \int \frac{\partial n}{\partial y} dz \quad (2.5)$$

A schlieren system can be seen as a device to measure the angle  $\varepsilon$ . In most schlieren applications, this angle is quite small, of the order of  $10^{-6} \div 10^{-3} rad$ . It needs to be understood that the angle  $\varepsilon$  is a function of the coordinates x and y on the exit plane of the test cell [28, p.28].

If the index of refraction within the test section  $n$  is different from that of the surrounding medium  $n_0$ , angle  $\alpha''$  of the light beam emerging from the test area is given by *Snell's law* [28, p.28]:

$$n_1 \sin \alpha_1 = n_2 \sin \alpha_2 \quad (2.6)$$

Assuming  $\alpha_1$  and  $\alpha_2$  to be small angles ( $\sim 10^{-6} \div 10^{-3} rad$  in most applications), we could correct the expression for the angles of interest by using the following:

$$\alpha'' = \frac{n}{n_0} \varepsilon$$

For two-dimensional schlieren (independent of the z coordinate) of extent  $L$  along the optical axis, the final angle emerging from the test region  $\alpha''$  becomes:

$$\alpha''_x = \frac{L}{n_0} \frac{\partial n}{\partial x}, \quad \alpha''_y = \frac{L}{n_0} \frac{\partial n}{\partial y} \quad (2.7)$$

where  $n_0$  is the refractive index of the surrounding medium. The gradients  $\partial n / \partial x$  and  $\partial n / \partial y$ , not the overall level of  $n$ , are cause of the refraction. A region without such gradients is homogeneous and relatively uninteresting. Moreover, Eq.2.3 and Eq.2.4 show that light rays are always bent toward the region of higher  $n$ . From Eq.2.2 for gases, this also means toward the region of higher density  $\rho$ .

These expressions provide the mathematical basis for schlieren and shadowgraph techniques in the following chapters. Of course, the geometric theory of refraction is only an approximation to the more-complete physical optics approach, but is sufficient for present purposes.

## 2.2 Schlieren Technique

Both schlieren and shadowgraphy are methods of analysis that integrate optical systems in order to project line-of-sight information onto a viewing screen or camera focal plane. As such, they are most appropriate for 2-D phenomena but still qualitatively useful for any phenomenon [34, p.29]. Despite of their purpose, their differences are quite strong. The schlieren method (see Fig.2.3a) returns an image, formed by a lens and thus bear-

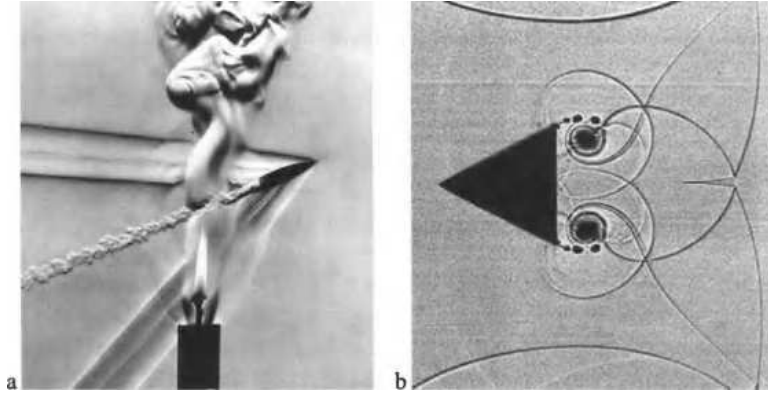


Figure 2.3: Two famous images by Hubert Schardin [32]. **a** Schlieren photo of a bullet and a candle flame. **b** Shadowgram of shockwave diffraction around a triangular block.

ing a conjugate optical relationship to the schlieren object, indeed the illuminance level in a schlieren image responds to the first spatial derivative of the refractive index (e.g.  $\partial n / \partial x$ ) in the *schliere*. On the other hand, the shadowgram (see Fig.2.3b) is not a focused optical image, considering that shadowgraphy returns a mere shadow, which is related to the second spatial derivative or Laplacian (e.g.  $\partial^2 n / \partial^2 x$ ). Equivalently, the schlieren image displays the deflection angle  $\varepsilon$ , while shadowgraphy displays the ray displacement resulting from the deflection [34, p.29]. It is clear the extreme ease of a shadowgraphy apparatus (so little is needed that we can experience natural shadowgrams without use of any technology). In Fig.2.4 it is illustrated a *direct shadowgraph* example.

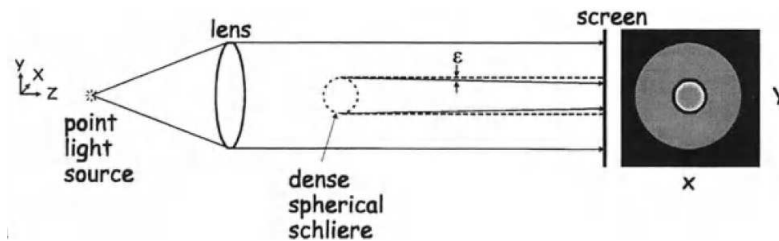


Figure 2.4: Diagram of parallel-light *direct shadowgraph* observation of a dense spherical schliere [34, p.31].

Dissimilarly, schlieren methods require a high precision equipment, with particular focus on the lenses (or mirrors) and the knife-edge filter (further details will follow in the next sections). This last one is pivotal in order to cut-off the refracted light and exhibit the typical schlieren images (see Fig.2.5). Schlieren effects also appear naturally in more-limited

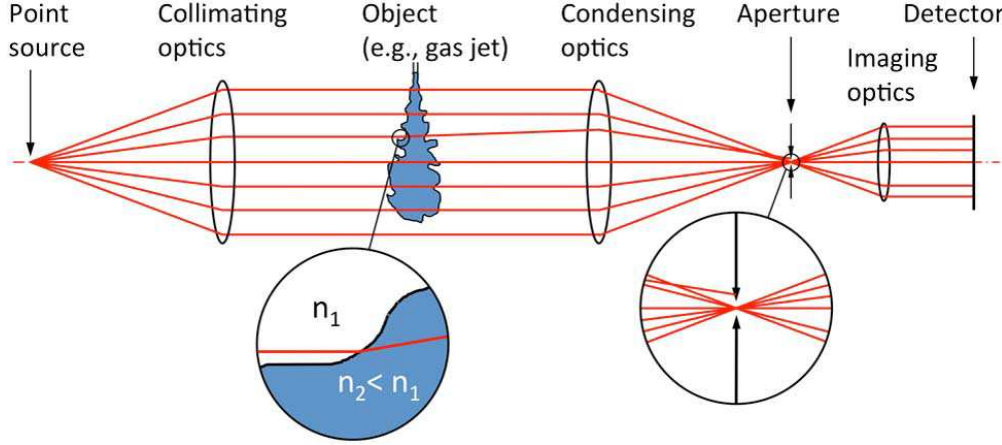


Figure 2.5: General arrangement for schlieren imaging. Enlarged regions within circles illustrate deflection by the rays at the boundary between two refractive indices and the resultant blocking of the deflected rays by the aperture. Note that for clarity this schematic drawing shows only a single beam being refracted, while in reality all beams passing through the jet would experience refraction [17].

circumstances, but they stand out best in the laboratory using lamps, mirrors, and lenses. The resulting image on the detector (see Fig.2.5) shows many darker regions, due to the cut-off over downward refracted beams, and other where the light beams are focused, due to the upward instead. The overall result is a partial picture of the schlieren object as shadows on a bright background, a grey-scale image that virtually contains all the information about the refractive-index variations that describe the schlieren object of interest.

It is important to notice how a knife-edge filter affects only those ray refractions components perpendicular to it. In Fig.2.5 we would need an horizontal oriented filter in order to collect data about  $\partial n / \partial y$  gradients. It follows that any horizontal variation of refractive index, due to  $\partial n / \partial x$  gradients, would remain invisible despite the presence of the filter [34, p.33]. In the next sections, these properties of cut-off effect and their consequences will be analysed in depth .

For now, it is in our interest to find a proper correlation between the 0-255 grey-scale values (in our case the detector is a digital camera) resulting from the schlieren image and the corresponding effects of refraction along the test region.

## 2.2.1 Illuminance

We now consider the more realistic case of an *extended light source*, as shown in Fig.2.6. In this case, we can no more assume that collimation produces exactly-parallel rays. An incoherent beam of white light originates from the extended source (shown by a downward-pointing arrow). For our purposes, it will be a circular slit in the  $x,y$ -plane, but in general its specific shape is secondary.

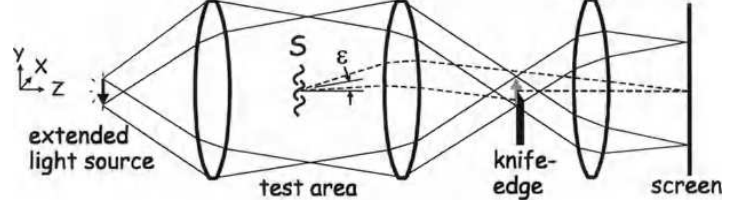


Figure 2.6: Diagram of a simple schlieren system with an extended light source [34, p.34].

We will name  $a_s$  as the *extended light source* diameter, kept at the focus of first field element  $L_1$  (see Fig.2.7). If we place the knife-edge filter at the focus of second field element  $L_2$  [28, p.29], then the relation between the light beam diameter at the knife-edge filter, named  $a_0$ , and  $a_s$  is:

$$\frac{a_0}{a_s} = \frac{f_2}{f_1} \quad (2.8)$$

that in our case of interest (choosing  $f_2 = f_1$ ) leads to  $a_0 = a_s$ .

To step forward in this analysis, it is necessary to correlate the light beam area variation (cut-off amount) to the *illuminance* level perceived at the knife-edge filter.

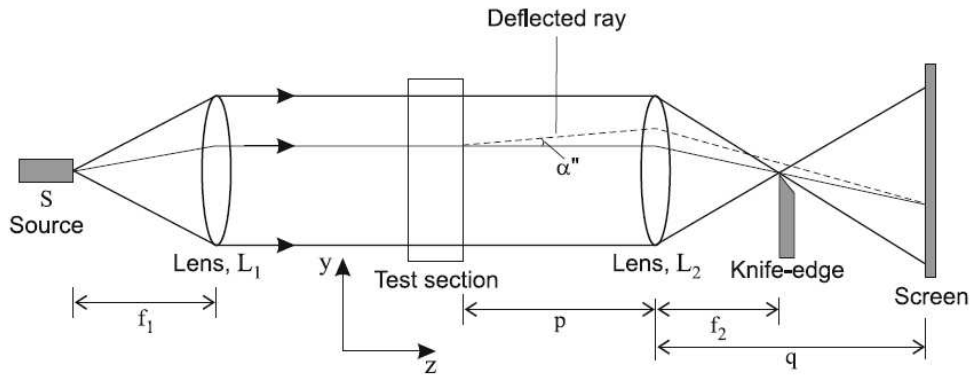


Figure 2.7: Schematic drawing of the path of the light beam in a schlieren system made of lenses [28, p.30].

The *illuminance* ( $I$ ) [ $lx$  or  $cd \cdot sr \cdot m^{-2}$ ] is the total luminous flux incident on a surface, per unit area. This measure of how much the incident light illuminates the surface is often

related to the *luminance* ( $B$ ) [ $\text{cd} \cdot \text{m}^{-2}$ ], that is *luminous intensity* [ $\text{cd}$ ] per unit area corresponding to a light source. For a rectangular source slit [34, p.48] (as said, the specific shape is secondary as long as the conclusions are the same), *illuminance* at the first field element (lens or mirror), would be:

$$I_{1ST} = \frac{B \cdot b \cdot a_s}{f_1^2}$$

where  $b$  (for simplicity) and  $a_s$  are the breadth and height of the source slit, respectively. This value, neglecting any losses (that means without any disturbance in the test region), falls on the second field element (lens or mirror) as:

$$I_{2ND} = \frac{B \cdot b \cdot a_s}{m^2 \cdot f_1^2}$$

where  $m = f_2/s$  is the *magnification factor*, which accounts for image size relative to that of the test area [34, p.73] (effects of *magnification* will be shown in Sec.3.2.1 at p.37).

The  $I_{2ND}$  level is the same that falls over the knife-edge filter position, before its insertion,  $I_0$ . To obtain its expression in  $a_0$  terms, we should take into account the Eq.2.8:

$$I_0 = \frac{B \cdot b \cdot a_0}{m^2 \cdot f_1 f_2}$$

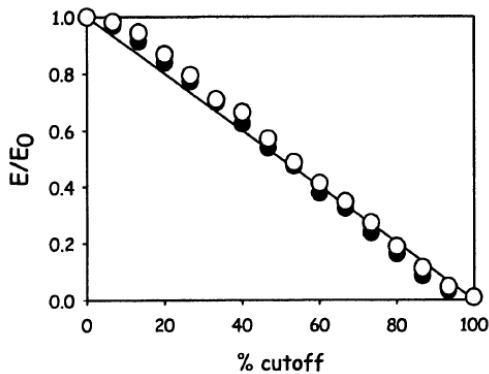


Figure 2.9: Illuminance ratio  $E/E_0$  vs. %cutoff and experimental data for various  $E_0$  [34, p.50].

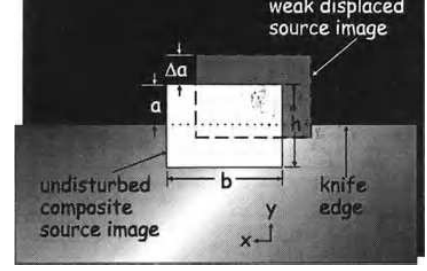


Figure 2.8: Knife-edge plane for a rectangular source image at 50% cut-off, with height  $a$  remaining unobscured. Due to refraction in the test area, a weak elemental source image is shifted. Its unobscured height,  $a + \Delta a$ , passes extra light to a corresponding point in the schlieren image [34, p.36].

where, for simplicity, we do not take into account any changes to  $b$  because they would not affect the results in a vertical refractive-index gradients evaluation.

It is experimentally verified (see Fig.2.9) that there is a linear dependence of illuminance on the cut-off amount, for values far from 0% nor 100% (due to uneven source-slit illumination and to diffraction effects) [34, p.50].

It follows that the illuminance level  $I_k$  with the knife-edge inserted in the focal plane of the second lens but without any disturbance in the test region will be given by:

$$I_k = \frac{a_k}{a_0} I_0 \quad (2.9)$$

where  $a_k$  (or  $a$  in Fig.2.8) is the portion of image not obscured, which leads to:

$$I_k = \frac{B \cdot b \cdot a_k}{m^2 \cdot f_1 f_2} \quad (2.10)$$

Now consider the case of a schlieren object in the test area that refracts a certain light ray through an angle  $\alpha''$ , having y-component  $\alpha''_y$ . In order to obtain the expression for the *incremental gain of illuminance*  $\Delta I$  due to refraction angle y-component  $\alpha''_y$ , it is necessary to bound the displacement of the frame in the vertical direction  $\Delta a$  (see Fig.2.8) with the angular deflection [28, p.31] through relation:

$$\Delta a = \pm f_2 \cdot \alpha''_y \quad (2.11)$$

The sign is positive when the shift is in the upward direction and negative if the light beam gets deflected below the knife-edge. In the dissertation to come, Eq.2.11 is considered with a positive sign. In that case, one could obtain:

$$\Delta I = \frac{B \cdot b \cdot \alpha''_y}{m^2 \cdot f_1} \quad (2.12)$$

which is the expression for the *incremental gain of illuminance*  $\Delta I$  at the corresponding image point due to refraction angle y-component  $\alpha''_y$ . A similar proceeding could be conducted for  $\alpha''$  x-component.

## 2.2.2 Contrast & Sensitivity

In the previous section, we obtained a proper expression for the *gain of illuminance*  $\Delta I$ , for a rectangular source slit, relatively to *luminance* level  $B$  and the angle of deflection  $\alpha''$ . This expression is useful in case of *absolute photometry* [34, p.265], where schlieren-image evaluation associates pixel gray-scale values with source-image displacement values  $\Delta a$ . For this purpose a schlieren calibration curve must be determined (see Sec.3.4 at p.51) using a micrometer knife-edge adjustment and a suitable photocell, PIN diode, or photomultiplier tube. Absolute photometry yields the best sensitivity of all the quantitative schlieren methods: therefore it is usually adopted when high sensitivity is needed.

According to Speak and Walters [41], such quantitative schlieren studies demand parallel light, lest they become hopelessly complicated. Similarly no 3-D flows need apply unless one is willing to resort to tomographic methods.

To avoid using a schlieren calibration curve, which could be affected from many errors if not patiently determined and could become useless if even minimal changes affect the optical system, it is preferred to work with *contrast* values,  $C = \Delta I/I_k$ , which are independent of any illuminance measurement and can be obtained directly from the 0-255 gray-scale values of the images captured by the camera.

Let  $I_f$  be the final illumination on the screen after the light beam has deflected upwards by an amount  $\Delta a$ , due to the inhomogeneous distribution of refractive index in the test cell. This time we will consider a circular shaped slit source (see Fig.2.10).

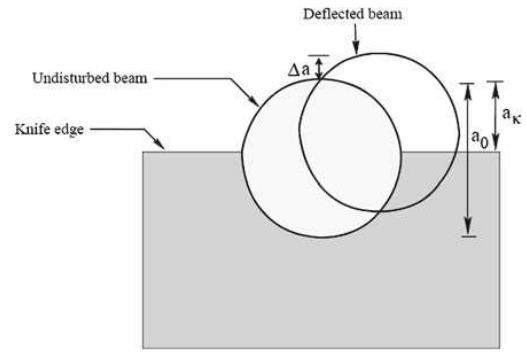


Figure 2.10: View of undisturbed and deflected light beam cross-sections at the knife-edge of a schlieren system [28, p.30].

According to Eq.2.9, it results:

$$I_f = \frac{a_k + \Delta a}{a_k} I_k = \left(1 + \frac{\Delta a}{a_k}\right) I_k$$

which, for the Eq.2.11, leads to definition of *contrast*  $C$  as:

$$C = \frac{I_f - I_k}{I_k} = \frac{\Delta a}{a_k} = \pm \frac{f_2 \cdot \alpha''_y}{a_k} \quad (2.13)$$

where, again, the sign is positive when the shift is in the upward direction and negative if the light beam gets deflected below the knife-edge (analogue proceeding for x-component). It is easy to verify that Eq.2.10 and Eq.2.12 would lead to the same result, confirming that the original slit shape is secondary, except for not obscured vertical extension  $a_k$  (or horizontal extension, for x-component gradients evaluation).

The quantity on the left-hand side can be obtained by using the initial and final 0-255 gray-scale values on the screen. By selecting a certain cut-off amount for the knife-edge filter, one could easily evaluate  $a_k$  as:

$$a_k = \text{cut-off}[\%] \cdot \frac{a_0}{100} \quad (2.14)$$

In Eq.2.14,  $a_0$  is the original dimension of the light beam before the knife-edge filter insertion. In our case ( $f_2 = f_1$ ), it corresponds to the source slit diameter  $a_s$ . If we were dealing with lasers, the exact value of  $a_0$  could not be measured, because its value would be of the order of  $\mu m$  and could be confirmed only by validation against benchmark experiments [28, p.32]. But, in our case, we are dealing with LEDs and we could virtually choose a specific value for  $a_0$  by implementing a pin-hole slit at a focal point along the light path (see Sec.3.2.1 at p.31).

*Schlieren sensitivity* (also called *contrast sensitivity*) is an useful evaluative parameter of any schlieren setup. It is defined as:

$$S = \frac{dC}{d\varepsilon} = \frac{f_2}{a_k} \quad (2.15)$$

which means that, in order to increase sensitivity, one could think to choose a 2ND mirror (or lens) with a longer FL rather than a shorter one, or to increase the cut-off amount (decrease  $a_k$ ). Both the solutions will be taken into account, with particular attention to the cut-off amount, that should be at least 50% ( $a_k = a_0/2$ ) [12]. At a glance, seems like an  $a_k \rightarrow 0$  could lead to an infinite sensitivity, which of course is a misconception caused by not taking into account light diffraction effects for cut-off amount near to 100%.

## 2.3 Resolutive Algorithm

In order to conduct a numerical evaluation of small-density variations on the x,y-plane from the very end of the test region, by relating pixel-by-pixel the x,y-components of the resulting angle  $\alpha''$  (different from each x,y-couple) to *contrast* values resulting from gradients evaluation, it is necessary to combine all the results yet obtained in a recursive perspective.

As long as  $\alpha''$  is related to refractive-index gradients  $\partial n/\partial x$  and  $\partial n/\partial y$  by Eqs.2.7, we will derive Gladstone-Dale equation (Eq.2.2) in order to express the first derivative of the refractive index (with respect to  $x$  direction<sup>1</sup>) in terms of density gradient [28, p.32]:

$$\frac{\partial \rho}{\partial x} = \frac{\rho_0}{(n_0 - 1)} \frac{\partial n}{\partial x} \quad (2.16)$$

where  $(n_0 - 1)/\rho_0$  is the *Gladstone-Dale coefficient* of the surrounding medium (known).

---

<sup>1</sup>In order to derive variations along the main direction of a longitudinal *combustion chamber*.

Since  $n_0 \approx 1$  for gases [28, p.29], we can combine Eq.2.16 with Eqs.2.5, in order to obtain:

$$\alpha_x'' = \frac{(n_0 - 1)}{\rho_0} \int_0^L \frac{\partial \rho}{\partial x} dz \quad (2.17)$$

Eq.2.17 shows that the schlieren technique records the path integrated gradient of refractive index over the length of the test section  $L$ .

If the field is 2D (in the x,y-plane), the quantity  $\partial \rho / \partial x$  is independent of the  $z$  coordinate [28, p.31], which is a strong hypothesis to adopt. On the other hand, it constitutes a necessary assumption in order to proceed with numerical evaluations<sup>2</sup>. This approach adopts the *paraxial* approximation, that assumes the derivatives in  $x$  and  $y$  directions to have independent influences on beam deflection, which is expected to hold under a *small angle approximation* [28, p.32]. Under these simplified hypotheses, the Eq.2.13 leads to the **governing equation for schlieren measurement in gas**, that can be rewritten as:

$$C = \frac{\Delta I}{I_k} = \frac{f_2}{a_k} \frac{(n_0 - 1)}{\rho_0} \frac{\partial \rho}{\partial x} L \quad (2.18)$$

By integrating this first-order linear differential equation (in variable  $\rho$ ) along  $x$ -axis, starting from a known boundary value<sup>3</sup>, it is possible to obtain the density values  $\rho(x,y)$  for each raw along  $x$ -axis. Actually, for a picture this constitutes a recursive process, because the integration has to be solved for each  $y$  coordinate (for each raw) in case of evaluation of gradients along  $x$ -axis (vice versa for an evaluation of gradients along  $y$ -axis).

At this point, one has just deduced the density values of a schlieren object on an  $x,y$ -plane from a single picture, taken through schlieren technique. In Sec.2.4 it will follow how to implement this differential equation for each raw of  $C$ , the matrix which contains the *contrast* values, of  $M,N$ -dimension (related to a picture with an  $M \times N$ -pixels resolution).

---

<sup>2</sup>Indeed, to know the  $\partial \rho / \partial x$  (such as  $\partial \rho / \partial y$ ) distribution along  $z$ -axis would mean, in a relatively easy case as an axial-symmetric inhomogeneous field (e.g. a combustor flame), to already know the solution of our schlieren analysis and consequently to nullify our efforts. In this perspective, we can assume the field of interest to be 2D (in the  $x,y$ -plane) by applying the mean value theorem for integrals, which leads to a thoughtful choice of  $L$  (depth of the flow-field along the optical axis) and to  $\partial \rho / \partial x$  values which are a mean value of its variations along the optical axis  $z$ , for each  $x,y$ -couple. One can stand with such simplified hypotheses, because the density evaluation over the  $x,y$ -plane depends from both gradients of density and depth of the flow-field, which, if properly combined, can reconstruct the results of a 3D analysis.

<sup>3</sup>E.g.  $\rho_0$  from the surrounding medium for tests in an open environment (e.g. an *open burner*); or values along  $y$ -axis at a specific  $x$ -coordinate from inside the *combustion chamber*.

Accordingly, one could think to obtain the temperature and pressure values by adopting the *isentropic relations*:

$$\frac{T}{T_0} = \left(\frac{\rho}{\rho_0}\right)^{\gamma-1}, \quad \frac{p}{p_0} = \left(\frac{T}{T_0}\right)^{\frac{\gamma}{\gamma-1}} = \left(\frac{\rho}{\rho_0}\right)^{\gamma} \quad (2.19)$$

which would be reasonable if we were studying an isentropic flow (e.g. isentropic expansion). Unfortunately, one is not allowed to accept this hypothesis, due to transfer of heat and mass from the combustion process<sup>4</sup>. Therefore, it is more reasonable to adopt the perfect-gas state equation:

$$\frac{p}{\rho} = RT \quad (2.20)$$

where  $R$  is the specific gas constant<sup>5</sup>.

By substituting Eq.2.20 into Eq.2.18, we would obtain the following:

$$C = \frac{\Delta I}{I_k} = \frac{f_2(n_0 - 1)}{a_k \rho_0} \left( \frac{\partial}{\partial x} \frac{p}{RT} \right) L$$

Assuming that the pressure inside the test cell is practically constant<sup>6</sup> [28, p.33], we finally get:

$$C = \frac{\Delta I}{I_k} = -\frac{f_2(n_0 - 1)}{a_k \rho_0} \frac{p}{RT^2} \frac{\partial T}{\partial x} L \quad (2.21)$$

which is a first-order non-linear differential equation (in variable  $T$ ) along x-axis, that needs to be solved for each y coordinate (each raw), starting from a known boundary value<sup>7</sup>. The Eq.2.21 has to be treated as a *stiff* differential equation (see next section for further details).

Eq.2.18 and Eq.2.21 respectively relate the contrast values measured through schlieren technique with the density and temperature gradients in the test section. By defining the dependent variables  $\rho$  and  $T$  through proper boundary conditions, these equations can be integrated to determine the quantities of interest [28, p.32].

---

<sup>4</sup>In an isentropic flow, at any decrease in density level, would correspond (see Eq.2.19) a fall into temperature level, which is not the case. Indeed, we are studying heat addition due to a combustion process

<sup>5</sup>One could also consider the effects of temperature on  $R = R(T)$ , specific gas constant, or to assign a constant value for the mean temperature that characterizes the phenomenon.

<sup>6</sup>This is a strong hypothesis, which is realistic in most of the cases of interest: for tests in an open environment (e.g. an *open burner*), it is reasonable to assume  $p = p_0$ , as an *isobaric* combustion process; otherwise, in a closed environment (e.g. a *combustion chamber*), it would be an error not to take into account a  $p$  value different from  $p_0$  and its variations along the x-axis, but its variation along the optical axis could still be acceptable as long as one is strictly interested in variations of pressure along a specific axis (such as the main axis of the longitudinal *combustion chamber*).

<sup>7</sup>E.g.  $T_0$  from the surrounding medium for tests in an open environment (e.g. an *open burner*); or specific values along x-axis from the inside of the *combustion chamber*.

## 2.4 Computational Implementation

In order to implement Eq.2.18 and Eq.2.21 in a calculation code, one first has to rearrange them in explicit form (with respect to the variable of interest) and then in matrix form:

$$\frac{\partial \rho}{\partial x} = \left[ \frac{a_k}{f_2} \frac{\rho_0}{(n_0 - 1)} \right] \frac{C}{L} \quad , \quad \frac{1}{T^2} \frac{\partial T}{\partial x} = - \left[ \frac{a_k}{f_2} \frac{\rho_0}{(n_0 - 1)} R \right] \frac{C}{pL} \quad (2.22)$$

The quantities between square brackets are presumably all constants, so that one can simplify the Eqs.2.22 by adopting the following form:

$$\frac{\partial \rho}{\partial x} = K_\rho \frac{C}{L} \quad , \quad \frac{1}{T^2} \frac{\partial T}{\partial x} = -K_T \frac{C}{pL} \quad (2.23)$$

where both  $K_\rho$  and  $K_T$  describe schlieren setup properties (such as *2ND mirror FL* and *cut-off amount*) and gas properties (such as *Gladstone-Dale coefficient* and *specific gas constant*). We will not include the depth of field along the optical axis  $L$  in this constants because of its pivotal role during integration process, that will be explained in detail further on.

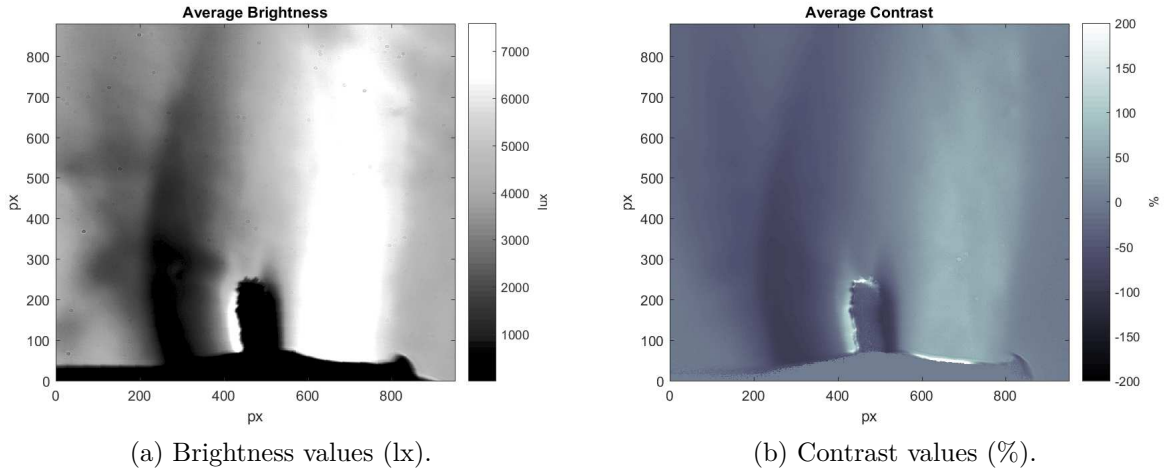


Figure 2.11: Pictures reporting *mean values* relative to a test campaign on a *candle test*, carried out in laboratory by the author and post-processed by a Matlab<sup>®</sup> Image Analysis routine.

To properly solve the differential problem, we first have to correctly identify all the members of Eqs.2.23. Considering Fig.2.11, one can associate a generic schlieren picture (Fig.2.11a) to its specific *contrast* matrix  $C$  (Fig.2.11b), which values are compared to a previous picture in *wind-off* conditions (no flames, flows or any other inhomogeneous

phenomenon running out in the test field), to extract the quantity  $C = \Delta I/I_k$  pixel-by-pixel (e.g. a  $900 \times 900$  px image will result in a *contrast* matrix  $C$  of dimension  $900 \times 900$ ). If one is conducting a numerical evaluation along x-axis, then the integration process must be carried out on every single y-coordinate.

### 2.4.1 Study of Variables and Boundary Conditions

For a generic  $M \times N$  dimension *contrast* matrix  $C$ , we can re-adapt the governing equation in terms of density  $\rho$  from Eqs.2.22, for each y-coordinate, as:

$$\dot{y}(x) = K_\rho \frac{C(x)}{L(x)} \quad , \quad y(0) = \rho(0) \quad (2.24)$$

where the non-homogeneous terms on the right are known only for specific values of  $x = (m-1) \cdot \Delta x$  ( $\Delta x$  is the actual distance covered between each pixel<sup>8</sup>), with  $m = 1, \dots, M$  ( $x = 0$  corresponds to the BC).

The BC  $\rho(0)$  could either be  $\rho_0$  of the surrounding medium for an *open environment*, nor a specific  $\rho$  value previously estimated from inside of a *closed environment* (e.g. a *combustion chamber*, collected away from the flame and close to the walls<sup>9</sup>).

Even  $L$  (depth of the flow-field) could be, strictly speaking, a function of the x-coordinate.

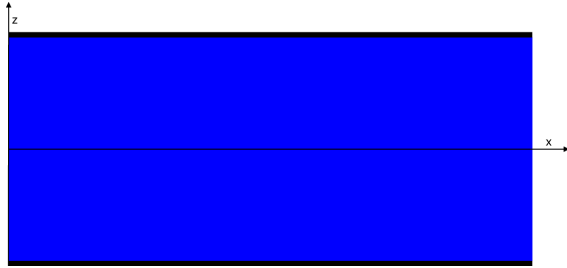


Figure 2.12: View from above of an "AllDomain" flow-field model.

Indeed, it is necessary to define a *flow-field model* that can describe the phenomenon you are actually studying with high fidelity. Some of this models are shown in Fig.2.12 and Fig.2.13 (all the other models that have already been implemented in the Matlab® Image Analysis routine are reported in Appendix A.2).

In most of the cases, an "AllDomain" model (constant depth of flow-field all along the optical axis), is the best solution for a *closed environment* (e.g. a *combustion chamber*) as long as every portion of the volume effected by the phenomenon is well contained.

<sup>8</sup> $\Delta x$  is the distance covered from each pixel along the x-axis, which is calculated by extracting the number of pixels in correspondence to the maximum circular segment along x-axis from the *wind-off* image and by dividing the 2ND parabolic mirror diameter, from the schlieren setup, for this number.

<sup>9</sup>This  $\rho$  values could be experimentally evaluated by matching measurements from thermocouples (TC) and pressure transducers (PC).

Otherwise, for an *open environment* (e.g. *candle test* and *open burner*) it is reasonable to

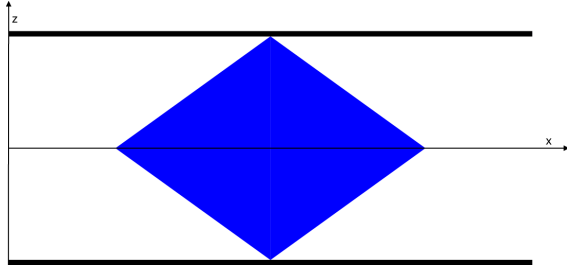


Figure 2.13: View from above of an example of a "Diamond" flow-field model.

do not consider any portion of the volume in which no sensitive variation are happening. This is pursued by adopting different values<sup>10</sup> of  $L$  along the x-axis, by testing different laws of distribution in the junction areas between uniform and inhomogeneous regions. In this perspective, the solutions for "Linear"/"Diamond" and "Sinusoidal"/"Cylindric" models (see Appendix A.2) showed more realistic behaviours.

More complex models of  $L = L(x, y)$ , which could take into account also variations along the y-axis<sup>11</sup> (or along the x-axis in case that one is conducting  $\partial n / \partial y$  evaluations), have not been handled, but nothing keeps the reader from trying to implement new models in order to satisfy his practical needs.

At this point, we have correctly defined all the members of Eq.2.24. On the other hand, by re-adapting the governing equation in terms of temperature  $T$  from Eqs.2.22, for each y-coordinate, one obtains:

$$\frac{1}{y^2(x)} \dot{y}(x) = -K_T \frac{C(x)}{p(x)L(x)} \quad , \quad y(0) = T(0) \quad (2.25)$$

where  $T(0)$  (BC) and  $p(x)$  (pressure distribution along x-axis) have to be properly defined, in order to solve the Eq.2.25. The BC  $T(0)$  could either be  $T_0$  from the surrounding medium for an *open environment*, nor a specific  $T$  value previously estimated from inside of a *closed environment* (e.g. a *combustion chamber*, collected by TCs, being sure to apply the sensors away from the flame and close to the walls).

The  $p(x)$  distribution could be simplified as a constant value for isobaric processes ( $p_0$  for *open environment* or  $p$  for *closed environment*) or an interpolation along x-axis of experimental measurements for specific x-coordinates<sup>12</sup> (PCs measurements along the walls).

<sup>10</sup>It is interesting to underline that, in order to avoid any numerical error in Eq.2.24,  $L(x)$  is never zero, but its minimum value (in *open environment* domains) is as close to zero as possible ( $\sim 10^{-4}$ ). This value is chosen with the purpose to be the smallest before any numerical errors occur and depends on the specific test one is running.

<sup>11</sup>In all the cases implemented in the Matlab® Image Analysis routine, the flow-field models define the base of a parallelepiped (note that  $L = L(x)$  means a depth of flow-field constant along y-axis).

<sup>12</sup>Not strictly correct, since it assumes variations on  $p$ , which contrasts the isobaric phenomenon hypothesis [28, p.33]. Further studies about modelling of non-isobaric phenomena are advisable.

## 2.4.2 Integration Method

The Eq.2.24 is a first-order linear ordinary differential equation (ODE) in the form  $dy/dx = F(x)$  and its solution is generally obtained by direct integration [34, p.265]:

$$\rho(x) = \frac{1}{K_\rho} \int_{x_1}^{x_2} C(\lambda) L(\lambda) d\lambda + \rho_{ref} \quad (2.26)$$

but this is not the case, because we do not actually possess an analytic distribution of *contrast* values, but we only know them in specific points of the x,y-plane. In this perspective, it could be reasonable to adopt a *finite difference method* (FDM) by approximating the first derivative to its *difference quotient*:

$$\frac{dy}{dx} \approx \frac{y(x + \Delta x) - y(x)}{\Delta x} \quad (2.27)$$

where  $\Delta x$  is the distance covered between two pixels (see Pag. page 17). For a generic  $M \times N$  *contrast* matrix of elements  $C(m,n) \equiv C_{m,n}$ , with  $m = 1, \dots, M$  and  $n = 1, \dots, N$ , for each  $n$  column, one should proceed from a known value (BCs at  $m = 1$ ) and then by solving the equation for every  $x = (m - 1) \cdot \Delta x$ .

This first order approximation works very well for first-order linear ODEs, such as Eq.2.24, returning a sharp and uniform distribution of  $\rho_{m,n}$ . On the other hand, from a purely programming-perspective, this approach risks to result over-intricate and slow in the execution. This issue has been fixed by implementing a Matlab<sup>®</sup> routine for *non-stiff* ODEs.

On contrary, a FDM approach seems to work badly on Eq.2.25, which is an inhomogeneous first-order nonlinear ODE. Because of its non-linear terms, which often generate singularities for  $C_{m,n}$  values close to zero, the FDM solutions show a non-convergent behaviour. In order to solve Eq.2.25, it is necessary to involve a Matlab<sup>®</sup> routine, specific for *stiff* problems, such as *ode15s*<sup>13</sup>. This choice is confirmed to be the most valuable by matching its results (see Fig.2.14b) with the actual shape of the flame (see Fig.2.11a) and with known realistic values of temperature.

---

<sup>13</sup>Matlab<sup>®</sup> *ode15s* is a variable-step, variable-order (VSVO) solver based on the numerical differentiation formulas (NDFs) of orders 1 to 5. Optionally, it can use the backward differentiation formulas (BDFs, also known as Gear's method) that are usually less efficient. It is a multistep solver. One should use *ode15s* if *ode45* fails or is very inefficient because the problem may be stiff, or when solving a differential-algebraic equation (DAE)[38].

For a well delimited phenomenon, like on a *candle test*, the best validation comes from verifying that the solution properly returns to its surrounding medium conditions, away from the region of inhomogeneities, which actually happens (with an arguable margin of error, due to the lack of accuracy related to this specific *candle test* conditions<sup>14</sup>).

The Matlab<sup>®</sup> Image Analysis routine has been optimized by implementing a Matlab<sup>®</sup> routine for *non-stiff* ODEs, such as *ode45*<sup>15</sup>. The consequences of such a choice are a much faster evaluative routine and a more uniform programming structure. The results about  $\rho_{m,n}$ , coming from the Matlab<sup>®</sup> *ode45* routine, are equivalent to the ones obtained by an alternative FDM approach, letting the choice to fall upon the first method in a merely programming-oriented perspective.

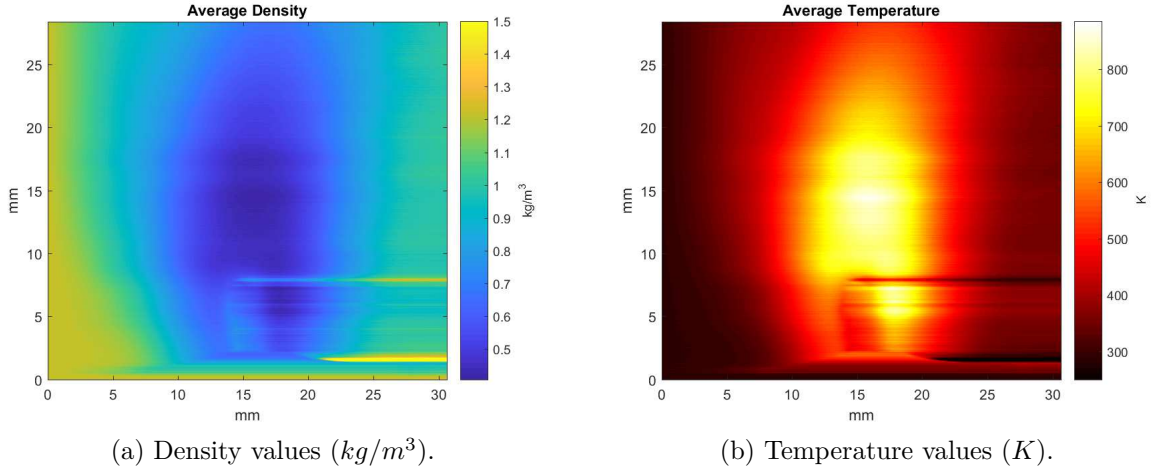


Figure 2.14: Pictures reporting *mean values* relative to a test campaign on a *candle test*, carried out in laboratory by the author. The Eq.2.24 and Eq.2.25 have been solved by adopting Matlab<sup>®</sup> routines for differential equations, more specifically *ode45* and *ode15s*.

### 2.4.3 Window Correction

Windows are often used to get optical access to gases contained in delimited regions (e.g. MoRaP combustion chamber), the refractive index of their material is considerably different from the one of the confined gases or from the surrounding medium [28, p.33]. For this reason, the presence of a window has to be taken handled by applying a correction factor to Eq.2.18 (see p.14).

<sup>14</sup>The numerical errors on the right-side are due to the presence of the wick of the candle.

<sup>15</sup>Matlab<sup>®</sup> *ode45* is based on an explicit Runge-Kutta formula. It is a single-step solver that, in computing  $y(t_m)$ , needs only the solution at the immediately preceding point,  $y(t_{m-1})$  [38].

With reference to scheme reported in Fig.2.15, we assume the deflection due to first optical window to be negligible (for almost parallel incoming rays). The presence of a schlieren object (refractive index  $n_{fluid}$ ) results in a total refraction  $\alpha''$  for the light beam, which strikes the second optical window at this angle. One can derive the resulting transmission angle  $\beta$  inside of the optical window (refractive index  $n_{window}$ ) by applying the *Snell's Law* (see Eq.2.6 at p.6):

$$n_{fluid} \sin \alpha'' = n_{window} \sin \beta$$

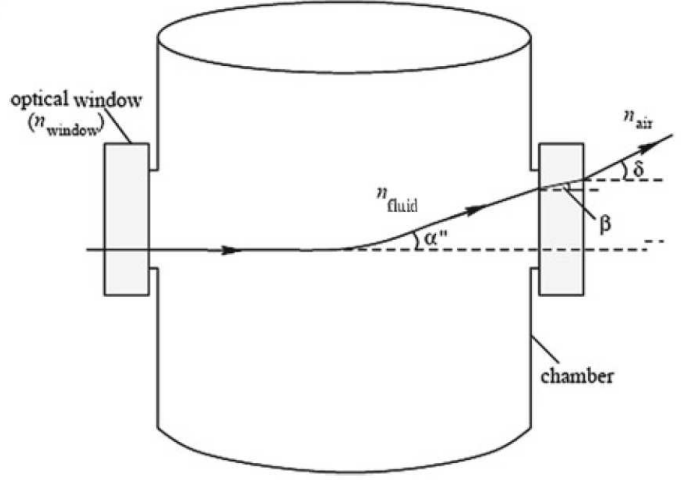


Figure 2.15: Geometrical construction scheme of light beam path altered by presence of a window [28, p.34].

Since  $\alpha''$  and  $\beta$  are quite small in most application ( $\sin \alpha'' \approx \alpha''$ ,  $\sin \beta \approx \beta$ ):

$$\beta \approx \left( \frac{n_{fluid}}{n_{window}} \right) \alpha''$$

Let  $\delta$  be the *final angle of refraction* with which the light beam emerges into the surrounding air. By applying the *Snell's Law*, in a similar way, it results:

$$n_{window} \sin \beta = n_{air} \sin \delta$$

By assuming also  $\delta$  as small angle ( $\sin \delta \approx \delta$ ):

$$\delta \approx \left( \frac{n_{window}}{n_{air}} \right) \beta$$

This assumptions, finally lead to:

$$\delta \approx \left( \frac{n_{window}}{n_{air}} \right) \left( \frac{n_{fluid}}{n_{window}} \right) \alpha'' = \left( \frac{n_{fluid}}{n_{air}} \right) \alpha'' \quad (2.28)$$

Indeed, the final contrast value that one actually measures is due to  $\delta$ . As long as one assumes  $(n_{fluid}/n_{air}) > 1$ , according to Eq.2.28 the presence of a windows tends to amplify the refraction angles originally coming from the test region inside of the chamber, which result in higher gradient values with respect to their real values in the flow-field.

In experiments with optical windows, schlieren image analysis should be carried on by first computing  $\alpha''$  from the recorded angle  $\delta$ . This is a not-trivial task, because the light path described in Fig.2.15 takes into account distances from schlieren object to window inner surface and from window outer surface to 2ND optical element (e.g. concave mirror), window depth and tin-bath direction being as parallel as possible to knife-edge. Slight measuring errors can have deep repercussions on final results, which means that the operator has to pay particular attention to details in order to achieve a satisfying precision level. Moreover, high mirror flatness and interior quality are a must, since even  $\sim 0.1 \text{ arcsec}$  refractions are visible in a well-calibrated schlieren system, which several times makes windows as expensive as optical lens of same diameter. Unfortunately, for combustion work, windows are often a necessity, so that one has to move on specific classes of material, such as *BK-7 glass* or *fused silica*, in order to guarantee satisfying results [34, p.175].

As a temporary solution for preliminary studies, an approximated formula is here offered, valid for *window depth* and *distance from schlieren object to inner window surface* both *negligible* with respect to 2ND optical element FL ( $f_2$ ). If  $\delta$  is the actual refraction angle detected from the optical system then, accordingly with Eq.2.13, one can assume that:

$$C = \frac{I_f - I_k}{I_k} \approx \pm \frac{f_2 \cdot \delta}{a_k} = \pm \left( \frac{n_{fluid}}{n_{air}} \right) \frac{f_2 \cdot \alpha''}{a_k}$$

which leads to a governing equation for schlieren measurement is gas *corrected* for windows:

$$\left( \frac{n_{air}}{n_{fluid}} \right) \frac{\Delta I}{I_k} \approx \frac{f_2}{a_k} \frac{(n_0 - 1)}{\rho_0} \frac{\partial \rho}{\partial x} L \quad (2.29)$$

The computational implementation of Eq.2.29 follows the same procedure presented in Sec.2.4, with *corrected contrast values* scaled by a  $(n_{air}/n_{fluid})$  factor. It is important to remark that this solution is valid only for *window depth* and *distance from schlieren object to inner window surface* negligible with respect to  $f_2$ . In case that one is studying an object very distant from the window (e.g. wind tunnels), nor is adopting a window with a discrete depth (e.g. combustion chambers), the Eq.2.29 can be used for preliminary studies only. That is because the Matlab<sup>®</sup> routine is predisposed for modelling windows along the optical axis, but not yet optimized. This current limitation will require most of future efforts on programming the Matlab<sup>®</sup> routine, in order to improve these particular aspects of the modelling of optical components.

## Chapter 3

# Project Design

### 3.1 Conceptual Design

A design process is not a route of consecutive decisions that leads to an ideal solution. It requires many attempts and steps backward before reaching a final solution that suits all the requirements. In spite of this, the following chapter is a reconstruction in consecutive perspective of the design process in its entirety, in an attempt to present the decision-making approach adopted by the author in a more fluent form. In order to do so, a three parts division[16] of the design process has been adopted, which is very common for the design in civil aeronautic field and, once adapted to the new small case scenario, it resulted surprisingly useful for the decision-making process of this specific project.

In the *conceptual design* phase, many conventional and novel configurations are taken into account, in order to match the project requirements with innovative and commercially viable solutions. The *preliminary design* phase starts from one or two best-candidate configurations, developing them in parallel eventually. Then, in the remaining *detail design* phase, a unique solution is fully optimized.

#### 3.1.1 Conventional and Novel Configurations

Schlieren technique has a long tradition, rooted in the 19th century and mostly developed in the 20th, yet in motion up to the present. This translates in a plethora of possible configuration, each one with its peculiarity and disadvantages. From here on will follow some examples of schlieren arrangements, which can be considered noteworthy for our purposes.

## Lens Systems

Toepler's original device used lenses of telescopes as schlieren heads, then mirror-based systems followed shortly on the strength of Foucault's knife-edge test [34, p.39]. The simplest lens configuration is the *Toepler's single-field-lens schlieren arrangement*, which is commonly considered outdated, due to its ambiguous interpretation of  $\Delta a = f_2 \cdot \varepsilon$  [34, p.40]. Indeed, a typical *dual-field-lens schlieren arrangement* is preferable (see Fig.3.1).

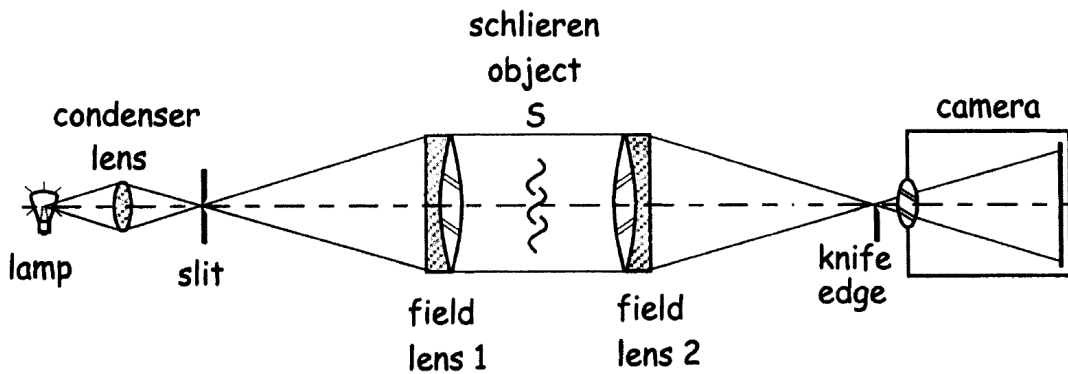


Figure 3.1: Dual-field-lens schlieren arrangement [33][34, p.41].

Lens-type schlieren systems have components arranged in-line, which makes them easier to calibrate rather than a mirror-type system, which components are inherently folded. This is not a big issue, though, unless one does not use too many mirrors [34, p.39]. On the other hand, a multi-element lenses system requires high internal quality and near-perfection surfaces polishing, while mirrors need little internal quality and well-cleaned surfaces. Furthermore, a lens is more affected by chromatic aberration, even an expensive achromatic one, due to partial spectrum cut-off, despite of a simple mirror system.

## Mirror Systems

Typically, commercial prices for schlieren-quality mirrors are much lower than prices for lenses of the same diameter [34, p.40] (the exponential rise of cost with diameter depends upon the manufacturer, generally presenting a steepest rise in case of lenses). For this reason, in order to gain a larger field-of-view for a given cost and to avoid chromatic aberration, it is common to adopt mirror-type systems in place of lenses-type ones [1].

**Z-Type 2-Mirror Schlieren System** By far the most common mirror schlieren system, the *Z-type Herschellian*<sup>1</sup> arrangement can make use of spherical, parabolic or concave mirrors. The letter Z comes from the combination of a diverging illuminator beam, a parallel beam between the mirrors and a converging analyzer beam [34, p.42]. This solution solves the chromatic aberrations, but lets arise *off-axis aberrations*, such as *coma* and *astigmatism* (see Sec.3.2.1 at p.36 and Sec.4.2 at p.65).

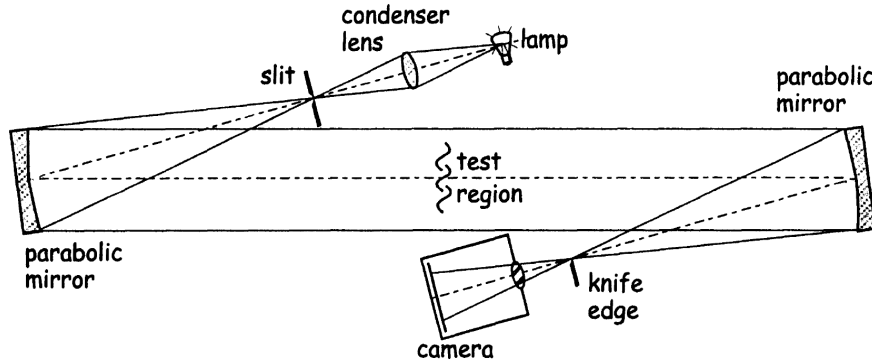


Figure 3.2: Z-type schlieren arrangement [32][33][34, p.42].

**Z-Type 2-Parabolic-2-Flat-Mirror Schlieren System** A much newer version of the classic Z-type system, this modern configuration involves two extra flat-mirrors, in order to downsize the space needed to arrange the schlieren system. This solution offers a lot of ideas about how to re-arrange the optical components in a *modular* perspective.

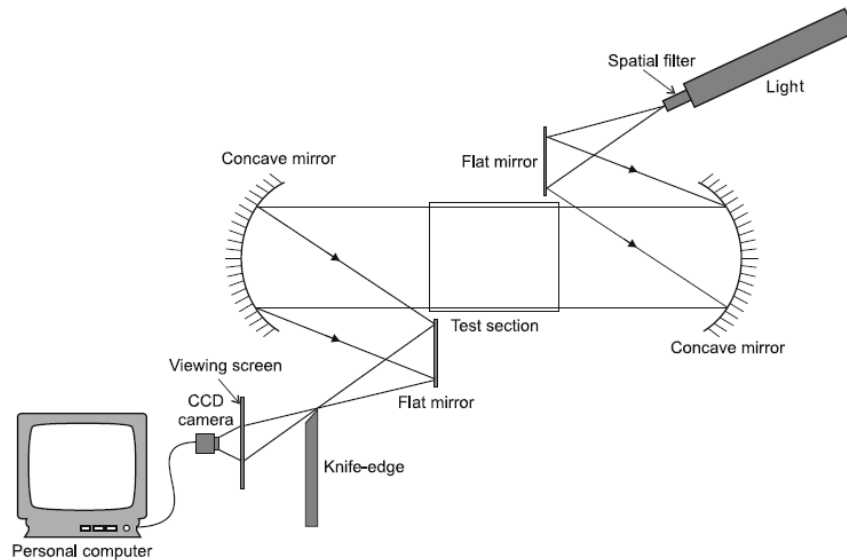


Figure 3.3: Z-type 2-parabolic-2-flat-mirrors schlieren arrangement [28, p.25].

<sup>1</sup>W. Herschel (1738-1822), German astronomer.

**Single-Mirror Systems** These mirror-based systems do not take advantages from a parallel light beam. The *single-mirror coincident system* (in Fig.3.4a) was adopted by Taylor and Waldram [43], deeply analysed by Schardin and credited to Hans Boas [6]. It is also called "*auto-collimating*", due to its similarity to an autocollimator for aligning a telescope mirror. The alternative *single-mirror off-axis system* configuration reported (see Fig.3.27b) does not take advantage from the coincident method just shown. While Schardin [32][33] found this useful, few have used it since. Both systems in Fig.3.4 are subject to off-axis aberrations but, even worse, the off-axis system demands a mirror twice the diameter of the desired FOV, which may constitute a big issue in case of lack of space.

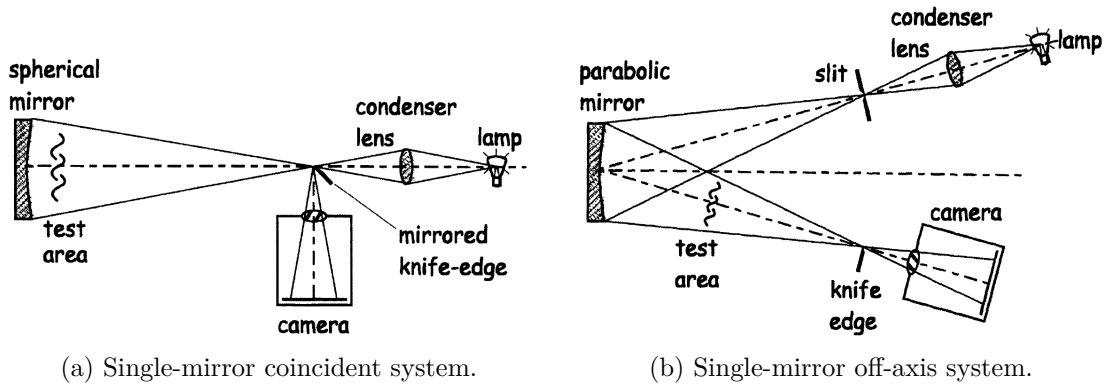


Figure 3.4: Two single-mirror possible arrangements [34, p.47].

## Lens-and-Background Techniques

Schlieren systems mostly based on a single lens, a large source background (e.g. a *grid*), and non-parallel illumination. Conceived by Burton [5], this technique evolved dramatically in the last century, with results nonetheless than spectacular.

**Background Grid Distortion** A background grid can result in an array of light/dark edges or stripes [33]. The first applications combined a need for simplicity and large FOV with the lack of any particular need for high sensitivity [8][25], returning qualitative-results only.

Later on, the technique evolved in more complex solutions (e.g. involving a complementary negative cut-off grid, see Fig.3.5) that deeply improved its sensitivity and resolution.

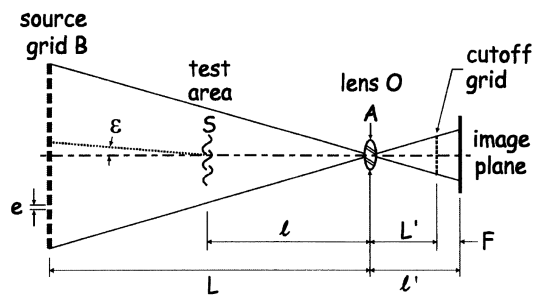


Figure 3.5: Diagram of Schardin's schlieren method no. 4, the lens-and-grid technique [34, p.89].

**Background Oriented Schlieren** These methods are based on a numerical comparison between a schlieren distorted image and an undistorted image of a deliberate background. This technique does not need a peculiar cut-off component, which makes the system much easier to calibrate and its components to align along the optical axis.

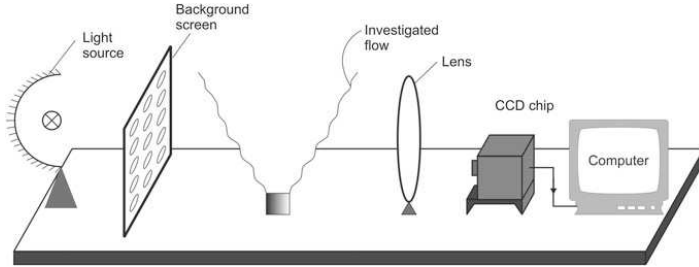


Figure 3.6: Typical BOS scheme. An optical ray passes through a phase object and its displacement is compared with the undistorted imaging ray [28, p.37].

The differences between *Background Oriented Shlieren* (BOS) and other techniques are the key role of numerical methods, the high accuracy, the smaller number of optical equipment, the bidirectional sensitivity, the fast evaluation and the missing field limitations. Some experimental studies show the applicability in a lot of

cases, like turbulent jets, supersonic jets, shed vortexes and many more [22][21].

The latest achievements in BOS techniques have been gained by NASA [49]. Their innovative approach consisted in generating the background speckle pattern by displaying it on a high definition 4K HD monitor. This technique presents three distinct advantages: no need to physically construct the speckle pattern, scale of the speckle pattern readily settable and simplified implementation in confined environments. This technique was an essential element for the studies of *Altitude Combustion Chamber* (ACS) at NASA GRC (see Fig.3.7).

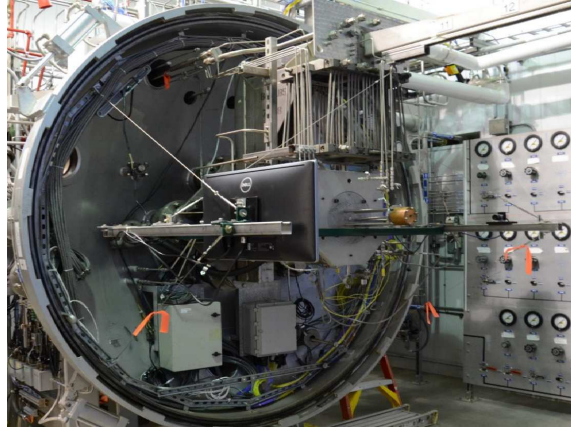


Figure 3.7: BOS installation in ACS, the camera views the background image on the monitor through the nitrogen gas simulated rocket exhaust plume [49].

The BOS constitutes an interesting alternative to conventional schlieren techniques. On the other hand, the lack of information about its efficiency on windows for combustion chambers with optical access and the limited resolution (lower than comparable traditional schlieren instruments [35]) discourages its utilization in this project.

## Laser Schlieren Techniques

These techniques involve a laser as the system light source [28, p.6], instead of a typical tungsten filament lamp (often called in literature "conventional light source"), which filament emission is random in time, spatially distributed, and photon energies are distributed over several wavelengths. In contrast, a laser output is:

- monochromatic;                      – directional;
- intense;                                – coherent;

Using a laser as light source implies the serious issue of camera saturation. In alternative, a white LED source is often used in the context of schlieren, since light coherence is not strictly a matter of concern for our purposes [28, p.25].

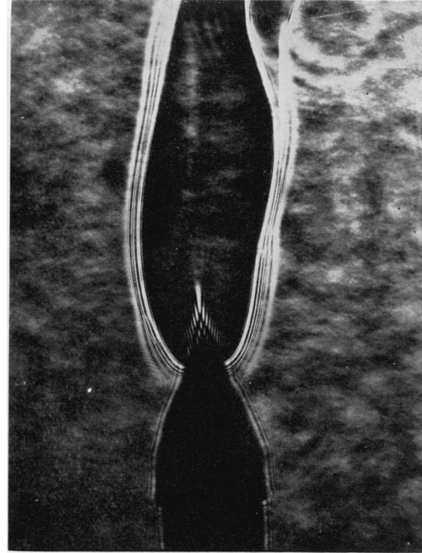


Figure 3.8: Parallel beam shadow of a flame illustrating diffraction effects obtained by a laser source [26].

### 3.1.2 Project Requirements

The Technische Universität München (we will refer to TUM as the *customer* from here on) commissioned a schlieren system for a mobile rocket combustion chamber. This request involves some specific tasks, while others were imposed by the author in order to arrange in advance a valid solution for future applications. The following are the project requirements that helped to define the guidelines for the project.

- **Accuracy:** the system should result as most precise as possible, in order to avoid the most of numerical errors coming from an inaccurate image detection;
- **Compatibility:** the system must properly adapt to its object of study (MoRaP<sup>2</sup>), which implies that it has to manage self-luminous phenomena (i.e. combustor flame) and to adapt to glass windows of the chamber (see Appendix B). It also has to be compatible with a pre-existing *chemiluminescence* image analysis system;
- **Compactness:** the global size of the system should be limited, in order to stock it and make it able to operate next to other equipments, already located in the test

---

<sup>2</sup>Mobile Rocket Combustion Chamber Test Bench

facility. Furthermore, since test campaigns are usually carried out in a specific area of the facility due to safety reasons, the space available for the storage of the system is restricted even more;

- **Affordability:** the system should lower its assembly cost by implementing as much components currently present in the facility as possible, with exception of irreplaceable optical components for the schlieren analysis;
- **Versatility:** optional feature which allows to use the system for future tasks, different from the one for which it was conceived in the first place. This feature could turn the schlieren system in a valid resource for many future applications;
- **Intuitiveness:** optional feature which allows the operator of the system to focus on his test campaign, instead of struggling with a harsh system calibration. This feature could encourage the usage of the system also from an operator who usually has no previous knowledge of the optical principles of the system;
- **Portability:** optional feature which allows to easily move the system and its components in case that it has to be dismantled from the facility. In order to achieve a non-destructive procedure, the system should be conceived in a *modular* perspective, so that the alignment of its components could result as easy as possible to replicate;

## Conclusions

The best candidate is a *Z-type 2-parabolic-2-flat-mirror schlieren system* (see Fig.3.9). This configuration represents the best compromise between all the project requirements. The system and its components will be described in detail in the following sections.

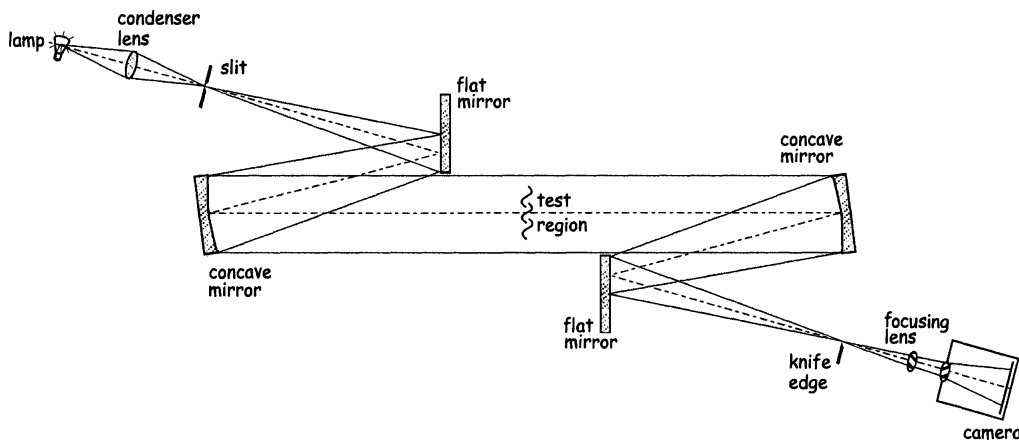


Figure 3.9: Example of a possible fully-functional *Z-type 2-parabolic-2-flat-mirror schlieren system* configuration, designed for quantitative-evaluation of refractive-index variations.

## 3.2 Preliminary Design

During this *preliminary design* phase, a unique best-candidate configuration is taken into account, while the other dead-end configurations that were previously considered along the design process are handled while describing the definitive design solutions adopted. This configuration will rely on a *Z-type 2-parabolic-2-flat-mirror schlieren system* (see Fig.3.9), which constitutes the best compromise between all the project requirements. Furthermore, there is a lot of reference material about its assembly procedure and operational costs. It is also very intuitive to calibrate, offering the best solution in terms of accuracy, compactness, affordability and compatibility with the Mobile Rocket Combustion Chamber Test Bench (we will refer to it as *MoRaP* from here on).

### 3.2.1 List of Components

#### Light Source Block

This block is responsible for generating the controlled light beam. All of its components are mounted on a breadboard plate that is able to rotate around its vertical axis.

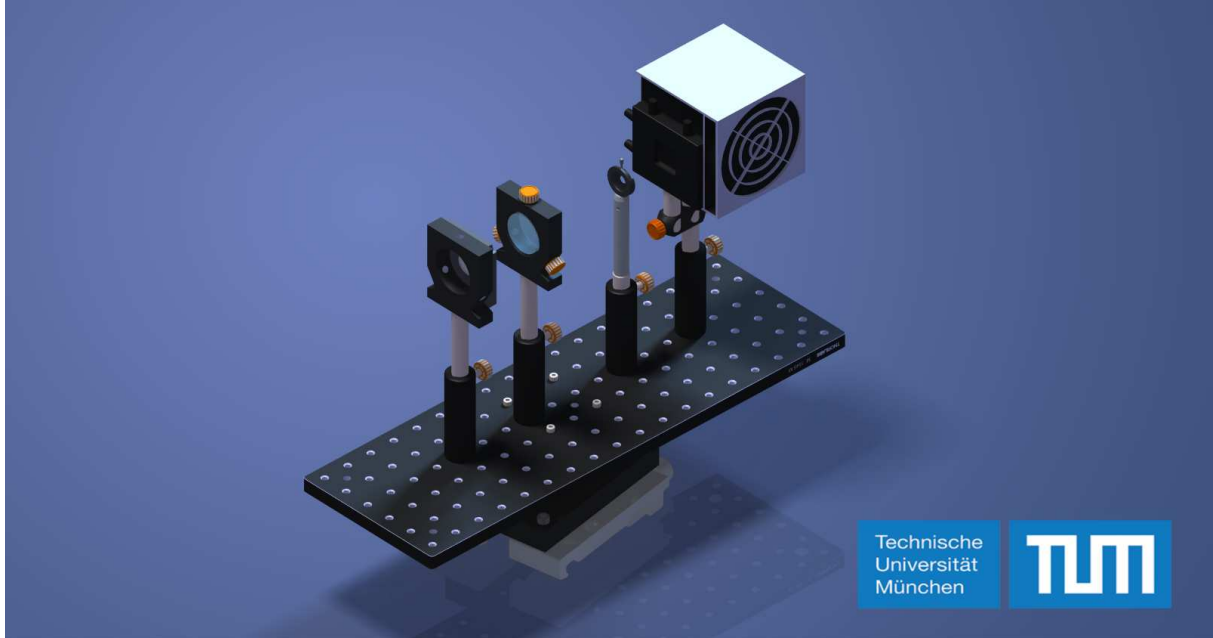


Figure 3.10: *Light Source Block* CAD model.

This choice was dictated by the necessity to optimize the *tilt angle*  $\theta$  in the advanced *detail design* phase, but it is optional for the final operator, which is free to fix the block to a specific angle, once that the system has been calibrated.

**LED Lamp** The *light emitting diode* (LED) lamp is the ideal non-coherent light source for schlieren application [35]. It is a cheap solution, that gives great results in returns. The choice is between a large variety of wavelengths for special purposes, but one can get the best resolution from a non-coherent phosphor-conversion "white-light" LED lamp (slightly bluish, indeed). These lamps have the ability to pulse repeatedly down to a  $100\text{ ns}$  range [47][52][53], which is better than other non-coherent light source and for a cheaper price. Unfortunately, many of the specifics about the LED lamp already present in the facility (such as the projection-angle of the beam or the *candela* luminous intensity) were lost, so that many characteristics of the emission had to be estimated. This also implied the impossibility to directly use the LED at the focus of the 1ST concave mirror and then to eliminate [34] the condenser and slit (see below), nor allowing to combine the slit with the LED source in close contact upon emitter size and shape, because of the actual LED lamp support casing.

**Condenser Lens** In Fig.3.9 and in Fig.3.11 one can distinguish the *condenser lens*, which focuses the LED lamp light beam upon a *source slit*. This solution actually crops the irregular intermediate image of the source, producing a regular and approximately-uniform light beam, which complexively improves the sensitivity of the optical system [44]. The ideal f/no. (*f-number*<sup>3</sup>, or *focal ratio*) should be identical to the f/no. of the 1ST concave mirror, in order to perfectly fill the schlieren field. On a more practical approach, this is unwise, because of the reduced illumination near the periphery of the light beam due to the finite size of the

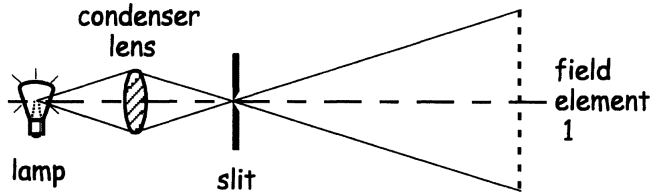


Figure 3.11: A scheme of the light source block [34, p.173].

source slit [32]. Vasiliev [46] suggests a condenser f/no. around  $1.5 \div 2$  times smaller than the 1ST optical element, which translates in a  $f/4$  condenser lens in our arrangement (for further information, consult the paragraph about the *concave mirrors*), moreover the lens should be both spherical and free from chromatic aberrations. In this way, some compromise is necessary in the interest of economy [34]. The final arrangement will implement a near to  $f/2$  double-element a-spheric condenser, efficient at light collection and inexpensive, since its components were already stocked in the facility.

<sup>3</sup>The f-number  $N$  is given by:  $N = f \cdot D$ , where  $f$  is the *focal length* and  $D$  is the *diameter* of the optical element; e.g. if a lens's focal length is 10 mm and its diameter is 5 mm, the f-number is 2, expressed by writing "f/2".

**Source Slit** The choice of this component can be very restrictive. Its shape is not relevant [44], as long as there is one straight edge corresponding to the knife-edge cut-off,

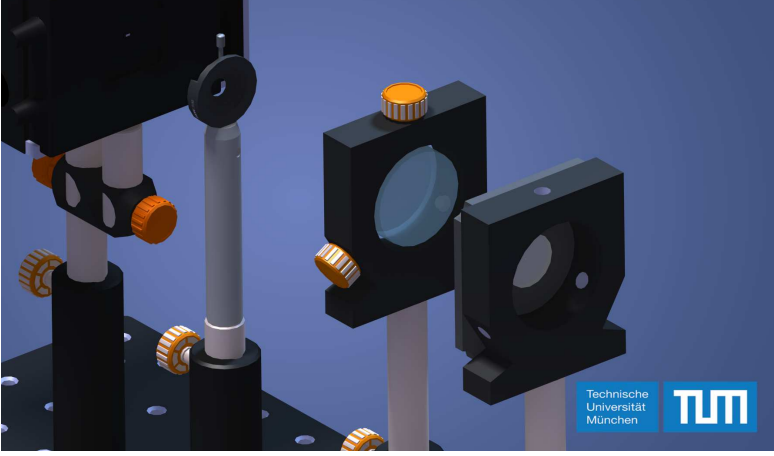


Figure 3.12: Detail of the Light Source Block CAD model. Starting from the left, we find the *LED lamp*, the *light-amount regulator*, the *condenser lens* and the *widened source slit*.

but it is universally recognized that a sharply-defined effective light source is a good solution [34, p.174]. Unfortunately, this condition requires a specific component that was originally in place, but then has been moved to the knife-edge filter, because of its precise regulation level, and substituted by a combination of *light-amount regulator* and *widened source slit* (see Fig.3.12). The first is

placed along the optical path but far from the focal point, while the second is placed at the focal point. This widened source slit leaves the light pass undisturbed [34, p.173] and its main function is to identify the focal point along the optical path. Nevertheless, the use of the light-amount regulator ensures a very sharp image at the focal point, but its dimension  $a_s$  inherits a certain degree of uncertainty. It was not possible to re-arrange the regulator itself as the slit, because of its wide aperture and its weak enclosure regulation mechanics, that could easily loose the calibration and nullify the efforts. In order to proceed with a numerical evaluation, the source dimension  $a_s$  has been estimated at the focal point, assuming a  $\sim 0.1 \text{ mm}$  order of approximation, which is still relevant.

## Mirror Setups

**Concave Mirror Model** This optic is a pivotal element for the entire test rig. The wavelength range of the mirror should result between  $380 \div 740 \text{ nm}$  (visible-light spectrum). Its diameter should exceed the combustion chamber windows extension at least (see Appendix B), which means more than  $4 \text{ cm}$  of diameter. An  $f/\text{no.}$  greater than  $f/6$  is strongly recommended [34, p.46], indeed the usual range in Z-type schlieren systems is  $f/6 \div f/12$ , but a bigger  $f/\text{no.}$  would also imply a bigger space for the rig, which is a parameter we are trying to keep as low as possible. This different necessities will lead to a near- $f/10$

concave mirror model, which is a compromise between tilt angle minimization and the biggest FL tolerated. Furthermore, larger-f/no. mirrors save the system from *astigmatism* (see Sec.4.2 at p.65), while larger FL ensures a higher *sensitivity* (see Eq.2.15 at p.13). Moreover, a  $3\lambda/2$  surface accuracy ensures good image quality and small focused spots. The model chosen for this project is the *20DC1000ER.1* (by *Newport*<sup>®</sup> [23]), an *enhanced aluminium concave mirror*, 500 mm EFL and 50.8 mm diameter, chromatic-aberrations-free and designed for 450 – 700 nm wavelengths. All further specifics are reported in Tab.3.1.

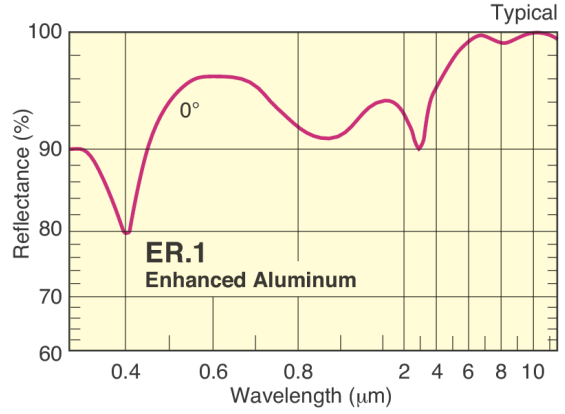


Figure 3.13: 20DC1000ER.1 concave mirror reflectance (%) vs. wavelength ( $\mu\text{m}$ ) [23].

20DC1000ER.1	Technical Specs
Wavelength Range	450 – 700 nm
Mirror Shape	concave
Diameter	50.8 mm
EFL	500 mm
f/no.	9.8
Radius of Curvature	–1000 mm
Material	Borofloat <sup>®</sup> 33
Coating Type	Enhanced Aluminium
Coating Code	ER.1
Surface Quality	40-20 scratch-dig
Surface Flatness	$\lambda/4$ at 632.8 nm
Center Thickness	9.21 mm
Angle of Incidence	0 – 15°
Back Surface	Fine ground
Reflectivity	$R_{avg} > 93\%$ , $R_{min} > 90\%$ @ 450 – 700 nm
Damage Threshold	0.5 J/cm <sup>2</sup> with 10 ns pulses @ 532 nm, 20 Hz
Edge Thickness	9.65 mm
Thickness Tolerance	$\pm 0.25$ mm
Diameter Tolerance	+0/– 0.13 mm
Chamfers	0.25 – 0.76 mm face width
Chamfers Angle Tolerance	45° $\pm$ 15°
Wedge	$\leq 0.03$ mm
Cleaning	Clean-air duster Glass-cleaning solvents

Table 3.1: 20DC1000ER.1 *technical specifications* [23].

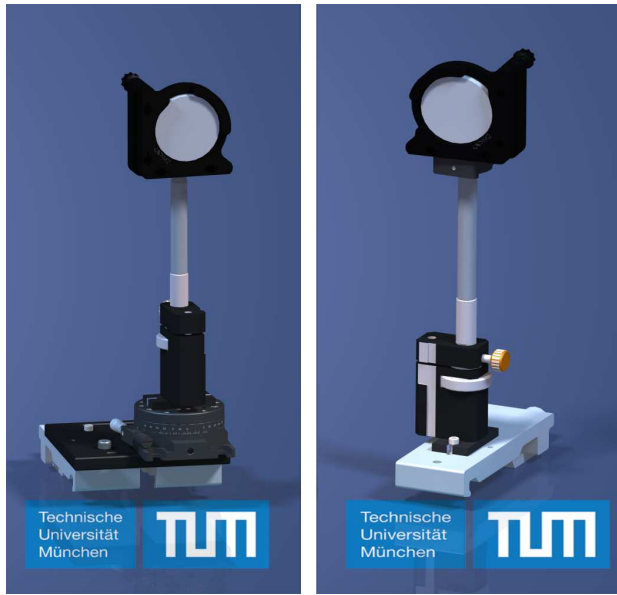


Figure 3.14: *1ST concave mirror support* (left) and *2ND concave mirror support* (right) CAD models.

**Concave Mirror Support** The 1ST and 2ND concave mirrors are identical, in order to avoid any scaling side-effect [28, p.25]. Their supports, instead, are different due to an higher need for precision on 1ST mirror calibration procedure (consult Sec.4.1.1) and for lack of components availability in the facility. For future application, the 2ND concave mirror support could replicate the support of the 1ST concave mirror in order to simplify the calibration procedure and to increase the precision of the system. This choice was dictated by the necessity to optimize the *tilt angle*  $\theta$  in

the *detail design* phase. A freely settable angle is optional for the operator, who is free to fix the left block to the specific  $\theta$  value, once that the system has been optimized.

**Flat Mirror Setups** This components are fully functional, but temporary arranged with pre-existing setups in the interest of economy. The best-candidate, in terms of quality and compactness for future applications, is the *20SJ00ER.3* (by Newport® [24]), an *utility broadband metallic mirror*, optimized for 400 – 10000 nm and free from chromatic aberrations.

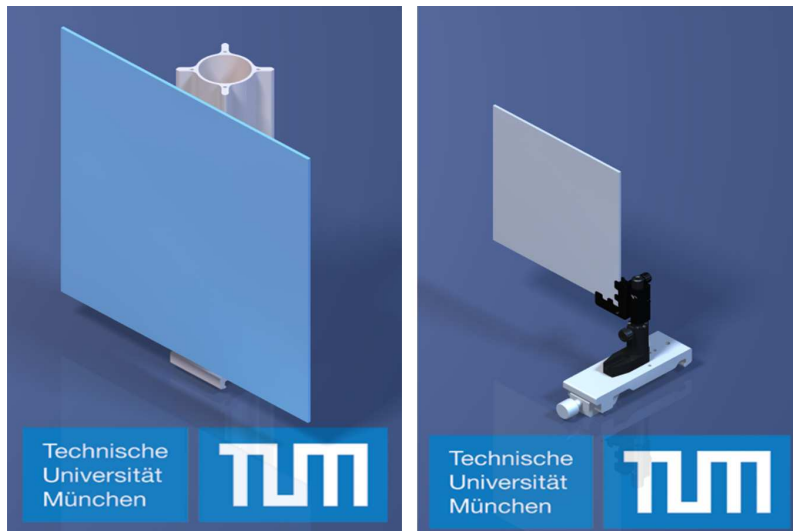


Figure 3.15: *Actual* (left) and *future* (right) *flat mirror setups*, CAD models.

This model is an excellent and economical broadband reflector, suitable for many applications. In Tab.3.2 will follow the technical specifics for this model (unfortunately, the tech-specs for the actual flat mirror configuration are unknown).

20SJ00ER.3	Technical Specs
Wavelength Range	400 – 10000 $nm$
Mirror Shape	square
Mirror Size	50.8 $\times$ 50.8 $mm$
Material	Float Glass
Coating Type	Enhanced Aluminium
Coating Code	ER.3
Surface Quality	60-40 scratch-dig
Surface Flatness	5 $\lambda$ per inch at 632.8 $nm$
Back Surface	Polished
Reflectivity	$R_{avg} > 90\%$ @ 400 – 700 $nm$
Thickness	3.17 $mm$
Thickness Tolerance	$\pm 0.76$ $mm$
Size Tolerance	$\pm 0.25$ $mm$
Cleaning	Clean-air duster Glass-cleaning solvents

Table 3.2: 20SJ00ER.3 *technical specifications* [24].

## Camera Block

This block is responsible for cutting-off the refracted light rays through a knife-edge filter, then a CMOS camera collects on file the images incoming on its sensor.



Figure 3.16: *Camera Block* CAD model.

**Knife-Edge Filter** A schlieren object can be observed only if its deflected beams pass through a knife-edge filter, which should present a very sharp edge, in order to cut-off the amount of light specified by its placement along the optical path. A knife-edge filter affects only ray-refractions with components perpendicular to it [34, p.33]. Indeed, it has to be mounted orthogonally to the direction for the quantities-gradients evaluation (e.g. filter in vertical stand for evaluations of horizontal quantities-variation and vice versa). The actual setup has been tested for evaluation along the x-axis (main direction of the longitudinal combustion chamber, from the igniter to the nozzle), along which the most interesting variations occur, but it is predisposed also for measurements along the y-axis (from flame center-line to walls).

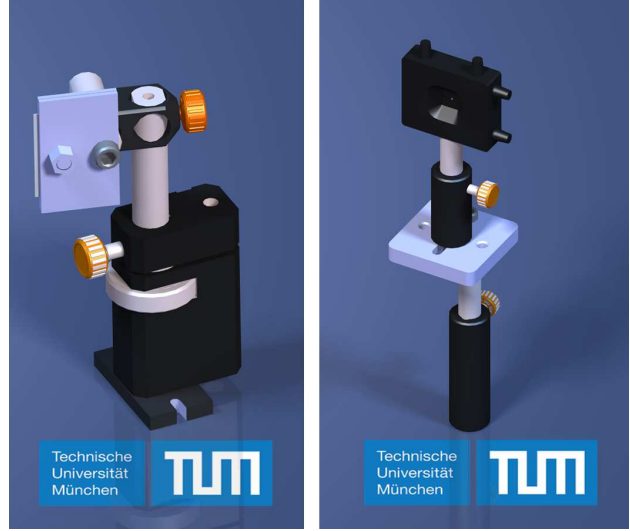


Figure 3.17: Preliminary concept (left) and definitive version (right) of the *knife-edge filter*, CAD models.

The calibration of a knife-edge filter (its position along the optical axis and orientation) plays a significant role in the quality of the image recorded. With the best alignment, the light beam should form a spot on the filter, whose dimensions match the source slit extension ( $a_s \equiv a_0$ ), avoiding any scaling effect induced by different focal lengths [28, p.25] (chosen mirrors present identical FLs  $f_1 = f_2$ ).

Once that the sharp edge of the filter reaches the focal point, the cut-off regulation turns into uniform darkening nor lighting of the image over the screen [28, p.25], in accordance with the theoretical concept exposed in Sec.2.1. If this is not the case (see Fig.4.5 in Sec.4.2 at p.68), then further calibration is necessary.

The cut-off amount regulates the overall *sensitivity* of the system (greater cut-off means greater sensitivity), but also determines the exposure of the image. It is necessary to find a compromise between image illuminance and request for sensitivity, but this constitutes a merely empirical practice, that will be carried on during the experimental sessions. A 50% cut-off amount is the minimum value to appreciate any sensitive variations [12], but a 80-90% is more common for schlieren evaluations (Settles points the ultimate sensitivity gain near to a 95% cut-off amount [34, p.72], then irreparable *diffraction* errors will occur).

Typically, a Z-type schlieren system is slightly affected by *astigmatism*<sup>4</sup>, that is the separation  $\Delta f$  between focal points for horizontal and vertical gradients evaluations

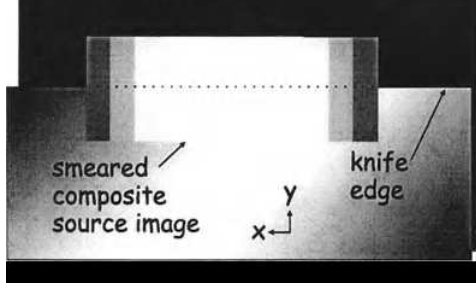


Figure 3.18: *Tangential focus* in a Z-type schlieren system, horizontal smearing of a rectangular source image while applying a horizontal knife-edge filter for vertical evaluations [34, p.45].

(respectively named *sagittal* and *tangential foci*, see Fig.3.18), resulting in the smearing (or spreading) of the elemental source images along two short lines near the focus of the 2ND mirror [34, p.45]. The point where the image is circular is known as the *point of least confusion* [29, p.2], which has not to be confused with the focal point of the 2ND mirror. When strong *astigmatism* occurs, any attempt to mask the light beam in both perpendicular directions at the same time is discouraged, while a separated analysis for horizontal and

vertical gradients evaluation is more recommended (further details on calibration in Sec.4.2 at p.68). A good practice to avoid *coma* and to limit *astigmatism* (hereditary defect of any Z-type configuration) is to adopt the minimum practical *tilt angle*  $\theta$  value (angle optimization is carried on in the *detail design* section) and to work only with mirror with f/no. of 6 or greater [34, p.46].

The knife-edge filter preliminary concept (see Fig.3.17 on the *left*) was less intuitive to calibrate and the regulation of the cut-off amount eventually risked to nullify the efforts for previous calibration. Its definitive version (see Fig.3.17 on the *right*), on the other hand, can cosily slide on a plane support and then be fixed, in order to find the focal point along the optical axis. Its regulation mechanics is very solid and intuitive, making easier for the final operator to set the cut-off amount.

**Focusing Lens** This optical element, placed between the knife-edge filter and the CMOS camera, allows one to control the image size independently from the distance in between. Indeed, without a focusing lens the *magnification factor* [34, 73] (ratio of image to test-area diameters) would depend from the actual distance  $(s + f_2)$  between the schlieren object in the test region and the 2ND concave mirror (see Fig.3.19), which has to be at least slightly longer than  $f_2$  itself, in order to visualize the schlieren object on focus.

<sup>4</sup>The distance between sagittal and tangential foci is an index of *astigmatism* severity. It is estimated by the formula:  $\Delta f = f \cdot \sin^2 \theta / \cos \theta$  [41][37], where  $f$  is the FL of the mirror and  $\theta$  is the *tilt angle*. E.g. f/8 parabolas having  $D = 10.8 \text{ cm}$  and  $f = 86.4 \text{ cm}$  yields  $m = 2.4 \text{ mm}$  for  $\theta = 3^\circ$ . Larger-f/no. mirrors would permit smaller angles  $\theta$ , which leads to minimized astigmatic separation.

The arrangement in Fig.3.19 returns the expression for the *magnification factor*:

$$m = \frac{f_2}{s}$$

This is usually inconvenient, since the distance  $s$  grows large in order to demagnify the image, so that the overall length of the optical train becomes unwieldy [34, p.73].

On the other hand, a focusing lens would allow to regulate the distance independently from the growth of the distance  $s$ , which is not negligible due to the necessity to host the combustion chamber inside the test chamber. The distance  $g$  should be minimized in order to keep small the light beam diameter compared to the camera lens aperture ( $\sim 5\text{ mm}$ ), which means a  $m$  value close to 0.1 for a  $D = 50.8\text{ mm}$ . The minimum value of  $g$  is  $\sim 5\text{ cm}$  due to mounting constraints of the schlieren system. In this case, the thin-lens approximation yields the following expressions [12] for  $f_3$  of the focusing lens and distance  $e$  from the camera sensor:

$$f_3 = \frac{m(f_2^2 - s g)}{f_2 - m s} \quad , \quad e = m \left( f_2 - \frac{s g}{f_2} \right) \quad (3.1)$$

Eqs.3.1 may come in help during a preliminary modelling of the camera block. The setup definitive version will show a separation between focusing lens and camera lens, due to the necessity to work with a *prime lens* (a fixed focal length photographic lens, opposed to a *zoom lens*) for the CMOS camera, with short FL (25mm). To obtain the searched  $m$  factor only by using *extension tubes* would lead to a dramatic drop in the exposure level, while an external lens helps preventing this inconvenience. This leads to a separation between focusing lens and camera lens, which allows a certain degree of freedom in the choice of the f/no. of the focusing lens mostly, dictated by the preservation of image quality and resolution. As consequence, the ideal match between focusing lens and CMOS camera images comes from an empirical troubleshooting procedure, which takes into account exposure level and focus on both the schlieren field and to infinity (for further details see Sec.4.1.2 at p.61, in **Camera Calibration & Setting** procedure). In routine schlieren photography, the focusing lens can be either mounted separately on the optical bench, or else can be used a C-mount adapter to mount a wider-aperture 35mm prime lens or zoom lens to the camera body [34, p.189].

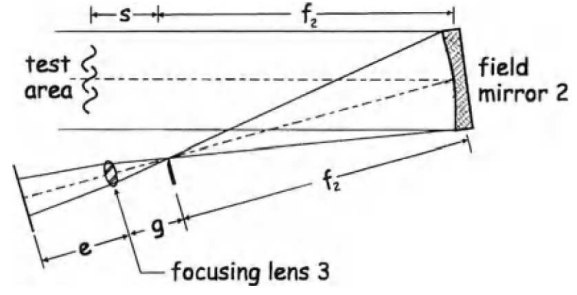


Figure 3.19: Diagram of 2ND mirror field, notations for *magnification factor* and focusing lens [34, p.73].

**CMOS Camera Setup** The adopted camera for the schlieren analysis is a *Toshiba BU205M* (Fig.3.20a), an integrated-(one-body)-type camera that mounts a global shutter CMOS<sup>5</sup> sensor. Its best features are a *high frame-rate* (170fps), a *global electronic shutter* (similar to a CCD image sensor) for clear images even for fast-moving objects and an *USB 3.0 interface standard* for high transfer rate. All further details are reported in Tab.3.3.

BU205M (B/W model)	Technical Specs
Imager	CMOS image sensor
Number of effective pixels (H)×(V)	2048 × 1088
Optical Size	2/3" type
Scanning area (H)×(V) [mm]	11.26 × 5.98
Pixel size (H)×(V) [ $\mu\text{m}$ ]	5.5 × 5.5
Scan method	progressive
Electronic shutter method	global shutter
Aspect ratio	2:1
Standard subject illuminance	3800lx @ F8,1/200s
Minimum subject illuminance	8lx @ F1.4,Gn(x8),VL(50%)
Interface	USB 3.0 (Only SuperSpeed is supported)
Transmission speed (max)	5Gbps
Image format	mono 8bit
Frame-rate (max)	170fps @ VL(100%)
Lens mount	C-mount
Exposure time (min,max)	30 $\mu\text{s}$ , 16 s
Gain (min,max)	×0.00 [times] , ×8.00 [times]
Black level (min,max)	-25 [%] , +25 [%]
Gamma (min,max)	0.45 , 1.00

Table 3.3: Toshiba BU205M *technical specifications* [45].



Figure 3.20: Pictures of the components for the camera setup.

<sup>5</sup> *Complementary Metal-Oxide-Semiconductor*, the CMOS sensor has emerged as an alternative to *Charge-Coupled Device* (CCD) image sensors.

The FL of the lens should be selected in accordance to the camera-to-schlieren-object distance. As consequence, in the 50-300mm distance range a 35mm zoom lens finds frequent application [34, p.189]. This should not surprise<sup>6</sup>, despite the misconception that schlieren photography works only with long FL optics (more suitable for parallel light beams falling on the camera sensor), since on this 2/3" camera sensor a remarkable *crop-factor* is involved. Indeed, on a 2/3" optical size camera (see Tab.3.3) a 35mm lens is equivalent to a 138mm lens on a *35mm equivalent focal length scale* (indeed, *crop-factor* is 3.93 [50]). The camera lens adopted is a *Tarcus TV-Lens 25mm F1.4* (see Fig.3.20b), which FL may affect negatively the results for schlieren photography but, rather than move to a different solution and take new expense into account, it seems worth to correct this issue by adopting an efficient and cheaper *extension tubes* solution (see Fig.3.20c and Fig.3.21). With a 30mm extension tube, the overall FL goes to 55mm (a 216mm on a 35mm equivalent focal length scale, which gives back results close to a *telescopic lens*). This 30mm extension tube is worth also due to exposure needs. All the exposure regulation procedures are discussed in the *practical issues* section in the calibration chapter (see Sec.4.2 at p.70).

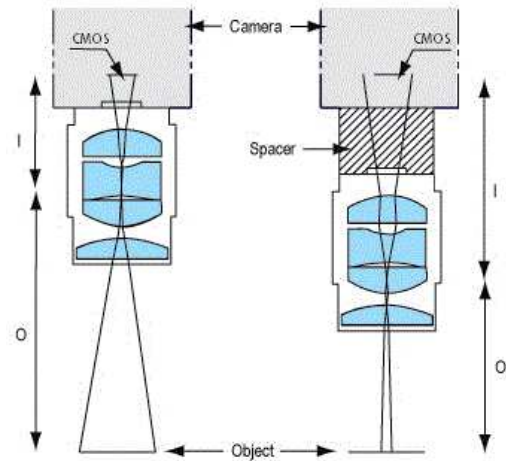


Figure 3.21: Effect of an *extension tube* on overall FL [9].

### 3.2.2 Cost Analysis

The definitive configuration of the system has already been examined, but it is important to stress that, at first, the choice on the *20DC1000ER.1 enhanced aluminium concave mirror* (by Newport® [23]) was not so obvious. Indeed, it was necessary to probe the market in search of valid alternatives from different suppliers and then to draw up a technical comparative between all the possible arrangements. It constitutes a necessary practice, dictated by TUM policies, in order to ensure the best purchase in terms of cost-benefits. The competitors have been chosen by taking into account their reliability on the market, as well as affinity with the choice on components and materials for the system.

<sup>6</sup>Usually, on a standard 35mm full-frame film sensor, a 35mm FL optics results as a wide-angle lens (covers the angle of view between 64° and 84°).

The official request-for-supplies document carried on a comparative between products from Newport® and two other competitors, whose names will be left out from the following description (purpose of this section is only to delineate a *methodological procedure*). The comparative between the offers from the suppliers is summarized in Tab.3.4 and Tab.3.5.

Concave Mirror and Mount		(Newport®)
Concave Broadband Metallic Mirror	50.8mm Ø, 500 EFL, 450-700nm	-
Standard Aluminium Mirror Mount	50.8mm Ø, 2 Knob Actuators	-
Concave Mirror and Mount		(alternative I)
Plano-Conc. Lens , fused silica	25.4mm Ø, 500 EFL, 450-700nm	-44.75 %
High Precision Lens Holder	MA - 1" Ø M	+337.46 %
Concave Mirror and Mount		(alternative II)
Dielectric-Coated Concave Mirror	75mm Ø, 500 EFL, 400-750nm	-6.26 %
Laser High Prec. Mirror Mount	3" Ø, 2 Adjusters (Side Holes)	+540.14 %

Table 3.4: Concave mirror and mirror mount components *comparative* from different suppliers (differences in price reported at *time of purchase*).

	(Newport®)	(alternative I)	(alternative II)
<b>Total Price</b>	-	+74.20 %	+147.69 %

Table 3.5: Total price quotation *comparative* for concave mirror and mirror mount components from different suppliers (differences in price reported at *time of purchase*).

From the comparative in Tab.3.4, one can notice a coherent price diminution for the half-diameter-length concave lens from **alternative I**, but there was no model that could satisfy the dimension request (at least 5 cm Ø), moreover the holder was overpriced due to its higher precision (not specifically requested). It is also worth to notice that fused silica lenses are often more sensitive to chromatic aberration than metallic mirrors in general. For what concerns **alternative II**, despite of its interesting diameter-price rate, the high precision mount support is definitely overpriced for our purposes (more suitable for laser-optics application than schlieren). As long as no other compatible mount system has been found from the same supplier, in according to the *overall prices* comparative from Tab.3.5 and privileging a purchase from a single supplier (as requested by TUM policy), the **Newport®** solution is confirmed as the best purchase in term of cost-benefits. All the other components for the actual schlieren arrangement have been adapted from material previously furnished by LFA, already present in the facility.

### 3.2.3 Sizing

The overall structure dimensions depend directly from the MoRaP size (see Appendix B), which requires at least  $800\text{ mm}$  to let the bench test pass through the accessible area. The original MoRaP was a rectangular combustion chamber with a single optical access on the top side (see Fig.3.22). In the updated version, it will keep its peculiarities, but will also present two additional optical accesses in order to let a straight light beam pass through, in order to conduct schlieren diagnostics. For this purpose, a U-shaped basic *system structure* (see Fig.3.23a) has been designed, made in aluminium structural rails, which offer both solidity and resistance to vibrations (includes vibration-absorbers *levelling feet*). Along its extremities, two *mounting brackets* (see Fig.3.23b) are able to slide to the requested x-coordinate. On their rails, the *light source block*, *concave mirror mounts* and *camera block* are set up, while the *flat mirror mounts* are placed directly on the structure and free to slide along x-axis.

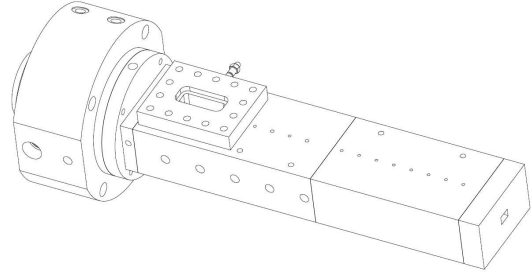
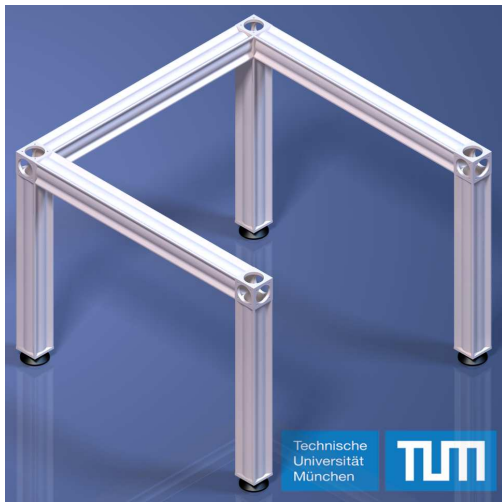
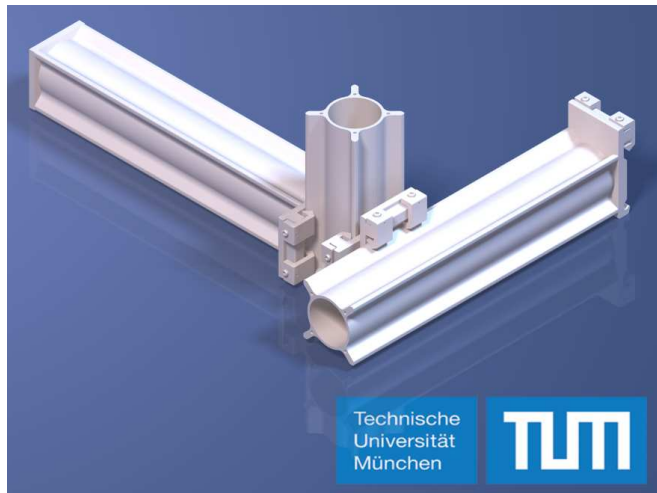


Figure 3.22: Isometric view of the MoRaP (*previous version*), special thanks to M.Sc. F. Winter.



(a) U-shaped basic *system structure*.



(b) (Left-side) *mounting bracket*.

Figure 3.23: CAD models from the *schlieren system* aluminium rail structure.

The test-area size allowed by the structure is  $1000\text{ mm}$ , enough to let the MoRaP pass through undisturbed and with a discrete manoeuvring margin. This choice was also driven

by the necessity to reduce the sensitivity of the system to self-luminous phenomena<sup>7</sup>, which often affect optical studies on flames. Indeed, the schlieren photography takes advantages from extending the distance from the self-luminous event (e.g the flame of a combustor) to the 2ND mirror. On the other hand, this may increase the magnification of the image, but this issue has been solved by implementing a focusing lens (see Sec.3.2.1 at p.37).

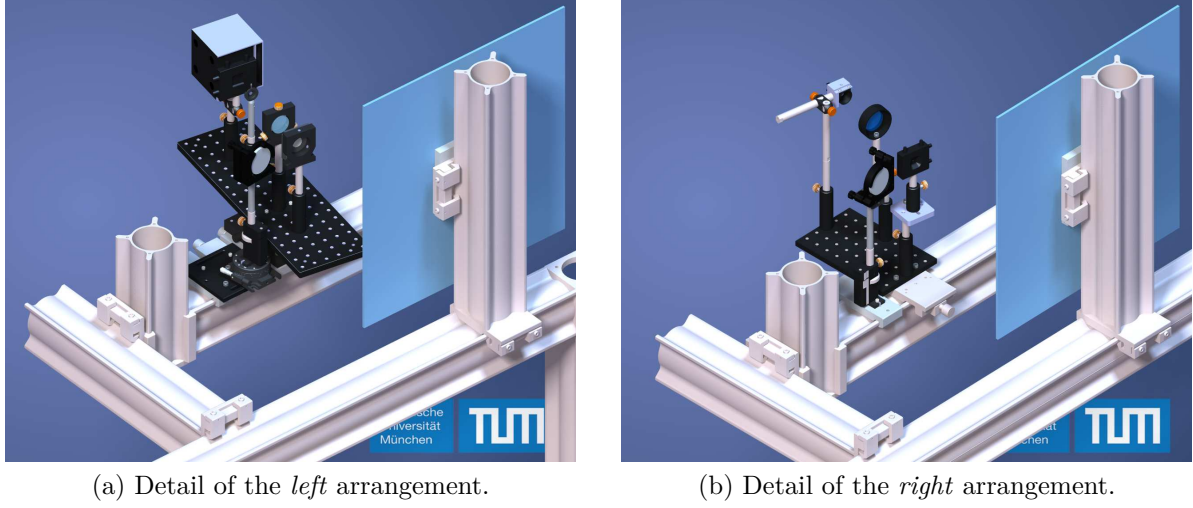


Figure 3.24: CAD models from the definitive *schlieren* system.

The standard height for the rails of the mounting brackets is  $895\text{ mm}$  from the floor, but it can slide for a  $\pm 155.5\text{ mm}$  range. All the optical components can be fixed to a common height (need to calibrate just once, see Sec.4.1.1), then the whole support can be regulated to a specific height (and x-coordinate), in order to align with the object of study. This approach saves a considerable amount of time by facilitating the calibration procedure for the operator. Moreover, it enhances the constructive quality of the system, because predisposes it for a wider range of future applications and makes it a valid instrument for the LFA research projects that could take advantages from a schlieren investigation.

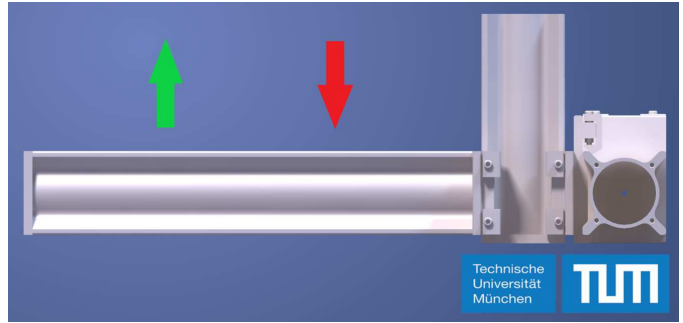


Figure 3.25: Regulation excursion ( $\pm 155.5\text{ mm}$ ) of the mounting brackets, CAD model.

<sup>7</sup>According to Kean [18], the illuminance of a schlieren image is  $E + E^*$ , where  $E^*$  is the component not due to refraction but generated by self-luminous phenomena (e.g. flames, shock-waves, heating radiation, etc.). Increasing the distance from the self-luminous object to the 2ND mirror reduces the aperture angle of extraneous light captured by the system [12].

### 3.3 Detail Design

The *detail design* phase has to finalize the optimization and micro-calibration of the configuration delivered by previous preliminary design phase. At this point, all the system components are putted in place and need to be tested, in order to confirm the choices carried on during the *detail design* phase, so that the system configuration can be fixed and delivered to the customer as a fully working machinery for schlieren evaluative diagnostic.

#### 3.3.1 Tilt Angle Optimization

The *tilt angle*  $\theta$  is the most influential parameter for a high precision schlieren system, as long as most of the optical errors, such as *astigmatism* (see Sec.3.2.1 at p.3.2.1), are due to an excessively broad tilt angle of the concave mirrors. A mirror-based schlieren system avoids chromatic aberration, but the phenomenon of double-passing of light necessarily occurs as consequence. The best way to limit the errors coming from this arrangement is to adopt the smallest practical tilt angle reachable [1], for both concave and flat mirrors, and to assume a Z-type configuration, in order to get rid off *comatic aberrations* (see *coma* in Sec.4.2 at p.4.2). This approach saves also the system from strong *astigmatism* affections (even if it is never completely avoidable on Z-type configurations).

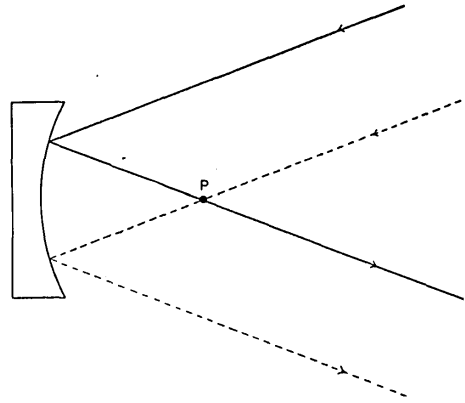


Figure 3.26: Point of double passage of light in the striation region [1].

#### Matlab® Routine for Geometrical Construction

Rather than proceed with a practical troubleshooting approach, a more methodological procedure is encouraged, which involves a Matlab® routine (consult *attachments*), properly written with the purpose of modelling the schlieren system and its components. It works by virtually varying the tilt angle  $\theta$ , into a reasonable range of values for these applications, and then applying a verification process in three steps, in order to validate the best-candidate  $\theta$  value. In other words, the troubleshooting procedure has been conducted virtually, saving a considerable amount of time and returning a  $\theta$  value pretty much close to those advised by Settles [34, p.205] for this kind of arrangement.

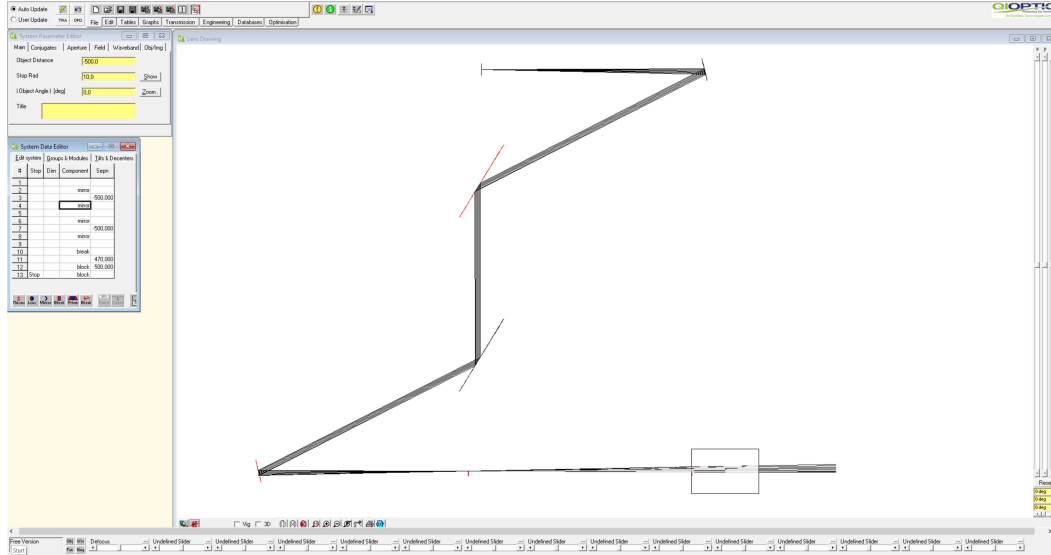
The *Matlab® Routine for Geometrical Construction* has been adapted separately for the left side (*light source block* and *1ST concave mirror*) and for the right side (*2ND concave mirror* and *camera block*) of the system. Here will follow a short description of the verification methods adopted for the tilt angle optimization:

- **Physical Interference Verification:** This procedure ensures that none of the physical components mounted on the brackets overlaps with one another after changes in the relative distances, as consequence to an excessive  $\theta$  reduction. Its optimization efficiency is limited by the mounting supports of each component and could be improved in future by adopting less bulky mount systems. Thanks to its high fidelity modelling, this verification procedure requires a quite small *margin-of-safety* (MS);
- **Light Interference Verification:** This procedure avoids any interference between the straight light beam, coming from the concave mirror and directed to the test region, and the flat mirror that previously reversed the beam incoming from the light source. Due to the assumption that the light beam projects itself on the flat mirror in a half-sized diameter shape, with respect to the concave mirror diameter (which may not be correct at all), this verification procedure requires a higher MS, in order to take this hypothesis into account during the modelling of the optical system;
- **Consistency Verification:** This procedure validates the geometrical model, which simplifies the optical path into sides of equal length of an isosceles triangle. Each side measures exactly half the FL of the concave mirrors, while half the vertex angle measures  $2\theta$ . The procedure validates the fidelity of the model by evaluating the maximum variance of the optical components actual position relatively to the common axis, resulting from the geometrical construction and base of the isosceles triangle. If this variance  $\pm d_{var}$  is too high, then the tilt angle  $\theta$  has to be lowered to an acceptable  $\pm d_{var}$  value (e.g. for  $\theta = 5^\circ$ , the  $\pm d_{var}$  has shrunk down to  $\pm 0.1\text{ mm}$ , that is less than the uncertainty about the positions of the optical components);

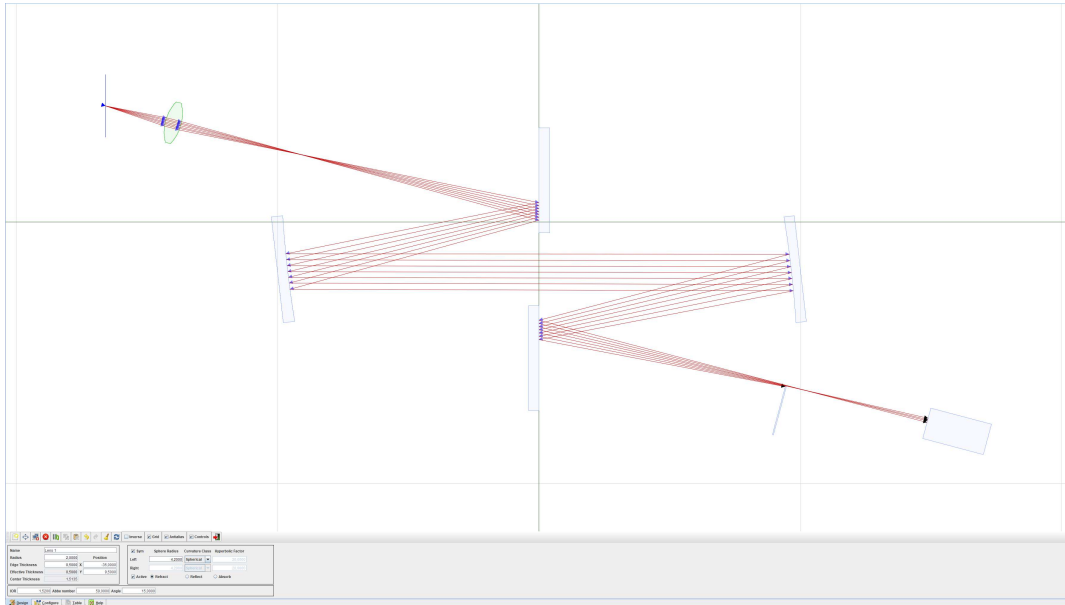
The starting value during the first assembly attempt was higher than  $10^\circ$ , but thanks to the *Matlab® Routine for Geometrical Construction* it shrank down to a satisfying  $\theta = 5^\circ$  value, which is very close to the  $3^\circ$  adopted by Settles [34, p.205] in some of its applications. It is virtually possible to reduce this value even more, by adopting a different mounting support system, but it requires further resources that were not available at the time.

## Optical Tracking Software

The programs for ray-tracking optical evaluation have been useful tools both for studies on other configurations during preliminary phases and for validating the  $\theta = 5^\circ$  value returned by the *Matlab<sup>®</sup> Routine for Geometrical Construction* (see Fig.3.27).



(a) Workflow in *WinLens3D Basic*, basic version of professional software by *Qioptiq<sup>®</sup>* [31].



(b) Workflow in *Optical Ray Tracer<sup>®</sup>*, freeware utility by P. Lutus [19].

Figure 3.27: Preliminary configurations through *commercial basic* (a) and *freeware* (b) software.

They also return the *relative distances* between components for simplified geometrical models, associated to a  $\theta = 5^\circ$  configuration, in order to preliminary size the schlieren system. Then, the definitive distance values are obtained by finalizing the CAD model.

### 3.3.2 CAD Model

The CAD model is more than just a digital reconstruction of the overall system and its parts. It has been a fundamental validation instrument during the *sizing* of the machinery and it is also an active tool for the calibration of the system, as long as it gives back the *relative distances* between the optical components (see Sec.4.1.1 at p.54), which otherwise would be deduced by geometrical construction, that would inevitably lead to much more imprecise results. Indeed, the CAD model works also like an efficient virtual meter, taking advantage from the high fidelity details of its parts, resulting as able to measure distances otherwise impossible to collect (due to their millimetre-scale for optical micro-calibration procedures, or large-scale for macro-calibration procedures between the two opposite sides of the structure).



Figure 3.28: Multiple views from the CAD model of the definitive system configuration.

The CAD model has been fully developed in *CATIA<sup>TM</sup> V5R19* (*Dassault Systèmes<sup>®</sup>*) and is available for the final user, in order to conduct the *advanced calibration* procedures with millimetre-precision (see Sec.4.1.2 at p.61).

A brief *components list* is available in Appendix C.

### 3.3.3 *Matlab® Image Analysis Routine*

This Matlab® routine has been written in a *top-down* perspective, following an *object oriented* programming philosophy, typical of Java® ambient programs. This choice comes from the necessity to keep the *Matlab® Image Analysis Routine* user interface as simple as possible for immediate use but, at the same time, to furnish an easy access to the code to programmers for further corrections. Indeed, it results very easy to reach the single function of interest and to add the required corrections.

The routine provides a complex image analysis on a set of images to the user. These pictures usually are captured during a chemiluminescence and/or schlieren test campaign. It provides many pictures and diagrams of interest, resulting from the data analysis.

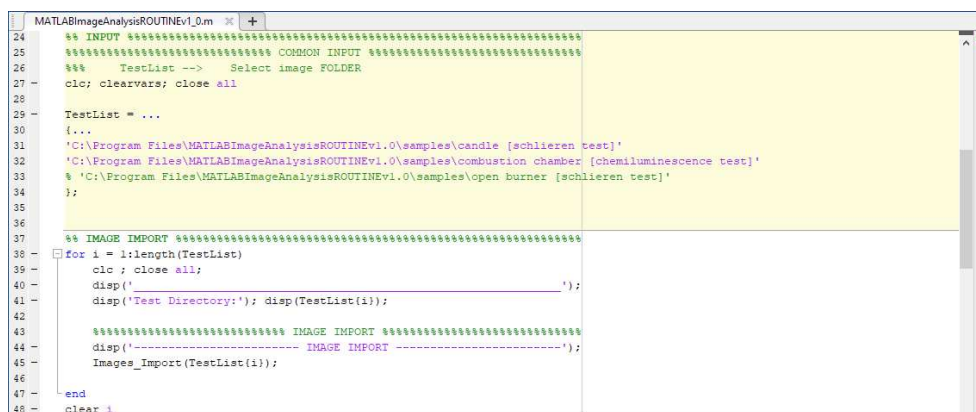
To properly work, the routine needs specific data input, provided by the end user (see *attachments*). All routine results are visible on screen during the routine execution and are stored in the relative test folder. To properly configure the program, it is due to set files "*test\_data*" (for *import*, *processing* and *chemiluminescence analysis*) and "*schlieren\_data*" (for *schlieren analysis*) to fit as close to the experimental configuration as possible. This means to characterize the fluid properties, boundary conditions, setup sizing, etc.

Every function of *Matlab® Image Analysis Routine* has a specific purpose and they are nested in one another, in order to reach a fine level of computational complexity and capability to deal with as much cases as possible. Despite of its more than 3000 lines of code, the routine keeps a relatively simple structure (see Fig.3.30). Indeed, the subroutines are designed to limit the knowledge of the program to the simple input pondering, without necessarily get into the program code itself (if not for specific programming refinement purposes). Further improvements will be always necessary, to fit the data analysis request, so this approach is strongly encouraged. Meanwhile, the necessity for a working program



Figure 3.29: A *Quick User Guide* is within the program folder, available for the end user.

has been accomplished and represents an useful instrument for test engineers who need a quick real-time data comparison during test sessions. It is important to underline how much realistic results are strongly bounded to experimental data coming from sensors during test sessions. Matching these two philosophies is the best way to accomplish a more and more realistic modelling through the Matlab® routine. The *structure tree* of the program is reported in Appendix A.1.

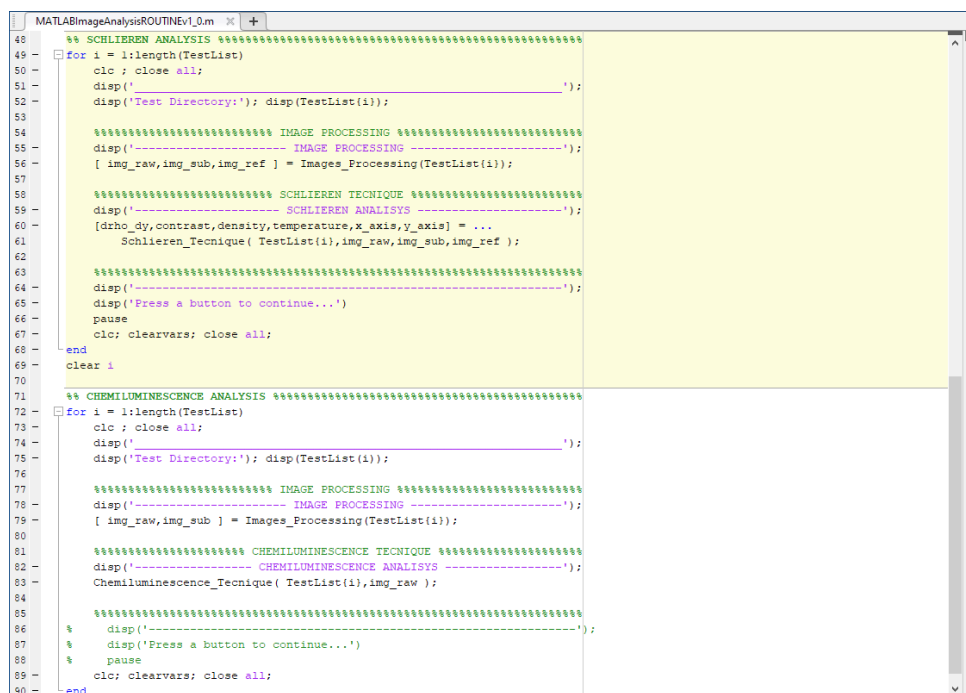


```

MATLABImageAnalysisROUTINEv1_0.m
24  %% INPUT =====
25  %% ===== COMMON INPUT =====
26  %% TestList --> Select image FOLDER
27  clc; clearvars; close all
28
29  TestList = ...
30  { ...
31  'C:\Program Files\MATLABImageAnalysisROUTINEv1.0\samples\candle [schlieren test]'
32  'C:\Program Files\MATLABImageAnalysisROUTINEv1.0\samples\combustion chamber [chemiluminescence test]'
33  'C:\Program Files\MATLABImageAnalysisROUTINEv1.0\samples\open burner [schlieren test]'
34  };
35
36
37  %% IMAGE IMPORT =====
38  for i = 1:length(TestList)
39      clc ; close all;
40      disp(' ');
41      disp('Test Directory:'); disp(TestList{i});
42
43      % ===== IMAGE IMPORT =====
44      disp('----- IMAGE IMPORT -----');
45      Images_Import(TestList{i});
46
47  end
48  clear i

```

(a) *Input and Image Import subroutines interface.*



```

MATLABImageAnalysisROUTINEv1_0.m
49  %% SCHLIEREN ANALYSIS =====
50  for i = 1:length(TestList)
51      clc ; close all;
52      disp(' ');
53      disp('Test Directory:'); disp(TestList{i});
54
55      % ===== IMAGE PROCESSING =====
56      disp('----- IMAGE PROCESSING -----');
57      [ img_raw,img_sub,img_ref ] = Images_Processing(TestList{i});
58
59      % ===== SCHLIEREN TECHNIQUE =====
60      disp('----- SCHLIEREN ANALYSIS -----');
61      [drho_dy,contrast,density,temperature,x_axis,y_axis] = ...
62      Schlieren_Tecnique( TestList{i},img_raw,img_sub,img_ref );
63
64      disp('-----');
65      disp('Press a button to continue...')
66      pause
67      clc; clearvars; close all;
68  end
69  clear i
70
71  %% CHEMILUMINESCENCE ANALYSIS =====
72  for i = 1:length(TestList)
73      clc ; close all;
74      disp(' ');
75      disp('Test Directory:'); disp(TestList{i});
76
77      % ===== IMAGE PROCESSING =====
78      disp('----- IMAGE PROCESSING -----');
79      [ img_raw,img_sub ] = Images_Processing(TestList{i});
80
81      % ===== CHEMILUMINESCENCE TECHNIQUE =====
82      disp('----- CHEMILUMINESCENCE ANALYSIS -----');
83      Chemiluminescence_Tecnique( TestList{i},img_raw );
84
85      % =====
86      disp('-----');
87      disp('Press a button to continue...')
88      pause
89      clc; clearvars; close all;
90  end

```

(b) *Schlieren Analysis and Chemiluminescence Analysis subroutines interface.*

Figure 3.30: User interface of main functions from *Matlab® Image Analysis Routine*.

A *quick user guide* (see Fig.3.29) is available for the end user (see *attachments*). It provides the information necessary for test engineers and data analysts to effectively use the *Matlab® Image Analysis Routine*.

## 3.4 Future Improvements

This section is dedicated to possible improvements that could be brought to the system in the future, in order to improve its functionalities and overall results quality. These solutions have not been implemented at the delivery time because their implementation was not considered of critical relevance to the basic functioning of the machinery, as well as for lack of time and resources. Yet, they deserve consideration as well, hoping for the overall efficiency of the schlieren system to be refined.

### Light Source Block

**Better LED Solution** An updated model is presented, as alternative to the actual solution. It is the high-power green LED lamp *CBT-120* by *Luminus Inc.*, which found many succesful applications in schlieren diagnostics [52][53]. It has a  $2.6 \times 4.6 \text{ mm}$  light emitting surface (LES), a  $520 - 540 \text{ nm}$  wavelength range, and puts out  $800 - 2100 \text{ lm}$  [35]. Assuming to know from datasheet the *CBT-120* characteristics, one could also try to directly use the LED at the focus of the 1ST concave mirror, thus eliminating [34] the condenser and slit, nor allowing to combine the slit with the LED source in close contact upon emitter size and shape (see Sec.3.2.1 at p.31).

**Single-Element Condenser Lens** One could implement a single-element a-spheric condenser lens, in order to reduce the optical aberrations resulting from the actual arrangement. Vasiliev [46] suggests a condenser f/no.  $1 \div 2$  times smaller that the 1ST optical element, moreover the lens should be both spherical and free from chromatic aberrations.

**Sharp Slit Source** In future applications, will be possible to implement a narrowed source slit with a known  $a_s$  value, that will substitute the actual configuration, which couples a *light-amount regulator* and a widened *source slit* (see Fig.3.12 at p.32) and consequently to increase the precision of the numerical evaluations.

### Alternative Calibration Techniques

**Laser Alignment Method** A peculiar technique [29] has been developed in order to maintain the proper alignment between the optical components by using alignment lasers placed on the mirror mounts. The lasers helped to facilitate the alignment procedure.

**Calibration Lens Technique** The approach consists in placing a calibration object (e.g. a long FL lens [33][11], longer than the mirrors FL), with a known refractive-index variation, in the FOV, thus allowing a gray-scale conversion of the refractive-index gradient values. Each radial position in the lens has a different refractive-index gradient, allowing the imaged horizontal gradient across the lens to provide the necessary calibration of pixel intensity to refractive-index-gradient value. Longer lenses provide finer resolution of refractive-index variations.

**Knife-Edge Controller** A servo system was designed to compensate the vibration due to a supersonic flow in a wind tunnel at the *Arnold Engineering Development Center* [48]. The closed-loop servo system captures the vibrations and adjusts the schlieren knife edge accordingly. This solution could be implemented in case that the vibrations resulting from the combustion chamber functioning may excessively affect the quality of the results in future test campaigns.

### Alternative Schlieren Techniques

**Rainbow Schlieren** Produces images with hue variations instead of gray-scale values, by implementing a color-grid cut-off filter in place of a traditional knife-edge filter [28, p.47]. The colors of the rainbow schlieren do not provide more information than the gray-scale version, but rainbow cut-offs have the advantage that they can be designed to color-code specific refraction directions or magnitudes (e.g. bulls-eye pattern to highlight radial refraction variations). Moreover, digital color images inherently provide more information-coding capability than gray-scale. This does not come without disadvantages, though, such as resolution loss due to diffraction by the narrow color cut-off bands and fabrication problems due to color transparency film quality [35].

**Synthetic-Schlieren Techniques** These relatively new optical methods utilise image processing technology to provide a quantitative whole-field density measurements in two-dimensional density-stratified flows [7], by adopting an optical arrangement much simpler to set up than the classical schlieren methods (and do not require high quality optical windows in the experimental apparatus). The biggest disadvantage may be a reduced spatial resolution compared with classic schlieren techniques, but for some application this issue may be negligible as long as the curvature in the density field remains small.

**Laser Schlieren** The laser sources have been excluded from this project, because of their diffraction affection and the serious issue of camera saturation. On the other hand, they could be a valid solution in case that the LED-based arrangement results able to properly exclude the self-luminous phenomena associated to the combustor flame. In that case, a specific laser light source could be implemented, coupled with a narrow "notch" filter at the laser frequency. The filter admits the direct laser light but excludes most of the light incoming from the self-luminous phenomenon [34, p.183].

## Camera Block

**Long FL Camera Lens** A longer FL camera lens (*telescopic lens*) could avoid the implementation of the additional focusing lens on the camera block. In routine schlieren photography, a wider-aperture 35mm prime lens or zoom lens could also be mounted directly to the camera body through a C-mount adaptor.

## Matlab® Image Analysis Routine Improvements

**Gladstone-Dale Constant** The conversion from refractive-index-gradient field to density field via Gladstone-Dale relationship requires an uniform fluid with a known Gladstone-Dale constant  $k$  [35]. The exact estimate<sup>8</sup> of the Gladstone-Dale constant for the mixture GOX/GCH<sub>4</sub> requires in-depth knowledge of  $\rho$ ,  $T$  and  $C$  (*species concentration*) along the combustion chamber, that are far beyond the final purpose of this thesis. By now, the Gladstone-Dale coefficient is assumed constant and corresponding to  $k_0$  from the surrounding medium, taking into account the errors coming from this over-simplification, but in future applications (in particular for MoRaP) could be possible to determine a matrix distribution  $k(x,y)$  on a x,y-plane of mean values along the optical axis depending on  $\rho$ ,  $T$  and  $C$ .

---

<sup>8</sup>The *Lorentz-Lorenz* formula (see Eq.2.1 at p.4) is a special case of a more general dependence of refractive index on *density*, *temperature* and *species concentration*. The general form can be written as a virial expansion in the dependent variables ( $\rho, T, C$ ) [28, p.13]:

$$\frac{(n^2 - 1)}{\rho(n^2 + 2)} = a_0 + a_1\rho + a_2T + a_3C$$

The individual dependence on temperature and concentration is negligible for most of media. The correction to *Lorentz-Lorenz* formula can so reduce to:

$$\frac{(n^2 - 1)}{\rho(n^2 + 2)} = a_0 + a_1\rho$$

which has small effect on gases [28, p.13]. This does not exclude that the effects could be sensitive in case of strong density variations (e.g. flame of a combustor) nor discrete alterations of temperature and species concentrations in the flow-field.

**Specific Gases Constant** A similar issue could affect the specific gas constant  $R$  too, due to its dependence on local species concentration ( $R = \bar{R}/M$ ). Could be necessary, in order to achieve a more realistic solution, to determine a distribution  $R(x,y)$  along the x,y-plane, depending on the average species concentration along the optical axis.

**BCs Optimization** The *Matlab® Image Analysis Routine* is predisposed for non-uniform BCs along the BCs side of the image, such as density, pressure and temperature distributions different from uniform conditions (e.g.  $\rho_0$ ,  $T_0$  and  $p_0$  from the surrounding medium). On the other hand, the routine is not yet *optimized*, due to lack of tested experimental conditions. It is advisable in the future to test and correct the *Matlab®* source code in order to fit the specific requests for the experiment one is conducting. It is also advisable to optimize the code for non-isobaric phenomena (e.g.  $p(x,y) \neq \text{const}$ ).

**Effects of Flow-field Depth** There is a discrete ambiguity on the correct definition of  $L$  (depth of flow-field along the optical path). Sometimes in literature one refers to it as the whole optical path [28, p.28] (from light source to sensor/screen), some other times is the geometrical light path ( $PL$ ) actually covered by light rays [28, p.14] ( $PL = \int_0^L n dz$ , where  $L$  is light path in vacuum), more commonly is just assumed as "test area" length with no further speculation. Because of its pivotal role in this analysis, a unique and rigorous definition is needed. For our purposes, the  $L$  definition has been inherited from Settles, who explained  $L$  role during the analytical derivation of deflection angles  $\varepsilon$  coming from a "*two-dimensional schlieren of extent  $L$  along the optical axis*" [34, p.27].

If  $L$  is meant as the *extension of a schlieren object along the optical axis*, this definition opens to a plethora of possible solutions that try to describe the yet undefined schlieren object. The most intuitive solution could be a constant  $L$  value along the optical path in the region containing the schlieren object and observed by schlieren photography, but any assumption on its real extension is merely speculative. Moreover, assuming a constant  $L$  value could negatively affect the numerical solution in a quantitative evaluation perspective, because of an inevitably misrepresentation of the actual shape of the schlieren object. Further research still need to be carried on by searching a more rigorous definition of  $L$  in literature and, most of all, by confronting experimental results with computational results, obtained from the *Matlab® Image Analysis Routine* by assuming different solutions for the flow-field modelling.

**Optimization for Window** The *Matlab® Image Analysis Routine* is predisposed but not yet optimized for handling the effects of windows presence along the optical path.

## Chapter 4

# Experimental Setup

## 4.1 Calibration Procedures

By following the approach proposed by Settles [34, p.201], this chapter is meant more as a manual to calibration process for the final operator than part of the design process. It is referred to both users that deal with the system calibration for the first time and users that need to adapt an already calibrated machinery to their research purposes. For as secondary as it may seem at first, the calibration procedures represent the summary of all the efforts in obtaining a unique and coherent *step-by-step* procedure that may conduct to an optical system properly calibrated, moreover it provides also some of the most relevant practical application of the concepts introduced in the previous chapters.

### 4.1.1 Basic Calibration

This *step-by-step* procedure explains in details how to properly set every components for a basic configuration and draws the guidelines for sustaining any future specific test campaign. It is not a necessary procedure in case the setup has previously been calibrated, but is always an useful reading for check-up purposes.

#### 1. Light Source Block

- **Step 1:** Mount the light source block close to the edge of the mounting bracket as a temporary solution (will be fixed later);
- **Step 2:** Choose a common *height* and set all pieces to this value. This one is not conditioned by your test object of study, but should be suitable for the light source block size;

- **Step 3:** Set all pieces parallel to each other and orthogonal to the breadboard plate short side;
- **Step 4:** Check the *levelling* of the breadboard plate using a professional level and make sure that it is null (necessary step to obtain a proper parallel beam). In case it is different from zero, help yourself tightening the M6 screws that set the breadboard plate height from the rotating support;

## 2. 1ST Concave Mirror

- **Step 1:** Make sure that both regulation angles on concave mirror support result as *null* (it is advisable to make use of a professional calibre);
- **Step 2:** Mount the concave mirror block as close as possible to the clamping carrier at the mounting bracket root (*this is an optional step, in principle this procedure is valid for any 1ST Concave Mirror disposition along the longitudinal direction; in case you are already dealing with the object of study, placed in the test session, it is strongly recommended to align the optical axis with the section of interest in this instance*);
- **Step 3:** Fix the concave mirror to a *basic null angle* (this will be fixed later), orthogonal to the mounting bracket;
- **Step 4:** Set the concave mirror *height* to a value that matches the concave mirror centre to the other components centres;
- **Step 5:** Verify that the light beam centre fits the concave mirror centre from the previous random angulation (in case you do not find *vertically* this match, go back to **Light Source Block - Step 4**);
- **(N.B.) 1ST Concave Mirror Alignment:** as anticipated in **Step 2**, *in case you are already dealing with your object of study*, it is strongly recommended to already align the optical axis with the section of interest. It is possible to achieve that by recalling the optical path behaviour. It will result orthogonal to the longitudinal direction, along which you can slide the 1ST Concave Mirror support. In particular it will be possible to regulate the whole optical system height by reducing or increasing the height from both (left/right) mounting brackets. Once the alignment between optical axis and region of interest and the height regulation on both mounting brackets have been achieved, you can prosecute to the next step;

### 3. Matching Light Source Block & 1ST Concave Mirror

- **Step 1:** Set the concave mirror *tilt angle* to the nominal value  $\theta$  properly chosen before (see Sec.3.3.1 at p.44 or *Off-Axis Aberrations: Coma and Astigmatism* in **Practical Issues**);
- **Step 2:** Match the light source block with the concave mirror, by modifying the *distance of the entire mounting bracket from the flat mirror* and the *distance of the light source block from the fixed concave mirror*. A good starting point is modelling the light path as sides of equal length of an isosceles triangle, of which leg measures exactly half the FL ( $f$ ) of the concave mirror, while half the vertex angle measures  $2\theta$ , in order to *match a perfect alignment* is strongly suggested to use the MATLAB<sup>®</sup> routine "*Geometrical\_Costruction.m*" (see Sec.3.3.1 at p.44 or relative *attachments*);
- **Step 3:** Change the light source block *tilt angle* until the light beam fits perfectly the concave mirror shape (by temporary substituting the concave mirror with a white piece of paper with a small cross in the centre can come in handy). If *mounting bracket distance from the flat mirror* and *relative distance between light source block and concave mirror components* have been properly set, the just obtained light source block tilt angle should result as the double of the concave mirror tilt angle ( $2\theta$ ). This match will provide a straight and cylindrical light beam across the test zone;
- **Step 4:** Verify that the light source block tilt angle results actually as  $2\theta$  (you could use a simple protractor). In case that you find a strong dissimilarity from the expected tilt angle value, please take note of this and go on with next calibration steps. This issue will be compensated later by fixing the concave mirror angle (see also *Improper Alignments* in **Practical Issues**);

### 4. Light Beam along Test Section

The best way to verify that calibration is going well is to use a blank paper sheet, drawing a circle that matches the concave mirrors diameter, and check that the light beam impressed on it keeps a circular shape that fits closely the figure just drawn (Vasiliev [46] says  $\pm 3$  mm is an acceptable tolerance on the first FL setting). This tool results to be very useful and is advisable to keep adopting it afterwards in different occasions.

## 5. CAD Model

In order to obtain a proper match between components, a detailed *CAD model* has been furnished to the operator as a calibration tool. Follow the next steps for properly set the CAD model (see Sec.3.3.2 at p.47):

- **Left Block setup:** This block comprehends *Light Source Block*, *1ST Concave Mirror* and relative mounting bracket. Edit the *distance of left mounting bracket from the main setup base* to a value that could fit your object of study (standard value on 700mm), then update all setup inputs (*distances* and *tilt angle*) to the settings you choose to work with (standard values for  $\theta = 5^\circ$  and associated distances);
- **Right Block setup:** This block comprehends *2ND Concave Mirror*, *Camera Block* and relative mounting bracket. Edit the *distance of right mounting bracket from the main setup base* to a value that could fit your object of study (standard value on 100mm), then no further modify is actually required;
- **Distance Value for a Proper Alignment:** This CAD model will automatically furnish you the exact value for the two concave mirrors match in occurrence of a straight cylindrical light beam. You can read this value as *distance between 2ND concave mirror and the right mounting bracket root*. Keep note of this value (will be used in next section);
- **(N.B.) Not Updated Settings:** It is important to notice that the *camera block distance from 2ND concave mirror* and *distance between right mounting bracket and flat mirror* have not yet been modified (standard values for  $\theta = 5^\circ$  and associated distances). In order to update this CAD model, follow the steps from the next section and enter the CAD model using the proper values evaluated for an eventual new value of  $\theta$  (standard values for  $\theta = 5^\circ$  and associated distances);

## 6. 2ND Concave Mirror

- **Step 1:** Make sure that both regulation angles on concave mirror support result as *null* (it is advisable to make use of a professional calibre);
- **Step 2:** Mount the concave mirror block at the previously estimated distance from the mounting bracket root (see **CAD Model - Distance Value for a Proper Alignment**);
- **Step 3:** Fix the concave mirror to a *basic null angle* (this will be fixed later), orthogonal to the mounting bracket;

- **Step 4:** Set the 2ND concave mirror *height* to a value that plausibly matches both concave mirrors heights (as before, substituting the concave mirror with a white piece of paper with a small cross in the centre can come in handy). It is possible to follow this step by confronting measures on the setup itself, or by consulting the coupling measures on the CAD model (more advisable solution). After this step, if it is not possible to immediately align the 2ND concave mirror with the light beam centre, due to small degrees mismatch on the 1ST concave mirror block, go back to **Light Source Block - Step 4** and **1ST Concave Mirror - Step 1** (check also *Improper Alignments* in **Practical Issues** for details). In order to obtain a straight and cylindrical light beam perfectly fitting the 2ND concave mirror, you have to modify the 1ST concave mirror *vertical* tilt angle from the project value  $0^\circ$  by using the regulation valve. Take note of the increase of the distance induced by the regulator valve if it results as more than  $1\text{ mm}$  (ca.  $2^\circ$  increment). Notice that it is possible in this occurrence that you can not manage to find a proper *horizontal alignment* (see **Matching Light Source Block & 1ST Concave Mirror - Step 4**). In this case, temporary move the 2ND concave mirror block to an aligned position for height regulation, then pull it back to the previous location and proceed to the next step;
- **Step 5:** Verify that the light beam fits *horizontally* the 2ND Concave Mirror centre. It is very plausible that you will not find immediately a proper alignment, due to small degrees mismatch on the 1ST concave mirror block (see **Matching Light Source Block & 1ST Concave Mirror - Step 4** and *Improper Alignments* in **Practical Issues**). In order to obtain a straight and cylindrical light beam perfectly fitting the 2ND concave mirror, you have to modify the 1ST concave mirror tilt angle from the project value  $\theta$ . Take note of the gap between nominal  $\theta$  value and effective tilt angle on 1ST concave mirror  $\theta_L$ . If it results as more than  $1^\circ$  gap, could be reasonable to go back to **1ST Concave Mirror - Step 2** or to **Matching Light Source Block & 1ST Concave Mirror - Step 3**, in order to obtain a better alignment, or to verify that on **CAD Model** every input has been correctly modified. If a proper alignment is not yet obtained, even after these check-up steps, take note of this issue and keep following the calibration procedure;
- **Step 6:** Set the 2ND concave mirror *tilt angle* to the nominal value  $\theta$ ;

## 7. Camera Block

- **Step 1:** Mount the camera block close to the edge of the mounting bracket as a temporary solution (will be fixed later);
- **Step 2:** Set all pieces to a *height* value which matches the 2ND Concave Mirror centre with the camera block components centres. This value is not conditioned by your test object of study;
- **Step 3:** Set all pieces to an angle close to  $2\theta$  value respectively to each other and to the breadboard plate short side (will be better fixed later);

## 8. Matching 2ND Concave Mirror & Camera Block

- **Step 1:** Match the camera block with the 2ND concave mirror, by modifying the *distance of the entire mounting bracket from the flat mirror* and the *distance of the camera block from the fixed concave mirror*. A good starting point is modelling the light path as sides of equal length of an isosceles triangle, of which leg measures exactly half the FL ( $f$ ) of the concave mirror, while half the vertex angle measures  $2\theta$ . In order to *match a perfect alignment* is strongly suggested to use the *MATLAB*<sup>®</sup> routine "*Geometrical\_Costruction.m*" (see Sec.3.3.1 at p.44 or relative *attachments*);
- **Step 2:** Slide the knife-edge filter as aligned as possible with the central point depth of the 2ND concave mirror (will be fixed later during knife-edge filter calibration), then close entirely the knife-edge filter blades in order to let no light pass through and visualize where does the light beam actually impacts on;
- **Step 3:** Verify that the light beam impresses the closed knife-edge filter close to the filter centre, as a *dot*. If you can not manage to find a sharp focus point, it may be that this configuration suffers off-axis aberrations (see *Off-Axis Aberrations: Coma and Astigmatism* in **Practical Issues**). In this case, we will solve these issues in the next section (see *Knife-Edge Filter Calibration*), so take note of the problem and go on with this procedure. If the *horizontal* alignment does not occur (which can be very plausible, due to the amount of possible mismatches along the alignment line), do not move the knife-edge filter. Otherwise, you have to modify the 2ND concave mirror tilt angle from the project value  $\theta$ . Take note of the gap between nominal  $\theta$  value and effective tilt angle on 2ND concave mirror  $\theta_R$ . If it results as more than a  $\theta/2$  gap, could be reasonable to go back to **2ND Concave Mirror - Step 6** in order to obtain

a better angle reading, or to verify that in the **CAD Model** every input has been correctly modified. If a proper alignment is not yet obtained, even after these check-up steps, take note of this issue and keep following the calibration procedure. Differently, if the *vertical* alignment does not occur (which is still very plausible, due to the amount of possible mismatches along the alignment line), you have to alterate the 2ND concave mirror *vertical* tilt angle from the project value  $0^\circ$  by using the regulation valve. Take note of the increase of the distance induced by the regulator valve if it results as more than  $1\text{ mm}$  (ca.  $2^\circ$  increment);

The *basic calibration* section has expired its task. From here on, any further calibration procedure will be specific for the experiment one is conducting. An example of calibrated arrangement is showed in Fig.4.1.

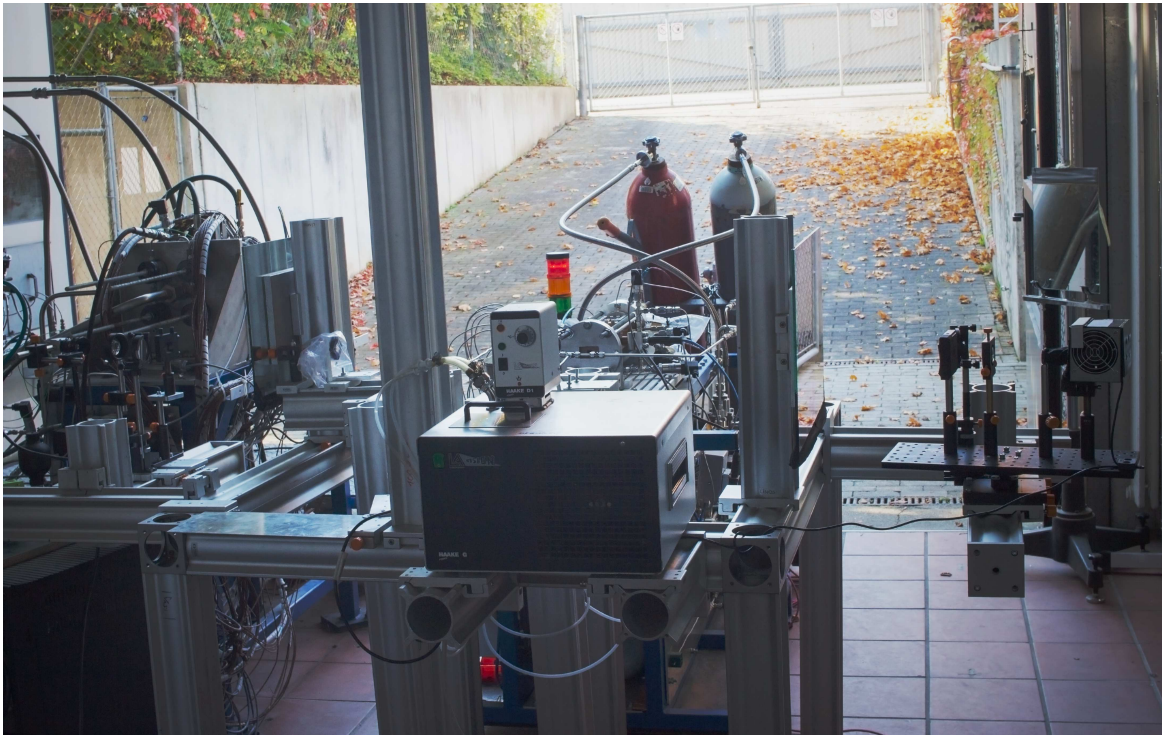


Figure 4.1: Schlieren system just after the *basic calibration* procedure, photo by the author.

In order to proceed with the calibration of the schlieren optical system, you can step to the *advanced calibration* procedure (see Sec.4.1.2 at p.61).

## 4.1.2 Advanced Calibration

This *step-by-step* procedure explains in detail how to properly set every component in a specific configuration of interest during a test campaign. It is a necessary procedure if the setup has not been previously calibrated. Instead, if you are running a test in an already set configuration, it is always an useful reading for check-up purposes.

### 1. Optical Axis Alignment along Test Session

This is a necessary step in case you did not take into account the optical alignment with your object of interest, now placed in the test region. This is also the case if you have lost your alignment from the last test session. Otherwise, if the optical alignment satisfies the test requirements, you can skip this procedure and keep following the **Advanced Calibration** without any further alteration to the setup, but for the knife-edge filter and camera.

- **Left Block setup:** This block comprehends *Light Source Block*, *1ST Concave Mirror* and relative mounting bracket. Go back to **1ST Concave Mirror** step (in **Basic Calibration**, previous section) and update the distance of the 1ST Concave Mirror from the clamping carrier at the mounting bracket root (see (1) in Fig.4.2) and the whole mounting bracket height (see (2) in Fig.4.2) in order to achieve a proper optical axis alignment with the object of study. Then, follow the whole drop-down procedures to basic calibration for *1ST Concave Mirror* and relative mounting bracket, *with the exception of regulating the height of the mirror support or the single optical elements on the breadboard (should be already aligned, but a quick check-up is always recommended)*;

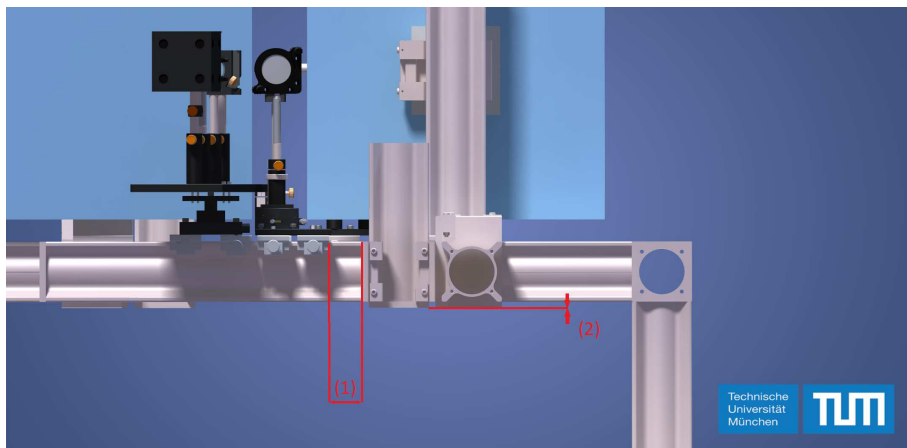
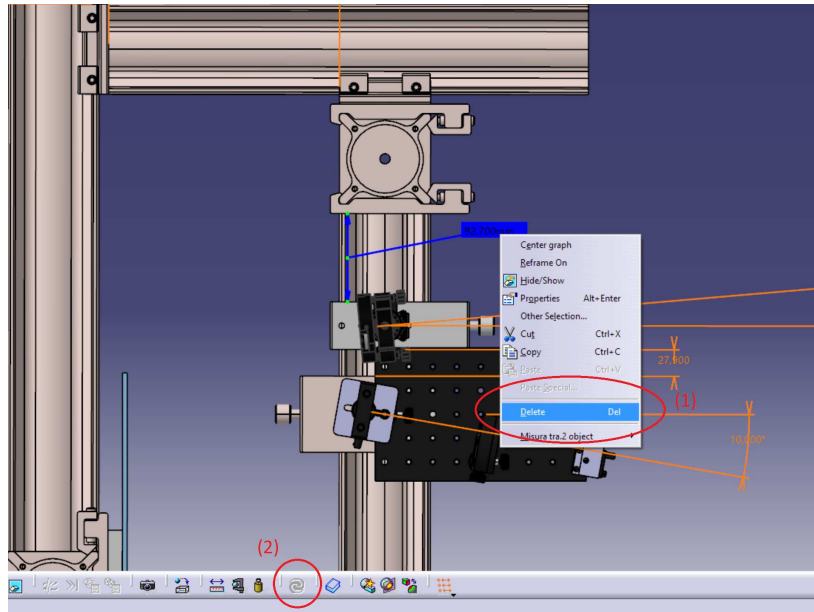
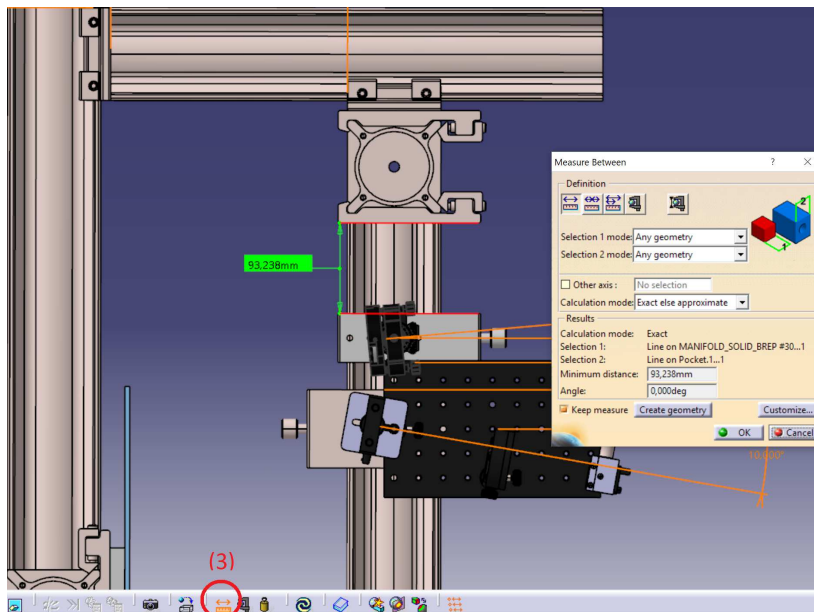


Figure 4.2: *Distance of the 1ST Concave Mirror from the clamping carrier (1) and mounting bracket height (2).*

- **CAD Model:** Go back to **CAD Model** (in section **Basic Calibration**) and update the distance of the 1ST Concave Mirror from the clamping carrier, adopting the value from **Left Block setup** (in **Optical Axis Alignment along Test Session**). Then update (see Fig.4.3a), read (see Fig.4.3b) and note the new distance for the proper alignment on the second block (see **Distance Value for a Proper Alignment from CAD Model in Basic Calibration**);



(a) Delete the previous distance (1) and Update the CAD (2).



(b) Create a new "Measure Between" (3) with the updated CAD.

Figure 4.3: Updating the *alignment distance* for right block on CAD Model.

- **Right Block setup:** This block comprehends *2ND Concave Mirror*, *Camera Block* and relative mounting bracket. Go back to **2ND Concave Mirror** step (in **Basic Calibration**, previous section) and update, with the measure you took note from the **CAD Model**, the distance from the 2ND Concave Mirror to the clamping carrier at the mounting bracket root (see (1) in Fig.4.4) and the whole mounting bracket height (see (2) in Fig.4.4) in order to align the components accordingly to the optical axis. Then, follow the whole drop-down procedures to basic calibration for *2ND Concave Mirror*, *Camera Block* and relative mounting bracket, *with the exception of regulating the height of the mirror support or the single optical elements on the breadboard (should be already aligned, but a quick check-up is always recommended)*;

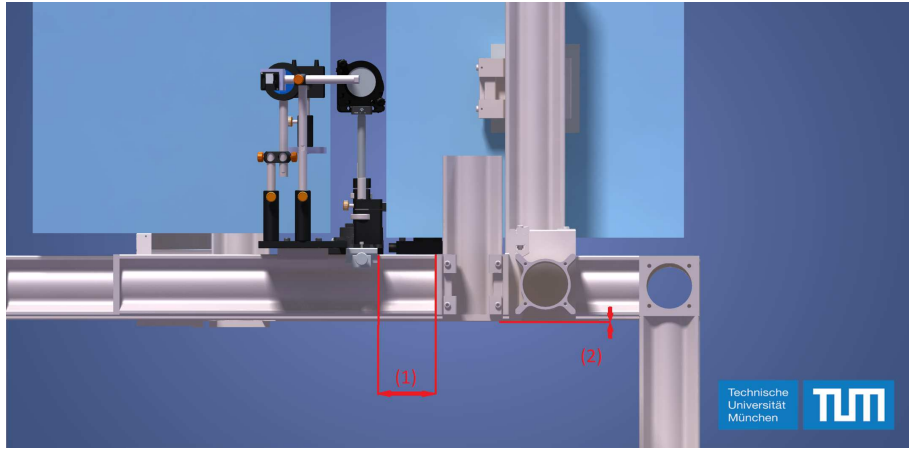


Figure 4.4: Distance of the 2ND Concave Mirror from the clamping carrier (1) and mounting bracket height (2).

## 2. Knife-Edge Filter Calibration

- **Step 1:** Place a white paper sheet behind the closed knife-edge filter at a proper distance to visualize brightness variations;
- **Step 2:** Slightly open the knife-edge filter windows in order to obtain the correct refractive index gradient measurements. In particular, use a vertical knife-edge displacement for horizontal refractive index gradient evaluation, and vice versa. Any cut-off solution that attempts to mask the light beam in perpendicular directions in a single  $x,y$ -plane at the same time is discouraged, because of astigmatic affection of the optical system, which implies that *sagittal* and *tangential foci* result spaced apart by a small distance  $\Delta f$  along the optical axis (see *Off-Axis Aberrations: Coma and Astigmatism* in **Practical Issues**);

- **Step 3:** Verify that, by variation of cut-off amount, the brightness changes homogeneously on the paper sheet. If this is not the case (very common during knife-edge calibration, see *Knife-Edge Filter Calibration* in **Practical Issues**) it is necessary to slide the knife-edge filter along the specific support, until the correct dependency of brightness from cut-off amount is reached;
- **Step 4:** Verify that the knife-edge position just found is in a  $40\text{ mm}$  sliding range ( $\pm 40\text{ mm}$  from the design distance). If this is not the case, you can choose between changing the 2ND Concave Mirror tilt angle and then repeating the Concave Mirror and Camera Block matching (see **Matching 2ND Concave Mirror & Camera Block**), or moving forward (or backward) the single knife-edge support column along the optical axis and then mounting it in a proper location on the breadboard plate. This second solution is more advisable in most of the cases;
- **Step 5:** Set the cut-off amount to 50%, which corresponds to almost half the dot size on the knife-edge blade cut out by the filter (this will be fixed later);

### 3. Camera Calibration & Setting

- **Step 1:** Regulate the *focusing lens*, placed between the knife-edge filter and the camera, in order to focus the light beam on the camera lens. Make sure that the resulting final image on the camera sensor does not exceed the sensor size itself, or the picture will result over-zoomed;
- **Step 2:** Connect the CMOS camera to a terminal by the supplied USB 3.0 cable, then open a visualizer utility from the many programs compatible with the camera model. On the program first start, you may need to modify the image *exposure time* down to  $50\mu\text{s}$  in order to have a decent exposure for calibration;
- **Step 3:** Regulate the camera to *infinity focus* (see *Camera Regulation* in **Practical Issues**);
- **Step 4:** Slide the camera horizontal rod, tilt the support around the vertical rod and rotate the camera around the horizontal rod until you will finally reach a well centred and zoomed image from the visualizer utility output. This procedure will be referred to as *image centring procedure*. It has to be carried out after any further alteration to the setup;
- **Step 5:** Slide gently the camera along the optical axis (in order to reach the minimum focus distance and to include the test zone into the DOF), until you

reach a decent sharpness for the object of study placed in the test zone. Carry out a new *image centring procedure* (see **Step 4**) in order to achieve a correct image output;

- **Step 6:** Close the camera lens blades to highest f/no. as possible ( $f/6$  or  $f/8$  are good values for exposure purposes) in order to correctly regulate the *exposure level* (see *Camera Regulation* in **Practical Issues**). Be aware that an higher f/no. makes further centring procedures harder. Then, carry out a last *image centring procedure*;
- **Step 7:** Set the cut-off amount to the value required for the specific case of study and regulate the exposure accordingly. These steps will surely lead to a satisfactory image quality. High cut-off amounts are suggested in order to increase sensitivity, but it is strongly recommended not to exceed a 90% value, in order to avoid any *diffraction* phenomena at the knife-edge (see *Diffraction* in **Practical Issues**);

## 4.2 Practical Issues

By following the approach proposed by Settles [34, p.165], this section is meant as a panoramic view of most of the practical issues that may occur during a calibration procedure. It delivers also practical solutions to the problematic that may occur during calibration and utilization of the optical system.

### Off-Axis Aberrations: Coma and Astigmatism

The most common optical aberrations resulting from an incorrect alignment between geometrical and optical axes are *coma* and *astigmatism* (see Sec.3.2.1 at p.36). In order to avoid coma and reduce astigmatism, concave mirrors with long f/no. and set with close tilt angle have been adopted.

*Coma* occurs when the direction of light reflected from a mirror depends on the position of the point of reflection. This is a consequence of tilting the schlieren field mirrors off their optical axes. This aberration grows in proportion to tilt angle  $\theta$  and to inverse square of the mirror f/no. for a given  $\theta$ . In result, beginning with a point light source, a *comatic* optical system spreads the point focus into a line [34, p.45]. Fortunately, since

coma is generated at both schlieren field mirrors, it is possible to cancel its overall effect by tilting the mirrors at equal angles  $\theta$ , in opposite directions from the central optical axis, forming a "Z". This Z-type configuration has been adopted, but to be truly effective all optical elements must be centred in a common plane and perfectly aligned. In some cases, it is still possible to verify comatic aberrations due to optical mismatch during setup.

Unlike coma, *astigmatism* cannot be totally eliminated from a Z-type schlieren system or any off-axis mirror system. It is literally the failure to focus a point to a point. Due to finite off-axis angles  $\theta$ , a point light source is imaged as two short lines at right angles to one another and spaced apart a small distance  $\Delta f$  along the optical axis. When astigmatism occurs, the *sagittal plane* (horizontal evaluations) comes into focus at the *sagittal focus* (vertical line), resulting as an elliptical image with respect to the vertical axis. The same is true for the tangential plane. The *tangential plane* (vertical evaluations) comes into focus at the *tangential focus* (horizontal line) which is an elliptical image with respect to the horizontal axis. The sagittal and tangential planes come into focus at two different locations along the optical axis (respectively sagittal and tangential foci), spaced apart a small distance  $\Delta f$  along the optical axis. The point in between where the image is circular is known as the *point of least confusion* [29, p.2], which has not to be confused with the focal point of the 2ND mirror.

The alignment techniques are aimed at reducing coma and astigmatism rapidly. Even though  $\theta$  is minimized and large-f/no. mirrors have been used, some astigmatism will always be present. Astigmatism in Z-type schlieren equipment generally frustrates the use of circular or L-shaped cut-offs, or any cut-off that attempts to mask at the same time the light beam in perpendicular directions in a single x,y-plane [34, p.45].

### Improper Alignments

It is very common to experience improper alignments between components in many occasions. It is not a purely aesthetic matter, because of the final pictures shape that does not properly result as circular, but this also affects the measurements conducted by *Matlab® Image Analysis Routine* itself. So, it is strongly advisable to resolve these issues by adopting a troubleshooting approach and by paying attention to details.

The most common case that can occur on horizontal angles mismatches is during *1ST concave mirror & 2ND concave mirror alignment* (see **2ND Concave Mirror - Step 5**). It is intuitive to verify that even a  $0.5^\circ$  slip (which is a very plausible value) at the 1ST concave mirror alignment can result in more than a 10 mm gap at the 2ND concave mirror

a 1000 mm test section. A mismatch on light source block has conceivably the same effect (see **Matching Light Source Block & 1ST Concave Mirror**).

This issue is usually fixed by modifying the 1ST concave mirror tilt angle from its nominal value  $\theta$ . The effective 1ST concave mirror tilt angle value can be labelled  $\theta_L$ . If the gap between  $\theta$  and  $\theta_L$  results in more than  $1^\circ$ , could be reasonable to go back to previous steps in order to obtain a better alignment, or to verify that the CAD model has been properly set (all specific steps are well explained in calibration procedures). Once check-up steps have been taken into account, if a proper alignment is not yet obtained, one has to take note of this issue and keep following the calibration procedure.

Another common occasion where this issue can verify is during *camera block & 2ND concave mirror alignment* (see **Matching 2ND Concave Mirror & Camera Block - Step 3**) but, differently from the previous case (*1ST concave mirror & 2ND concave mirror alignment*), this should not affect the straightness and cylindrical shape of the light beam in the test zone. This means that, even if going back to check-up steps seems unsuccessful, one can modify  $\theta_R$  up to a reasonable limit value ( $\theta/2$  for instance).

Last but not least case of improper alignments is on the vertical angles, very common during *1ST concave mirror & 2ND concave mirror alignment* (see **2ND Concave Mirror - Step 4**) due to a wrong resulting laying plane for the light beam. As for the previous case, even a  $0.5^\circ$  slip (which is a very plausible value) at the 1ST concave mirror alignment can result in more than a 10 mm gap at the 2ND concave mirror on a 1000 mm test section. This issue is usually fixed by modifying the 1ST concave mirror *vertical* tilt angle from its nominal value  $0^\circ$  by using the regulation valve. The effective 1ST concave mirror tilt angle value can be estimated from the increase of the distance induced by the regulator valve. If it results as more than 1 mm (ca.  $2^\circ$  increment) would be reasonable to go back to previous steps in order to obtain a better alignment, or to verify that the CAD model has been properly set (all specific steps are well explained in calibration procedures). Once check-up steps have been taken into account, if a proper alignment is not yet obtained, one has to take note of this issue and keep following the calibration procedure.

Another common occasion where this issue can verify is during *camera block & 2ND concave mirror alignment* (see **Matching 2ND Concave Mirror & Camera Block - Step 3**) but, differently from the previous case (*1ST concave mirror & 2ND concave mirror alignment*), this should not affect the straightness and cylindrical shape of the light beam in the test zone. This means that, even if going back to check-up steps seems unsuccessful, one can modify the increase of the distance induced by the regulator valve up to a reasonable limit value (2 mm for instance, ca.  $5^\circ$  increment).

### Knife-Edge Filter Calibration

After placing your white-paper screen beyond the filter and placing the knife-edge in order to cut off part of the source image, it will quite surely happen that the screen spot darkens non-uniformly from one side. Take note of which side it is. If it is the same side as the knife-edge, increase the axial distance of the knife-edge from the second mirror and try again. If it is opposite to the knife-edge, decrease the axial distance [34, p.181]. The knife-edge position is correct when the screen darkens uniformly, as shown in Fig.4.5b.

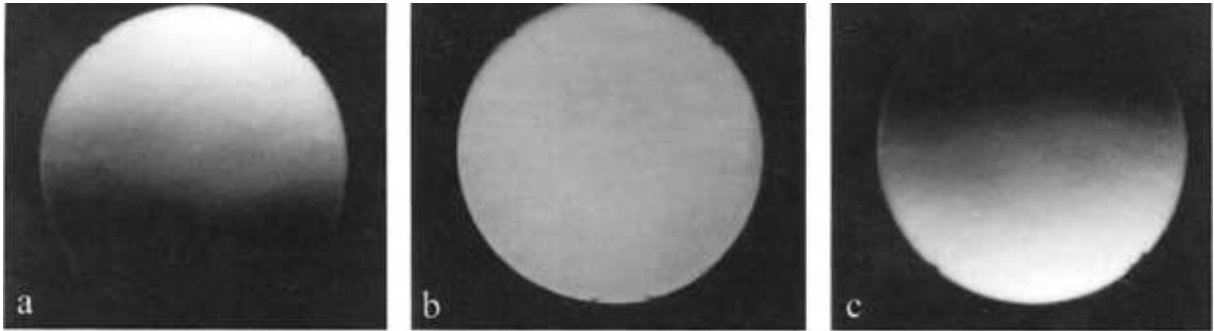


Figure 4.5: Effect on the schlieren image of knife-edge displacement along the optical axis for a horizontal knife-edge entering the beam from below. **a** knife-edge too close to mirror, **b** correct adjustment, **c** knife-edge too far from mirror [34, p.181].

One has to remember that the knife-edge position along the optical axis for uniform cut-off depends on edge orientation (i.e. vertical or horizontal) when *astigmatism* is present (separation  $\Delta f$  between *sagittal* and *tangential foci*, see *Off-Axis Aberrations: Coma and Astigmatism* in **Practical Issues**).

### Diffraction

Diffraction is now recognized as a fundamental part of the schlieren image-formation process, though indeed it is still a roadblock to high sensitivity and to some quantitative measurements. Two diffraction effects are of chief concern: the *diffraction of light in the test area*, creating halos in the image, and the *diffraction at the knife-edge* of the light-source image, which limits schlieren sensitivity and resolution [34, p.66].

In the first case (*diffraction of light in the test area*), Schardin [32, p.1-32][33, p.303-439] makes it clear that diffraction halos are not a very serious problem. They outline opaque objects with thin white lines, but do not usually otherwise obscure the schlieren image. One has to make sure not to confuse them with other bright bands that can appear (e.g. due to test-model misalignment or laminar boundary layers [37, p.524-544]).

On the contrary, the schlieren sensitivity limit, imposed by *diffraction at the knife-edge*, is a pivotal matter in quantitative analysis. Indeed, diffraction provides a natural limit to attempts to increase sensitivity indefinitely by increasing the knife-edge cut-off [33]. The consequences are not as bad as those of an actual narrow slit with two real knife-edges, since diffracted light from the test area is only blocked on one side by a real knife-edge. Nonetheless, the beam approaching the cut-off contains all the information necessary to create a sharp schlieren image [34, p.68]. The main effect of diffraction at knife-edge is smearing the image resolution and creating a diffraction "shadow" emanating perpendicular to the edges of objects in the test area [33] (see Fig.4.6).

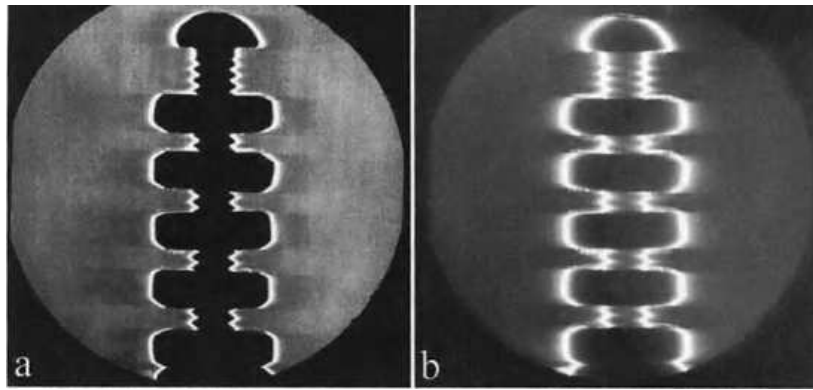


Figure 4.6: (a) 95% cut-off, revealing diffraction "shadows", (b) 100% cut-off reverses the diffraction shadow illumination [34, p.69].

At about 100% knife-edge cut-off, the screen darkens sufficiently that there is an illumination reversal in the phenomenon of diffraction shadowing. In qualitative schlieren, high sensitivity can be obtained before diffraction finally takes over. The consequences are more restrictive for the quantitative evaluation of schlieren images by densitometry at high sensitivity [33][13, p.473-482]. This practice, described in detail by Settles [34, p.263-278], is disrupted when non-uniform image illuminance occurs due to diffraction shadows. *A 90% cut-off amount has resulted from the test sessions as the maximum sensitivity level reachable before a drastic resolution drop.* It is strongly suggested to never exceed this value, as confirmed by Settles [34, p.72], which points the ultimate sensitivity at around 95% cut-off amount.

## Camera Regulation

To achieve a decent image quality is the hardest calibration step, it requires a troubleshooting approach and frequently is source of frustration for a novice. But it becomes easier once that few rudiments about photography and exposure regulation have been acquired.

*Exposure* is the amount of light per unit area that reaches the camera sensor:

$$H_v = I_e \cdot \Delta t \quad (4.1)$$

where  $H_v$  is the *luminous exposure* on a surface ("v" stands for "visual", to avoid confusion with radiometric quantities), it is measured in  $lx \cdot s$  and  $I_e$  and  $\Delta t$  are the *illuminance* (see Sec.2.2.1 at p.9) and the *exposure time*, respectively. The "correct" exposure is the one that achieves the effect the photographer intended. It should represent the best compromise between *lens aperture*, *exposure time* (or *shutter speed*) and *gain* (or *ISO level*).

*Lens aperture* regulation is a fundamental step in order to obtain a decent sharpness on different subjects spaced along the optical axis. It is achieved by closing the lens blades (see Fig.4.7) to the highest f/no. practically reachable.

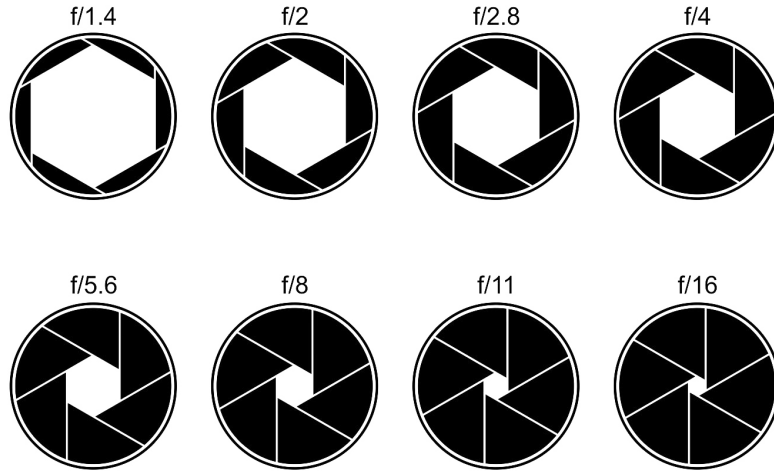


Figure 4.7: Examples of  $f/no.$  for the lens aperture [42].

Higher  $f/no.$  corresponds to wider DOF (sharper image in the test zone) and darker exposure (as clear from Eq.4.1, the exposure depends from the surface<sup>1</sup>). A darker exposure and closer blades can help to cut-off the rays coming from self-luminous phenomena, such as flames. But, a narrow closure of the blades compels also a harder centring procedure of

<sup>1</sup>Exposure level decreases with the square of the  $f/no.$ , as long as a bigger  $f/no.$  means smaller diameter and, consequently, narrower aperture.

the image. This effect has been mitigated by mounting a prime lens with FL longer than 50mm [34, p.74] (in the adopted configuration it is a 55mm FL lens, for compactness purposes), for which *the best solution usually falls in a range of lens aperture values between  $f/6 \div f/8$* .

Regarding lens aperture regulation, we assume the  $f/\text{no.}$  to be the highest reachable for the lens aperture, that means aperture setting is fixed and no longer comes in handy to correct the exposure. Yet, it is possible to manage the exposure level by regulating *exposure time* (or *shutter speed*) and *gain* (or *ISO level*).

*Exposure time* should be short enough to avoid any blur effects on the images (see Fig.4.8). Besides, it is also a fundamental parameter to reduce the incoming light to the camera sensor (by decreasing it), in order to avoid any "burn" regions on the image (white regions which imply *information loss*).

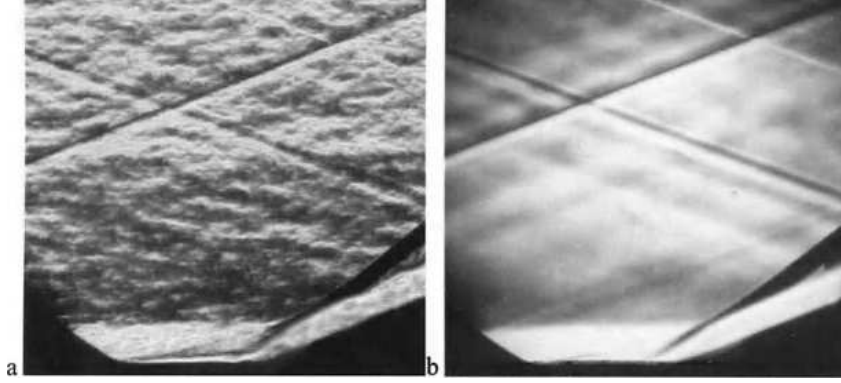


Figure 4.8: Pictures of a shock-wave boundary-layer at Mach 3 [34, p.190]. The turbulence seen in (a) ( $1\mu s$  shutter speed) is mostly optical noise from wind-tunnel side-wall boundary-layers, and is completely averaged out in frame (b) ( $10ms$  shutter speed).

Hyzer [15] asserts that the *exposure time*  $\Delta t$  should minimize the motion blur, concluding that:

$$\Delta t = \frac{\ell_b}{mV \cos \theta} \quad (4.2)$$

where  $\ell_b$  is the blur length,  $m$  is the image magnification,  $V$  is the speed of the observed phenomenon and  $\theta$  is the angle between the image plane and the direction of motion. *For our purposes, we assume a  $30 \div 100\mu s$  shutter-speed range*, in order to achieve the best exposure level.

*Gain* is the sensitivity of the image sensor to light, the lower the number the less sensitive the camera is to light (and the finer the grain). It is an useful instrument, indeed higher numbers mean the sensor becomes more sensitive to light, which allows to collect well exposed images in darker situations, but exceeding with it may lead to unwanted image noise and grain (which deeply affect the image analysis quality). It is a good habit to *keep*

*it to the reachable practical value closest to its starting value 1.00.*

*Exposure time* and *gain* are both needful parameters for exposure regulation in cases of study that involve high cut-off amount at the knife-edge filter, because both can help to restore a correct image exposure level. One has to recall that increasing *exposure time* leads to motion blur, while increasing *gain* leads to image noise and grain. The best solution should always be a good compromise between these two parameters.

Last but not least, the camera lens has to be set to *infinity focus*, in order to achieve the best results for schlieren photography purposes. In optics and photography, infinity focus is the state where a lens or other optical system form an image of an object at infinite distance away. This corresponds to the point of focus for parallel rays (better for schlieren). The image is formed at the focal point of the lens [51], which confirms a  $f/6 \div f/8$  range of lens aperture, if one is looking for a sharp focus on both objects in the test area and parallel rays for schlieren photography. To achieve the infinity focus, one has just to rotate the focus ring all the way to the  $\infty$  symbol, then slightly to rotate it back to  $1^\circ \div 2^\circ$  from the end on the run.

## Chapter 5

# Test Sessions

### 5.1 Test Bench Arrangement

The test campaigns for both the *system calibration* and the *flame study* have been conducted on the same *test bench*, which is here schematized as:

- Schlieren System;
- Flat Flame Burner;
- Feed System;



Figure 5.1: Test bench for the *system calibration* and *flame study* campaigns.

#### 5.1.1 Schlieren Optical System

The *schlieren system* has the same configuration that one could obtain after the *advanced calibration* procedure, which has been widely discussed and requires no further details.

### 5.1.2 Flat Flame McKenna Burner

The open burner adopted for the test campaigns is a *McKenna flat flame burner* (produced by *Holthuis & Associates* [10], in Fig.5.2). It is a porous sintered burner with a plate surface in bronze, 6 cm in diameter. The burner contains a spiral cooling circuit for water flow, in order to minimize radial temperature gradients [4]. The adopted fuel mixture (pre-mixed oxidizer and fuel) is a GOX/GCH<sub>4</sub> mixture, introduced through a 1/4 inch compression fitting into the bottom of the housing (see Appendix B). Further details are reported in Fig.5.3.

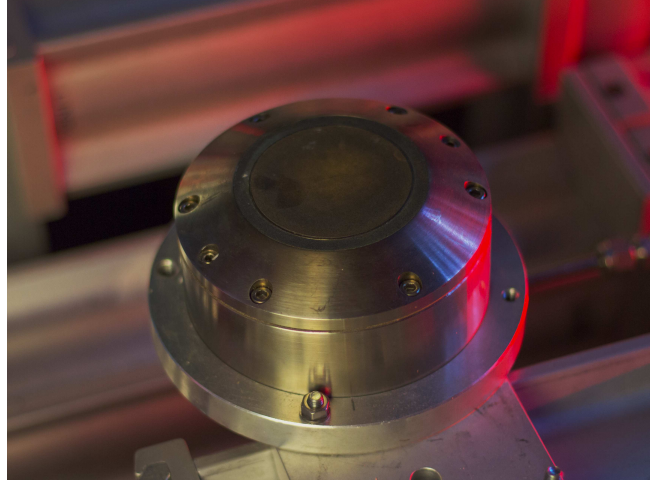
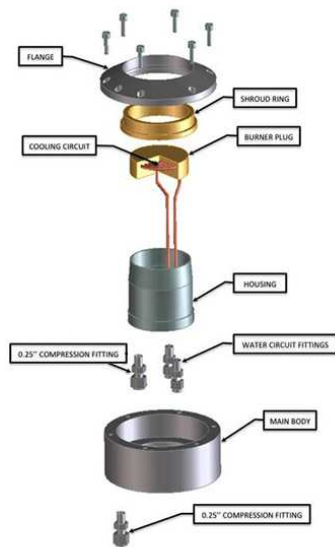


Figure 5.2: *McKenna flat flame standard bronze burner* with standard shroud ring, photo by the author.



Reference: DLR Report: Documentation of Flat Premixed Laminar CH<sub>4</sub>/Air Standard Flames: Temperatures and Species Concentrations, Weigand, Lückerath, Meier

#### Flat Flame Burner

##### • Example flow conditions (DLR)

—Rotometer settings calibrated versus equivalence ratio,  $\phi$

Num ( )	CH <sub>4</sub> (slpm)	Air (slpm)	CH <sub>4</sub>	Air	Phi ( )	T, adiabatic K
			Rotometer Setting (mm)	Rotometer Setting (mm)		
1	1.10	15.00	48	62	0.70	1838
2	1.31	15.60	57	65	0.80	1997
3	1.31	12.40	57	51	1.00	2226
4	1.31	11.31	57	47	1.10	2211
5	1.31	10.40	57	43	1.20	2137
6	1.42	15.00	62	62	0.90	2134
7	1.73	20.63	76	86	0.80	1997
8	1.73	16.50	76	68	1.00	2226
9	1.73	14.96	76	62	1.10	2211
10	1.74	15.00	76	62	1.10	2211

Figure 5.3: *McKenna flat flame burner*, technical specs [10] and example of flow conditions [4] for air/GCH<sub>4</sub> mixture.

This burner is designed for air/GCH<sub>4</sub>, consequently the mass flow rate must be heavily reduced from the standard values (see Fig.5.3), because of the GOX/GCH<sub>4</sub> higher calorific power. As reference temperature, instead, we will consider a near 2000 K, right above the plate (thermocouple placed  $\sim 1$  cm from the surface, near to the hottest point), in

according with the standard values for the air/GCH<sub>4</sub> mixtures (at higher mass flow rate) considered in Fig.5.3. Unfortunately, the data sheet in Fig.5.3 is the only reference chart for comparison about temperature available for our test sessions, which leads to a lower fidelity level on numerical evaluations, but still interesting in terms of qualitative evaluations, comparative quantitative evaluations and in optimization perspective.

### 5.1.3 Feed System and Sequence Definition



Figure 5.4: Example of a *T junction* along the feed lines, photo by the author.

The feed line has been re-arranged from the original feed system of the MoRaP. Two tank of gaseous oxygen and methane are connected to the feed system, while the mass flow rates (GCH<sub>4</sub>, GOX) are set by sonic orifices in the feed lines and the upstream pressure [40]. An external tank of nitrogen is linked too, for purging the feed lines after the functioning, in order to avoid any gases residual. The mass flow rates have been reduced below 1/16 of the original settings for the MoRaP sequence,

due to the original design for the open burner (air/GCH<sub>4</sub> mixture), in order to avoid any thermal damage nor unmanageable flames, always in accordance with LFA security policy. The feed sequence holds for 5 s, during which the flame has to be ignited manually. The *test sequence* has been developed in *LabVIEW*<sup>®</sup> (IDE developed by *National Instruments*<sup>TM</sup>). The *CMOS camera capture sequence* is separated in two phases [14]:

- **Wind-Off procedure:** capturing of the reference image in wind-off conditions (uniform flow-field with no visible phenomenon happening);
- **Wind-On procedure:** capturing of the test sequence in wind-on conditions (functioning of the machinery and flame going on);

The main difficulties during the wind-off procedure (see Fig.5.5a) are obtaining the correct exposure for both the phases (due to incoming rays from self-luminous phenomena, which tend to over-expose the image if not properly excluded) and achieving an uniform flow-field (requires still air, i.e. closed doors in the facility). Once that the wind-off reference image

has been collected, the schlieren system must remain untouched until the experiment is finished, since even the smallest change could irremediably affect the numerical results (the reference image is pivotal for determining the refractive-index variations induced by the schlieren object, in term of contrast).

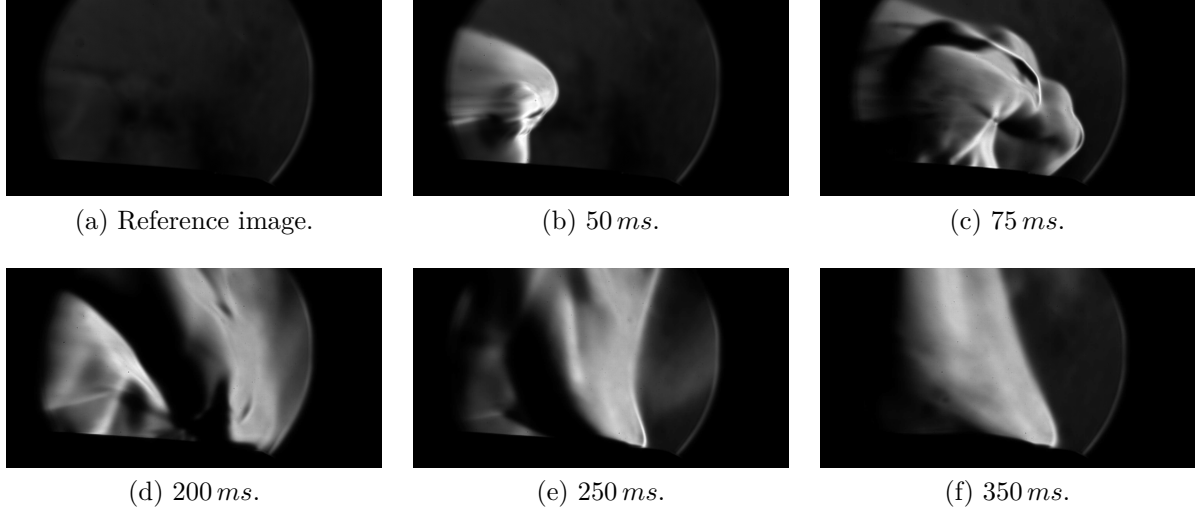


Figure 5.5: Sequence before (a) and after the ignition, showing the blasting and anchoring of the flame at  $O/F = 2.2$ , captured by the author.

The *Matlab*<sup>®</sup> *Image Analysis Routine* sequence has been standardized for all the sequences. It starts 30 frames ( $\sim 0.18 s$ ) after the ignition, when the flame has already anchored (see Fig.5.5f), and goes on for 340 frames ( $\sim 2 s$ ), before that the flame expires and the nitrogen purge starts blowing. This procedure can highlight the actual behaviour of the flame, independently from its casual oscillation in time, by evaluating the *mean values* of brightness and contrast (see Fig.5.6) during the whole 2 s duration of the sequence.

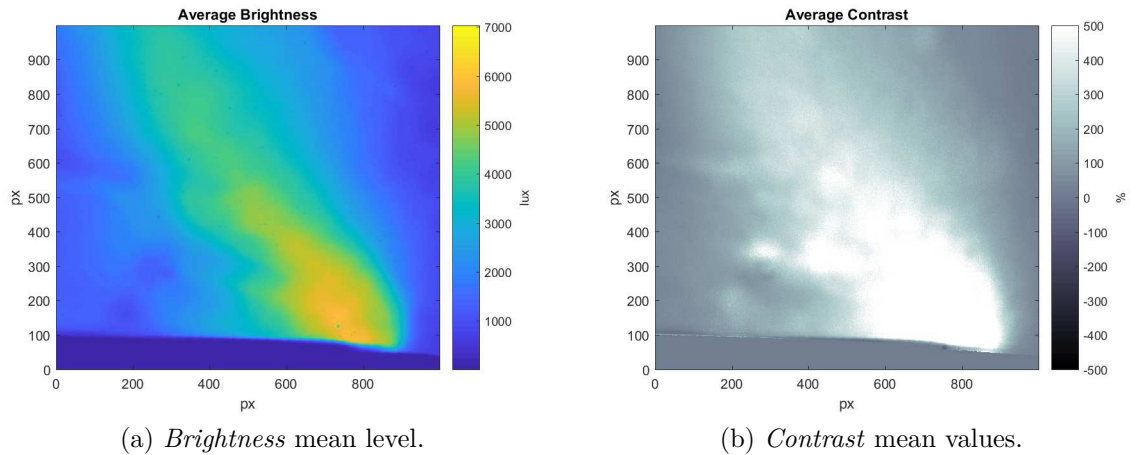


Figure 5.6: Output from *Matlab*<sup>®</sup> *Image Analysis Routine* on the  $O/F = 2.2$  sequence in Fig.5.5.

## 5.2 Test Campaign for System Calibration

This test sessions have the purpose to define the optimal calibration for the schlieren system, in terms of correct exposure and optical sensitivity, and to study the optimal input configuration for the *Matlab® Image Analysis Routine*, in terms of boundary conditions, flow-field discretization and the related limits of validity.

### 5.2.1 Common Inputs

The study starts from the *Matlab® Image Analysis Routine* input solution, as long as it affects all the following results. Some inputs are measurable quantities, while some other are estimated values. The limits of validity of the assumptions are reported in the following sections.

#### Input for Schlieren Technique Routine

The quantities relative to the *surrounding medium* in Tab.5.1 are referred to air in SLS conditions, which is reasonable for an open environment test on the burner. The corresponding Gladstone-Dale constant of the surrounding medium is  $k = (n_0 - 1)/\rho_0$ , referred to air in SLS conditions. The hypothesis assumed for this test sessions is that the Gladstone-Dale coefficient keeps constant its value along the test region, equal to  $k$  for the *surrounding medium*, which is an oversimplification of  $k$  dependence on temperature and gas species concentration. A similar assumption is made for the specific constant of gases  $R$  and its dependence on gas species concentration.

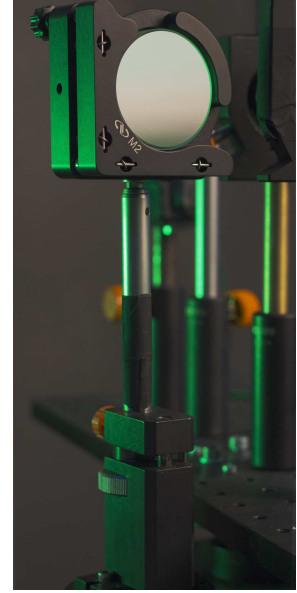


Figure 5.7: 1ST concave mirror arrangement, photo by the author.

Quantity	Symbol	Value	Unit
Density	$\rho_0$	1.225	$kg/m^3$
Temperature	$T_0$	288.18	$K$
Pressure	$p_0$	101325	$Pa$
Specific Gas Constant	$R$	287	$J/Kg \cdot K$
Heat Capacity Ratio	$\gamma$	1.4	$adim$
Refractive Index	$n_0$	1.00027717	$adim$

Table 5.1: *Surrounding medium* properties (referred to air in SLS conditions).

These strong hypotheses tend to affect the realism of numerical evaluations. In-depth knowledge about  $k$  and  $R$  involves additional studies about gas mixture distributions in the volume that are far beyond this thesis purposes. One can assume them as constant and focus on a more comparative numerical evaluation between different cases of study.

Quantity	Symbol	Value	Unit
Concave Mirror Tilt Angle	$\theta$	5	$deg$
Obj. Distance to 2ND Mirror	$D$	893	$m$
Concave Mirror Diameter	$D_1, D_2$	50.8	$mm$
Concave Mirror FL	$f_1, f_2$	500	$mm$
Slit Source	$a_S, a_0$	0.5	$mm$

Table 5.2: *Schlieren setup* properties.

The actual distance  $D$  (see tab.5.2) from the limits of the combustion area to the 2ND concave mirror is bigger than  $f_2$ , which ensures a satisfying image sharpness and focus on the schlieren object. The source slit extension  $a_0$  is approximated ( $\pm 0.1\text{ mm}$  uncertainty, due to diffraction halos and limits in accuracy of measuring instruments). An  $a_0 = 0.5\text{ mm}$  is a common value in literature for schlieren systems based on commercial LED lamps, which leads to  $a_k = 50\text{ }\mu m$  for a reasonable 90 % cut-off amount (better to keep  $a_k$  equal or above this limit value, due to inverse proportionality between sensitivity and measuring range [34, p.61]). Moreover, the precision about  $a_0$  measure could be improved by adopting a narrowed source slit with a diameter matching the requested value ad hoc.

### Solution for Flow-field Domain

The choice of *flow-field model* affects the quality of the numerical solution (see Sec.2.4.1 at p.2.4.1), so that it has been necessary to conduct a series of preliminary tests in order to evaluate and select the best-fitting *flow-field model* (see Appendix A.2) for the case of study.

From Fig.5.8 one can distinguish the transversal portion of the pictures that is examined by the *Matlab® Image Analysis Routine*. It is referred to a  $1000 \times 1000\text{ px}$  portion of the original raw pictures from the schlieren photography, corresponding

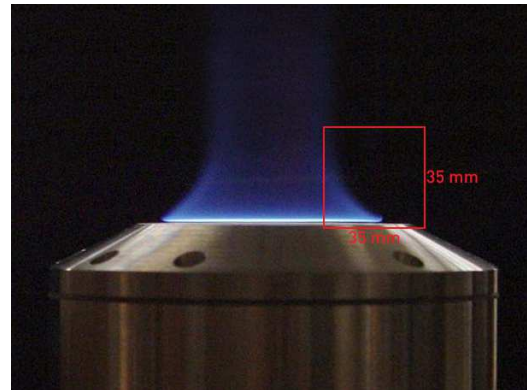


Figure 5.8: Pictures representing the area evaluated by *Matlab® Image Analysis Routine* for a corresponding  $1000 \times 1000\text{ px}$  portion of raw pictures.

to an almost  $35 \times 35 \text{ mm}$  square section. It is a portion of the image almost completely free from optical aberrations, comatic distortions at the mirror contour and out of focus regions, moreover it matches the project request to fit the window dimensions (at least  $4 \text{ cm}$  aperture) for the future model of MoRaP. Indeed, the image size could be eventually extended along the horizontal direction for more than  $500 \text{ px}$ , since a square shape is not a specific need for the analysis through the window on MoRaP.

In Fig.5.9 one can distinguish three specific models for the flow-field discretization. An *All\_Domain* model is the simplest (it keeps  $L$  constant along the optical path) and works well for most of applications (during a preliminary study, the first choice should always be an *All\_Domain* flow-field model).

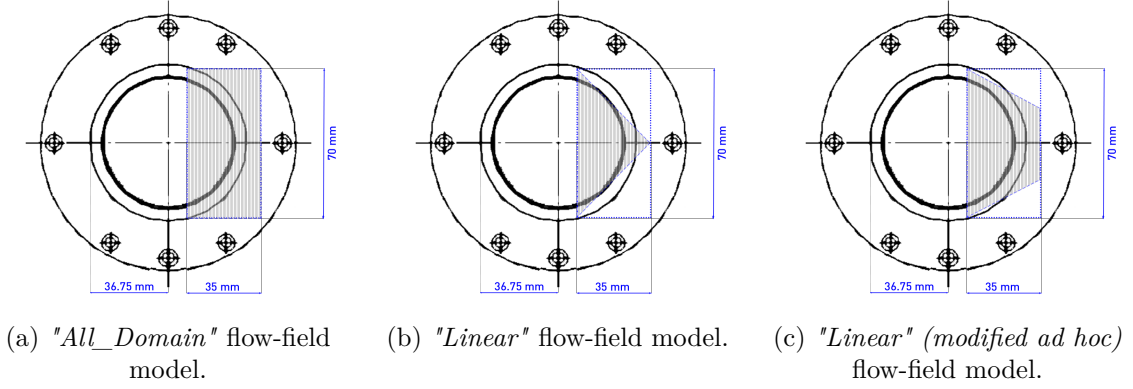


Figure 5.9: Different options for flow-field modelling by *Matlab*<sup>®</sup> *Image Analysis Routine*.

On the other hand, a *"Linear"* model (modified *ad hoc*<sup>1</sup> for the case of study<sup>2</sup>) gives back more realistic values on temperature (if compared with results in Fig.5.3), inducing one to choose this method (see Fig.5.9c) as reference model for the following tests.

The merely estimated evaluation about  $L_{MAX}$  value (longest flow-field depth along the optical axis) and the approximation about its eventual distribution  $L(x,y)$  along the transversal x,y-plane, leads irremediably to a discrete level of uncertainty on the density and temperature distribution achieved by *Matlab*<sup>®</sup> routine. On the other hand, the

<sup>1</sup>The length of the minor base could vary during the test sessions, accordingly to necessity, in order to avoid any numerical errors due to non-convergent solutions, but at the same time with small effects on the overall solution.

<sup>2</sup>The *Matlab*<sup>®</sup> *Image Analysis Routine* flow-field models are not yet optimized. The program version delivered to LFA is meant to work properly with well-isolated phenomena (e.g. *flames in MoRaP combustion chamber* or *candle tests*), in order to fit the future needs for research on MoRaP. For different cases of study, the program needs further optimization.

magnitude of the repercussions in assuming a constant  $L$ , nor a spatial distribution along the transversal plane, has shown to be contained for a well-shaped flow-field. Further research needs to be done on the actual benefits coming from a flow-field modelling that assumes a distribution of  $L(x,y)$  different from a constant  $L$  inside the flow-field domain.

This issue could be inherently solved for the MoRaP combustion chamber, which presents a limited flow-field depth (corresponding to the chamber *inner depth* along the z-axis). This solution could suggest, for future applications on MoRaP, to keep constant the  $L$  value to this specific depth, expecting that all of the heat transfer will happen inside of the chamber, inherently limiting the flow-field extension along the optical axis, by selecting an "*All\_Domain*" flow-field model and specifying the inner depth along the z-axis of the chamber as constant flow-field depth  $L$ .

### Limits of Validity

Most of them have already been introduced in previous sections, as well as in Sec.3.4. Anyway, a brief summary about limits of validity of the numerical results is given below. The limitations about the realism of actual density and temperature numerical evaluations are mostly due to the following factors:

- uncertainty on  $a_0$ ;
- uncertainty on  $L$  distribution;
- uncertainty on *cuf-off amount*;
- assumption of constant value of  $k$ ;
- assumption of constant value of  $R$ ;
- assumption of isobaric phenomenon;

Because of these over-simplified hypotheses, the quantitative evaluation is inevitably affected by errors, which penalize the realism of the solution for density and temperature distributions (and for their gradients along the x,y-plane). To overcome these approximated results, it is necessary to describe the fluid properties into the observable volume by average values along the optical axis, which requires in-depth understanding of the fluid dynamics of the problem, involving different research tools (e.g. TCs and PCs measurements, chemiluminescence diagnostics, CFD modelling, etc.), that goes far beyond the purposes of this thesis.

Despite its (still) flawed numerical results, the system constitutes an useful tool for *comparative quantitative evaluation* (e.g sensitivity to O/F and species concentrations variations) and an extremely powerful diagnostic tool for *qualitative evaluation* (e.g. shape of the flame, fluid dynamic behaviour, boundary layers and recirculation regions detection).

## 5.2.2 Cut-Off Amount Regulation

In most of cases of practical interest, a 90% *cut-off amount* is often adopted. It is virtually possible to extend this value to 95%, but diffraction errors could occur (see Sec.4.2 at p.4.2). Moreover, there would be a trade-off between sensitivity and measuring range<sup>3</sup> [34, p.51], because of the inverse proportionality between these two for a given contrast value.

The purpose of this section is to establish the magnitude of changes in contrast values due to different cut-off amounts and their effects on temperature profile. This analysis takes into account a 75% and a 90% cut-off amount configurations (see Fig.5.10a and Fig.5.10b). The 90% cut-off amount caused a darker exposure level (as one can notice from the background). For this instance, it was not possible to uniform the exposure level between the two configurations, because the *shutter speed* was already at its minimum. Increase the exposure time on the 90% amount configuration could have been a solution, but for this instance we preferred to focus on cut-off effects only. A less rigorous comparative is still possible, but it would presumably lead to very similar conclusions<sup>4</sup>.

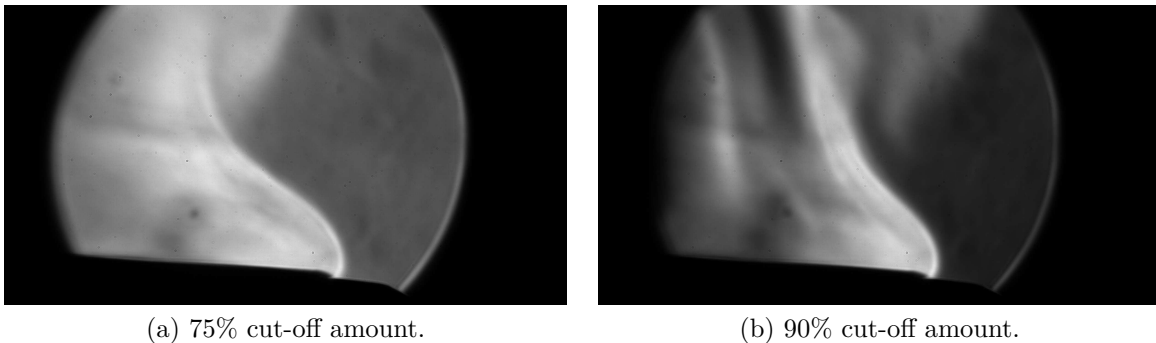


Figure 5.10: Pictures for comparative evaluations between two knife-edge filter configurations with different *cut-off amounts*.

At a glance, the 90% cut-off amount configuration seems to take more advantage of all the grey-scale values available for describing the image, while the 75% cut-off amount configuration presents a less marked contrast in general (see Fig.5.11). This translates in loss of information about the refractive-index gradient and, consequently, the inability for a lower cut-off amount configuration to return a satisfying temperature profile reconstruction. In order to verify this assumption, the *average temperature distribution along x-axis* has been evaluated (see Fig.5.12). This kind of diagrams is obtained from mean values of

<sup>3</sup>Discrete portions of deflected beams could be excluded due to high cut-off amount.

<sup>4</sup>The choice to do not uniform the exposures does not heavily compromise the validity of results, as long as contrast values are referred from wind-off images that present the same exposure levels of wind-on images, for 75% and 90% cut-off amount configurations respectively.

temperature along y-axis for a specific x-coordinate, it results very useful and intuitive in most of comparative evaluations. The maximum value of *average temperature along x-axis* takes into account also the reference temperature of the flow-field, that we investigate in a region located at  $\sim 1\text{ cm}$  above the burner surface and close to the centre<sup>5</sup>.

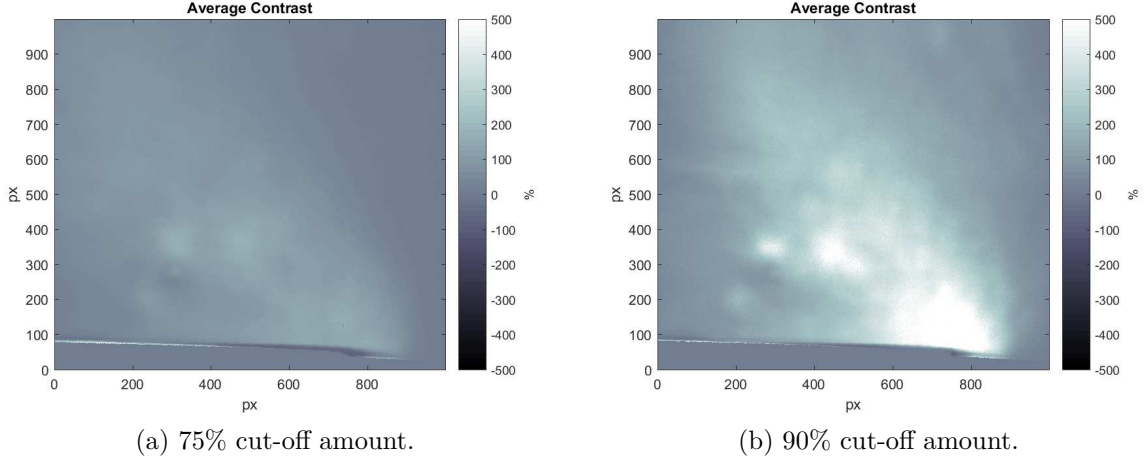


Figure 5.11: *Contrast* mean values for the entire sequence, comparative between two knife-edge filter configurations with different cut-off amounts.

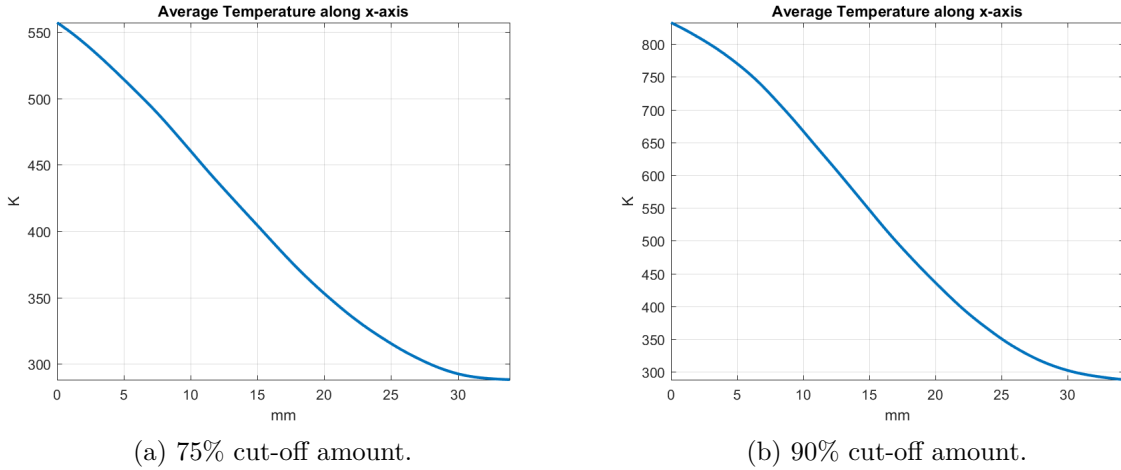


Figure 5.12: *Average temperature along x-axis*, comparative between two knife-edge filter configurations with different cut-off amounts.

As expected, a 90% cut-off amount is the best-fitting solution for most of practical needs in terms of sensitivity and quality of information. In case of extreme temperature variations, is advisable to decrease the cut-off amount, in order to extend the measuring range.

<sup>5</sup>For this region, one can assume a local temperature in a  $1800 \div 2400\text{ K}$  range (see Fig.5.3), which translates in a  $700 \div 850\text{ K}$  maximum average temperature in  $x = 0\text{ mm}$ . These temperature local values are visible on *Average Temperature.fig* in Matlab<sup>®</sup> routine outputs.

### 5.2.3 Shutter Speed Setting

The only way to validate the correct *shutter speed* (see Sec.4.2 at p.70), when microsecond-scale is considered, is through experimental attempts. For this purpose, a  $30 \div 80 \mu s$  *shutter speed* range has been taken into account (see Fig.5.13).

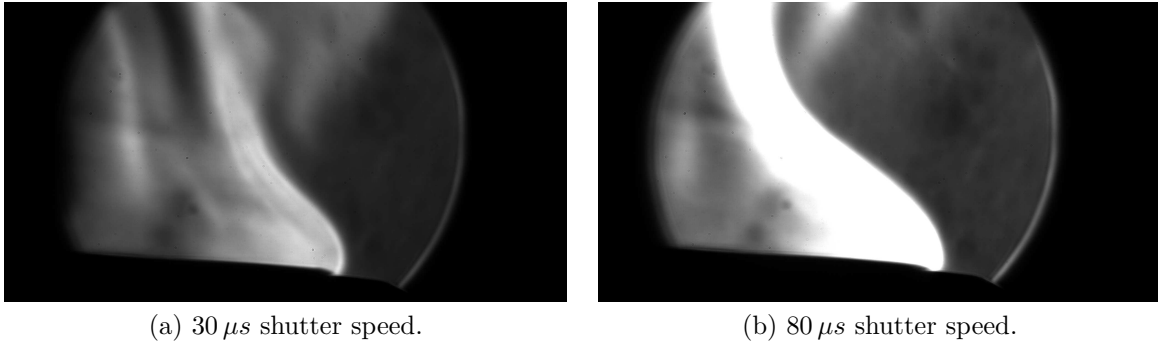


Figure 5.13: Pictures for comparative evaluations between two different *shutter speed* setting.

The  $80 \mu s$  shutter speed image results over-exposed and blurry. A correct exposure requires the grey-scale values of the image to fall in a well-distributed 0-255 range of values. An over-exposed image (see Fig.5.13b) presents most of the information "burned" (presence of totally "white" regions, where most of captured values are equal or close to 255).

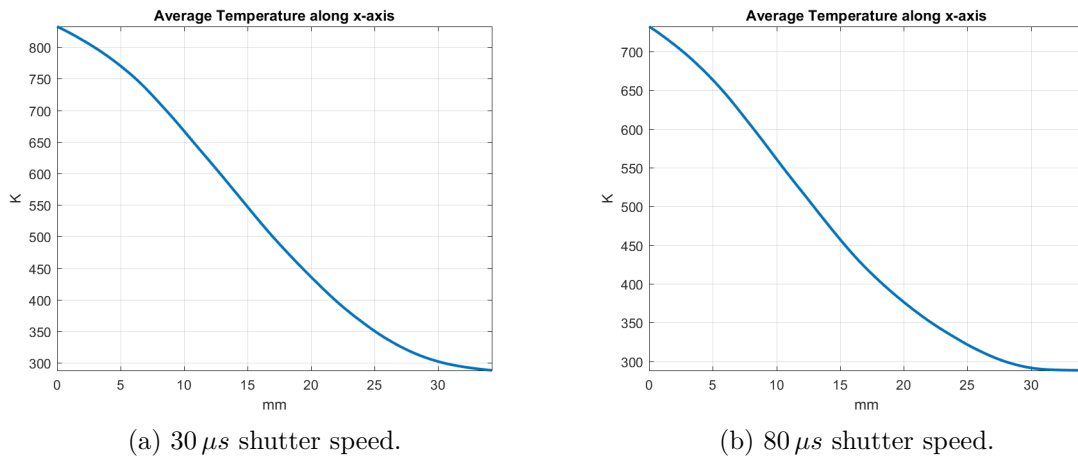


Figure 5.14: *Average temperature along x-axis*, comparative between two different *shutter speed* setting.

This turns into a massive loss of information about contrast levels, which may be higher than the values collected. Consequently, one detects lower levels of temperature gradients for an over-exposed image (see Fig.5.14b) with respect to one with a correct exposure. For our purposes, a  $30 \mu s$  seems a standard setting, then, if this value returns an under-exposed image, the exposure time can grow, in order to achieve the correct exposure.

## 5.2.4 Window Test Sessions

The comparative between *window-on* and *window-off* images has been conducted on MoRaP definitive window component, a synthetic fused silica glass (SQ1 model by Sico<sup>®</sup> Technology GmbH), produced from high purity  $SiCl_4$ , by the flame pyrolysis method. These fused silica glasses are free of bubbles and inclusions and stand out from other materials by good transmission in UV and visible spectral range. The SQ1-models distinguish themselves from other glasses regarding to high homogeneity, deep level of layers, low inclusions and high transmission in the deep UV



Figure 5.15: Synthetic fused silica glass SQ1 model by Sico<sup>®</sup> Technology GmbH.

range. Further details about this component are reported in Tab.5.3:

SQ1 - Synthetic Fused Silica	Technical Specs
OH - Content	$\approx 1200 \text{ ppm.}$
Stress Birefringence (10% outer edge exclusion)	$\leq 10^5 \text{ nm/cm}$
N. of Bubbles (class DIN 58927)	0
Max. area of Bubbles (in $100 \text{ cm}^3$ of glass)	$\leq 0.3 \text{ mm}^2$
Max. area of Inclusions (in $100 \text{ cm}^3$ of glass)	0
Striae (class DIN 3140)	none
Striations (perpendicular to functional dir.)	slight
Refractive-Index change ( $\Delta n$ with small gradients)	$\leq 2 \cdot 10^{-5}$

Table 5.3: SQ1 model by Sico<sup>®</sup> Technology GmbH, technical specifics [39].

The comparative between *window-on* and *window-off* images here presented has merely qualitative purposes. In order to have realistic feedback on numerical evaluation, it would be necessary to run the test in a closed environment (e.g. combustion chamber), but this is not the case, mostly due to lack of instruments at the time of test sessions (the combustion chamber itself was still in manufacturing phase). Consequently, the qualitative tests here presented do not have any numerical feedback, because the *Matlab<sup>®</sup> Image Analysis Routine* in *window-on* conditions is predisposed for working with closed environment only, moreover this kind of analysis requires in-depth knowledge about properties of gas mixture and its residue from the combustion process (e.g refractive index and species con-

centration), thermodynamic characteristics (e.g. BCs for the integration process), and so on. Some references about refractive-index estimate for gas mixtures can be found in [27] studies by J. Owens about its dependence on pressure, temperature and composition and in J.A. Mandarino's works about Gladstone-Dale constant [20].

Despite all, the effects of a *window-on* image on *Matlab*<sup>®</sup> *Image Analysis Routine* outputs is more than evident. Schlieren photography shows a tendency by the window to over-expose the image and also to magnify its proportions, which is a conse-

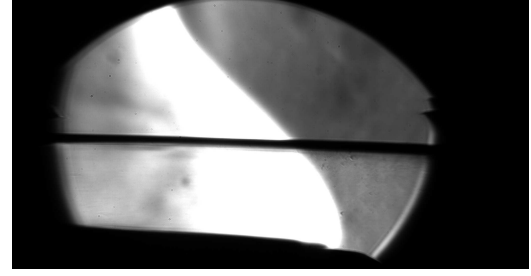


Figure 5.16: Example of a *window-on* arrangement, photo by the author.

quence to refraction of light rays caused by refractive-index variations due to a schlieren object, which makes them strike as not parallel on the inner surface of the mirror. In terms of *contrast* (see Fig.5.17), it results as a global decrease of its value, which seems in contradiction<sup>6</sup> with the analysis conducted in Sec.2.4.3, but this effect may be explained by the tendency of the mirror to over-expose the image, with consequent loss of information in the "burned" regions. As a direct consequence, the temperature levels calculated by *Matlab*<sup>®</sup> *Image Analysis Routine* get lower from *window-off* to *window-on* arrangement. In future applications, this issue could be limited by a correct image exposure.

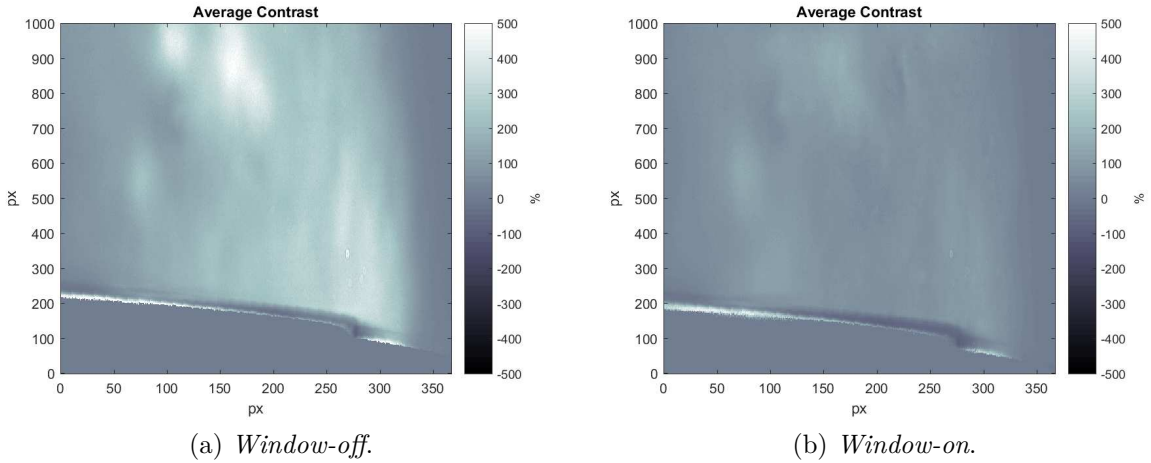


Figure 5.17: *Contrast* mean values, comparative between *window-off* and *windows-on* solutions with no alteration in input data.

<sup>6</sup>According to light propagation theory and geometrical construction, a window placed between a region at higher refractive index and the surrounding air should increase the refraction angle, following Eq.2.28.

The *Matlab<sup>®</sup> Image Analysis Routine* is predisposed to eventually correct the effects of a window for closed flow-field domains, which involves an additional reduction of contrast, accordingly with Eq.2.29 for preliminary studies.

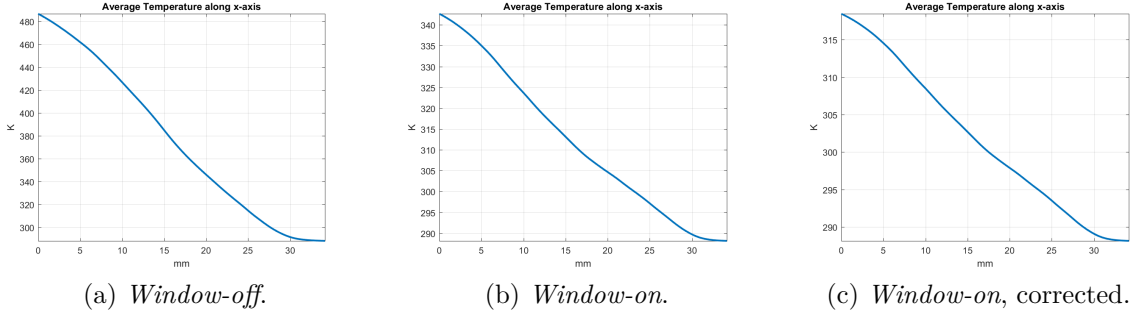


Figure 5.18: Comparative evaluation on *average temperature along x-axis* for different window configuration, in (c) an example of computational correction for windows by Matlab<sup>®</sup> routine.

Of course, its application does not fit our case of study (open burner), because the inputs for schlieren analysis that have been selected are describing an open environment, with air as surrounding medium. The *window-effect correction factor* for the Matlab<sup>®</sup> routine has been predisposed to modelling a closed environment (e.g. combustion chamber) and it is related to exhausted gases originated by a combustion process. In other words, the Matlab<sup>®</sup> routine is affected by the description quality of gas mixture properties, such as density, temperature (both for BCs, before integration process) and the not-trivial evaluation of *refractive index of the mixture*, which requires in-depth knowledge of its composition, with particular attention for MoRaP applications. As anticipated in Sec.5.2.1, will be necessary to involve different research tools, such as experimental measurements from TCs and PCs sensors, chemiluminescence diagnostic, CFD simulation and everything that can help to get as close as possible to realistic numerical evaluation from a schlieren analysis process.

Another interesting detail is the capability of the optical system to exclude eventual defects of the window by reducing the depth-of-field and focusing more on the schlieren object. This technique usually would involve wider f/no. aperture, but there have been no experiments on the system to evaluate the effective efficiency of the method nor its applicability on studies about self-luminous phenomena.

Both the flow-field description (with consequent *window-effect correction factor*) and the avoidance of defects by reducing the DOF will require further research for *window-on* solutions on the optical schlieren system, for future applications on MoRaP.

## 5.3 Test Campaign for Flame Study

Main purpose of this final test campaign is to prove the sensitivity of the optical system to slight variations in combustion parameters, such as *mixture ratio* ( $O/F$ ), in order to predispose the machinery for future applications on MoRaP.

The  $O/F$  parameter, in particular, describes the mass ratio between oxidizer and fuel in the chemical reaction, in particular for  $GOX/GCH_4$  combustion:



where  $x = 1.0$  if oxidizer and fuel are in stoichiometric condition, and  $(\dots)$  are eventual non-reacting gases residual from combustion or exited radicals (e.g.  $OH^*$ ).

In case that stoichiometric condition occurs, the associated  $O/F$  would be:

$$O/F = \frac{m_{O_2}}{m_{CH_4}} = 4.0$$

but it is rare that stoichiometric conditions find practical application, because of the intense amount of heat generated (maximum per unit mass). It is more common to work with *fuel-rich* mixtures, which involve  $O/F$  values in a  $2.0 \div 3.4$  range, for  $20\text{ bar}$  pressure test (typical values for future applications on MoRaP).

The following sequences (from Fig.5.19 to Fig.5.21) represent the evolution of a flame coming from the *McKenna flat burner* in different  $O/F$  conditions, paying particular attention to blasting, anchoring and flame emission through the entire  $1\text{ s}$  sequence.

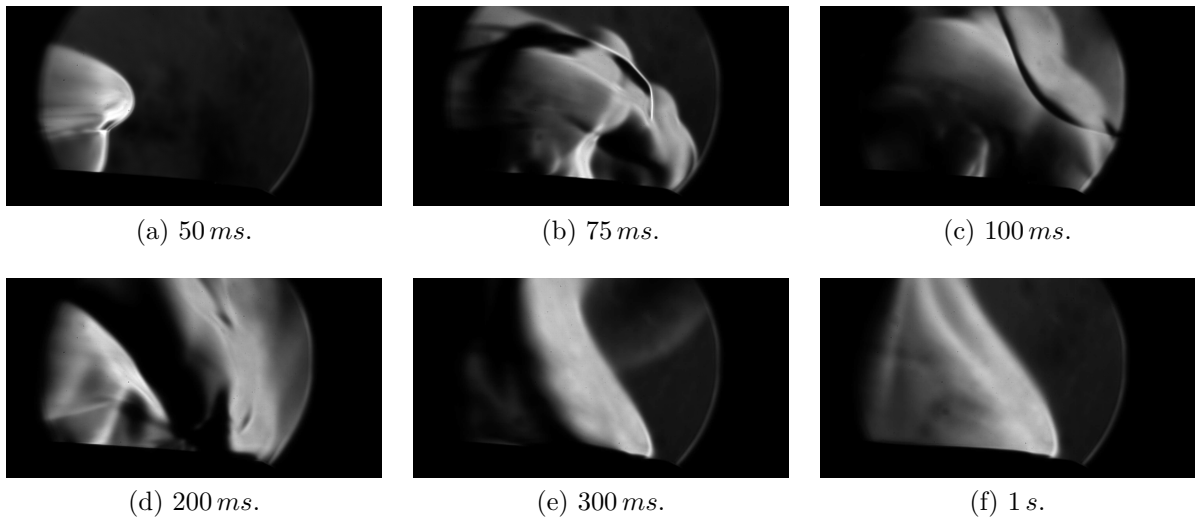


Figure 5.19: Blasting and anchorage of the flame at  $O/F = 2.2$ , captured by the author.

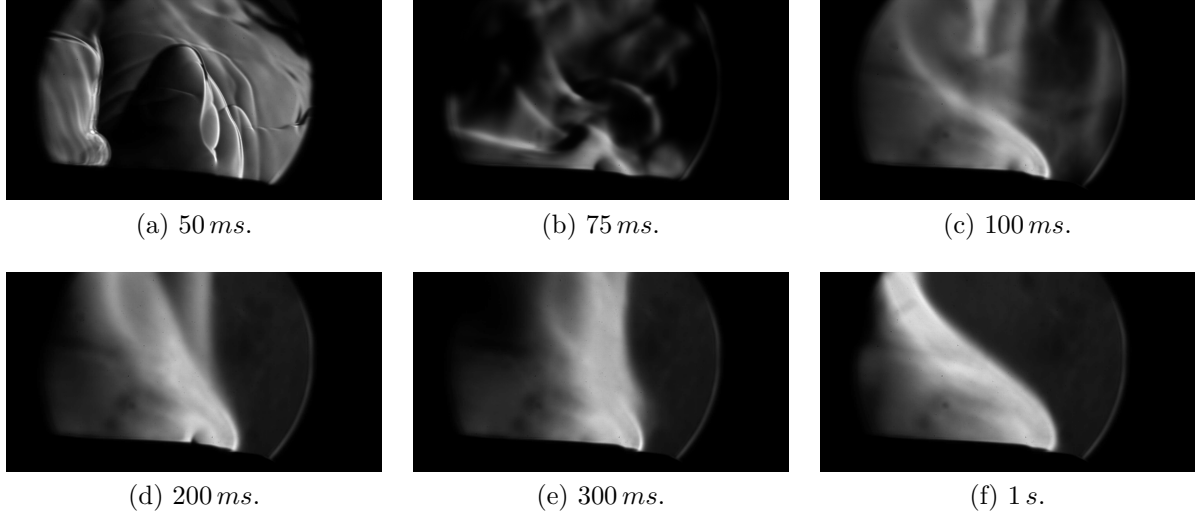


Figure 5.20: Blasting and anchorage of the flame at  $O/F = 3.0$ , captured by the author.

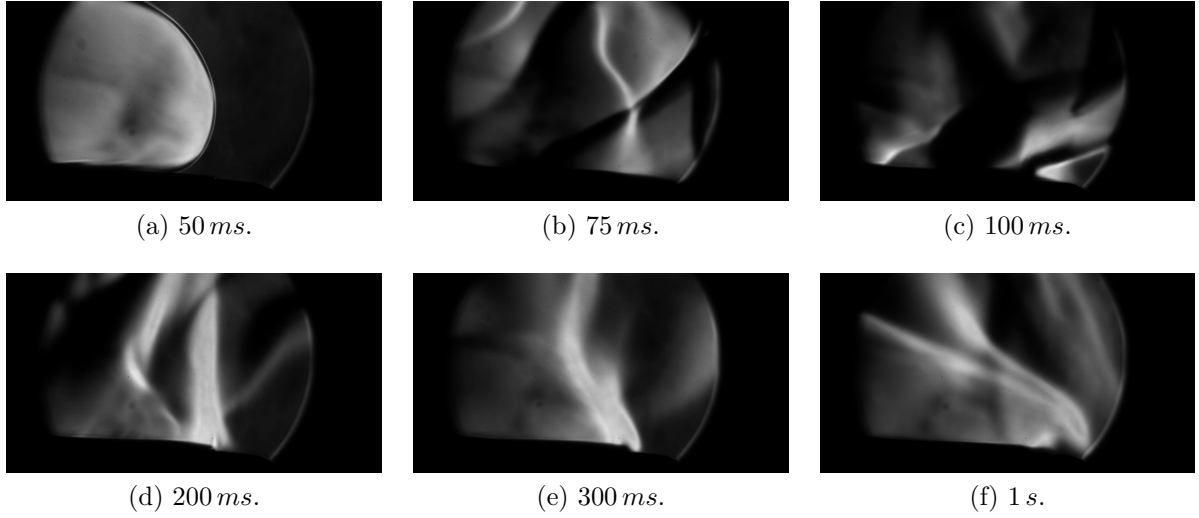


Figure 5.21: Blasting and anchoring of the flame at  $O/F = 3.4$ , captured by the author.

At a first look, flame anchoring and stabilization appear to come later for growing  $O/F$  values, moreover the blasting on  $O/F = 3.0$  and  $O/F = 3.4$  is more violent than for  $O/F = 2.2$ . The  $O/F = 3.4$  has shown a more oscillating motion with respect to lower  $O/F$  values, which would suggest a harder tendency to flame stabilization due to a higher amount of energy associated to combustion process. The flame seems more inclined towards the centre for high  $O/F$  rates with respect to  $O/F = 2.2$ , where it seems to develop in a more vertical direction instead. Currently, it is hard to assert if these effects are entirely associated to  $O/F$  variations or also due to changes in mass-flow rate, which may have affected the results in a not-totally rigorous method of analysis perspective.

The effects on anchoring and flame emission, such as many other predictions on density and temperature, can be validated only after a rigorous comparative analysis between different  $O/F$  ratio for *average values* on the entire 1 s sequence (from Fig.5.22 to Fig.5.29).

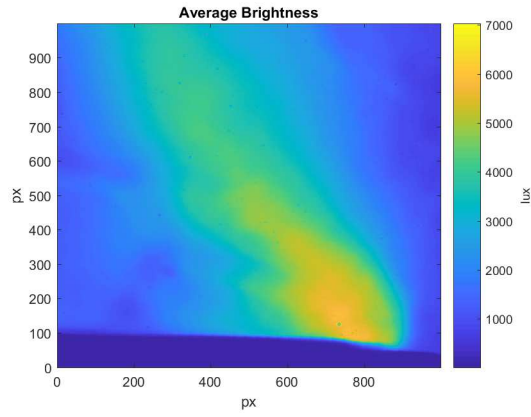
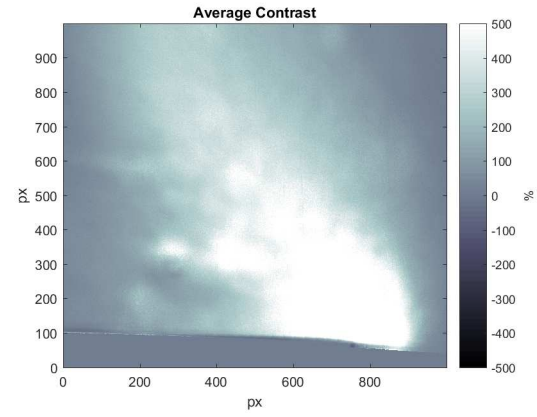
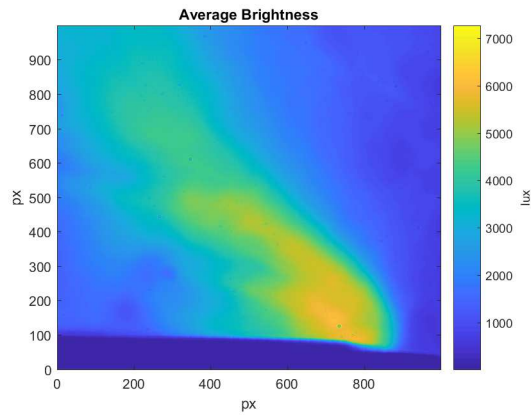
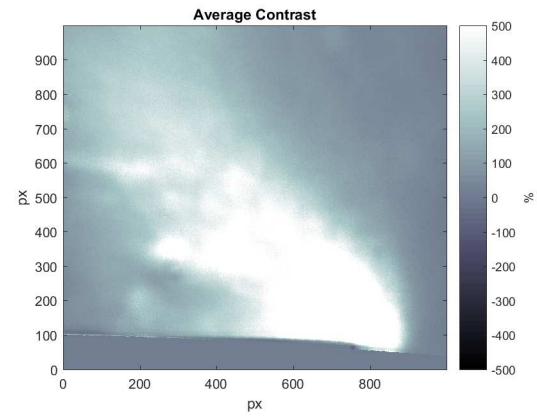
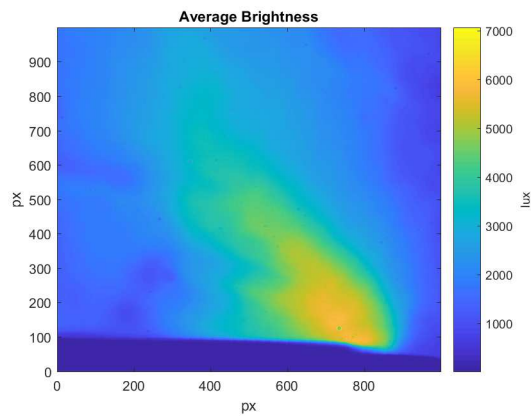
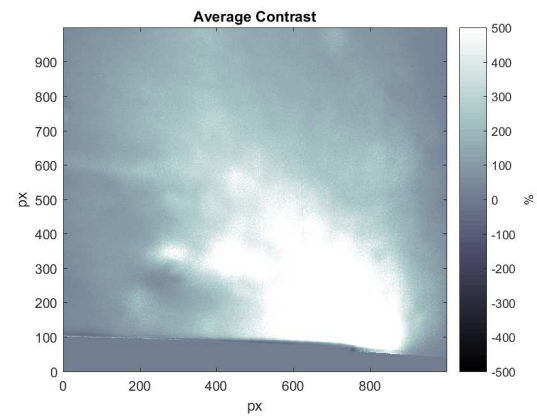
(a)  $O/F = 2.2$ .(a)  $O/F = 2.2$ .(b)  $O/F = 3.0$ .(b)  $O/F = 3.0$ .(c)  $O/F = 3.4$ .(c)  $O/F = 3.4$ .

Figure 5.22: Comparative evaluation on *average brightness* for different  $O/F$ .

Figure 5.23: Comparative evaluation on *average contrast* for different  $O/F$ .

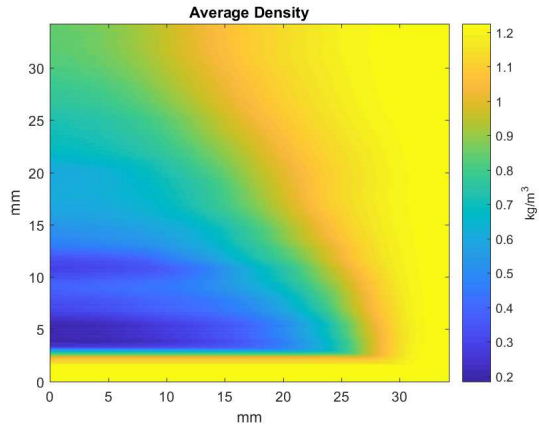
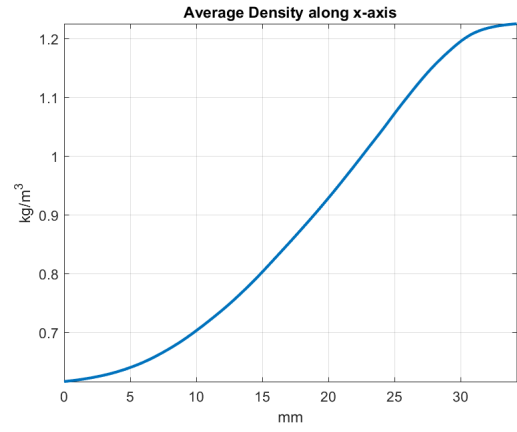
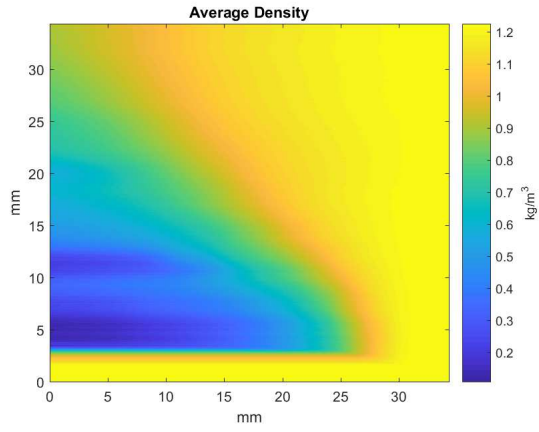
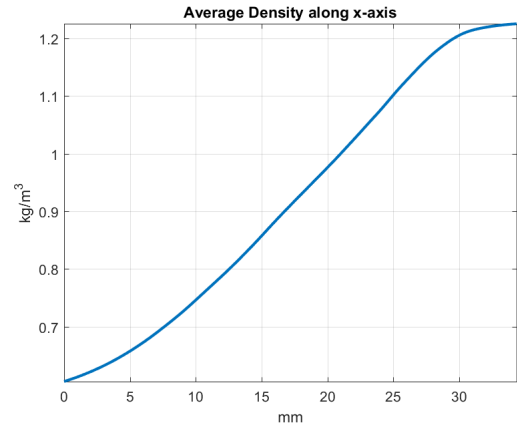
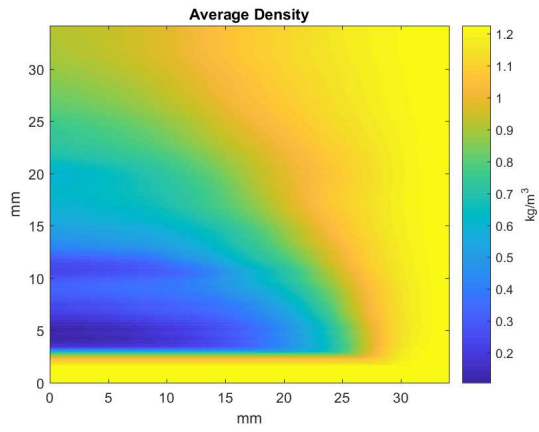
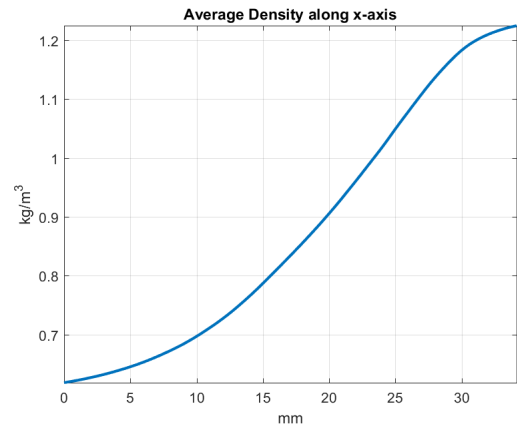

 (a)  $O/F = 2.2$ .

 (a)  $O/F = 2.2$ .

 (b)  $O/F = 3.0$ .

 (b)  $O/F = 3.0$ .

 (c)  $O/F = 3.4$ .

 (c)  $O/F = 3.4$ .

 Figure 5.24: Comparative evaluation on *average density* for different  $O/F$ .

 Figure 5.25: Comparative evaluation on *average density along x-axis* for different  $O/F$ .

As shown in Fig.5.23 and confirmed in Fig.5.24, the  $O/F = 2.2$  flame is less inclined than flames at higher  $O/F$ , moreover the  $O/F = 3.4$  suffers a less stable flame behaviour.

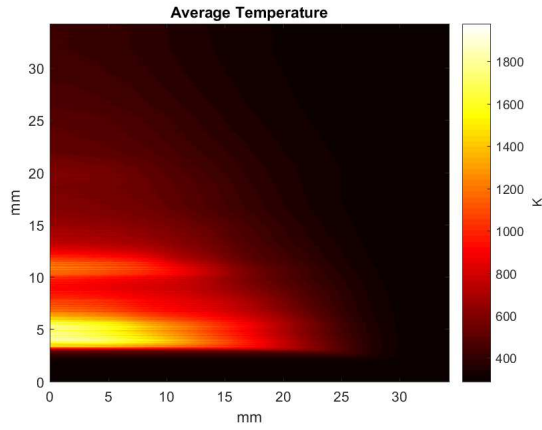
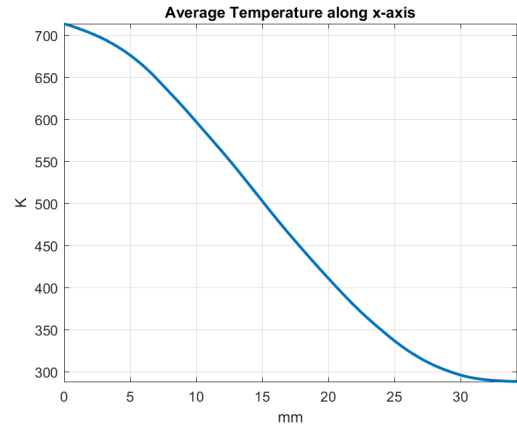
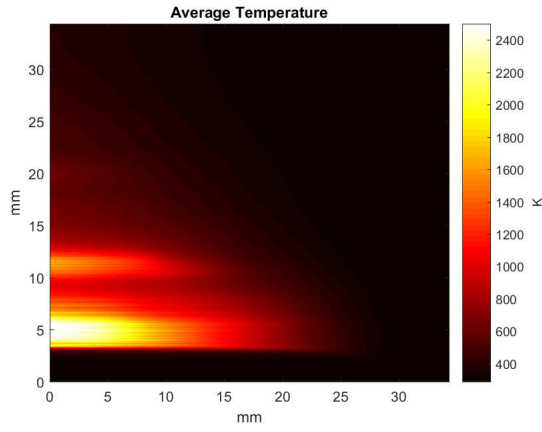
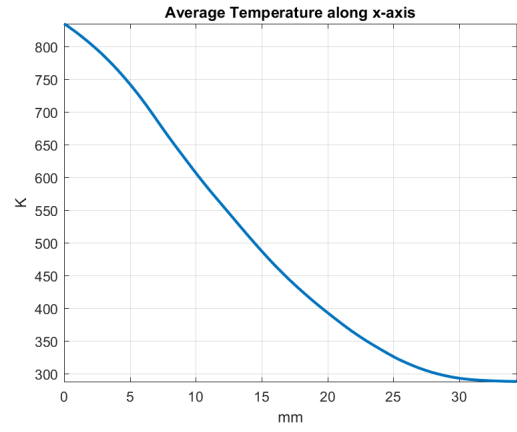
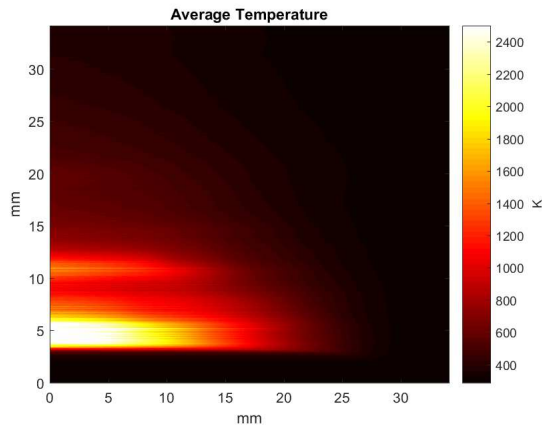
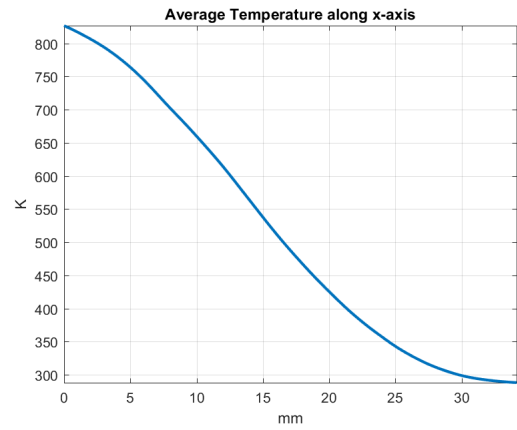

 (a)  $O/F = 2.2$ .

 (a)  $O/F = 2.2$ .

 (b)  $O/F = 3.0$ .

 (b)  $O/F = 3.0$ .

 (c)  $O/F = 3.4$ .

 (c)  $O/F = 3.4$ .

 Figure 5.26: Comparative evaluation on *average temperature* for different  $O/F$ .

 Figure 5.27: Comparative evaluation on *average temperature along x-axis* for different  $O/F$ .

As expected from theory, temperature (mostly) increases with density decreasing at constant pressure, as long as  $dn/dT$  derivative is negative under normal conditions [28, p.14].

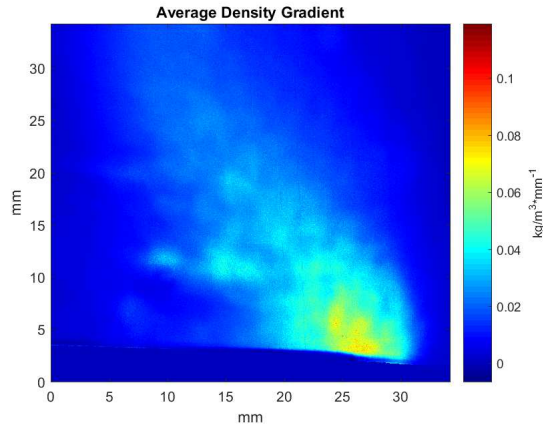
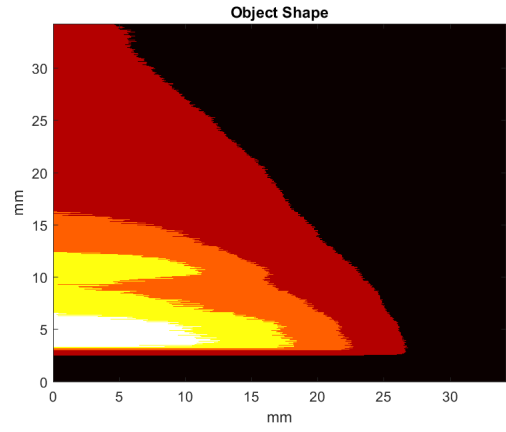
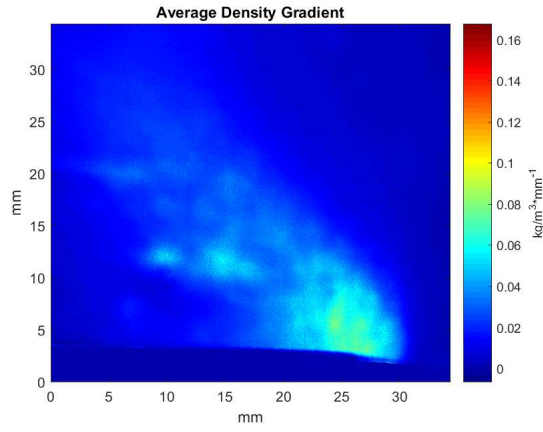
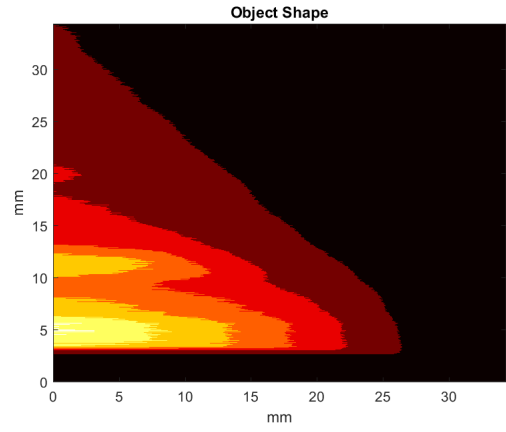
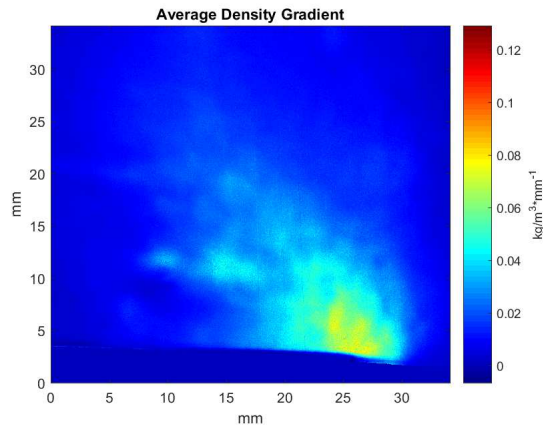
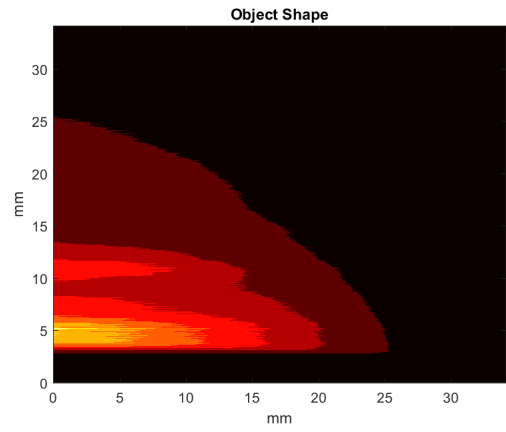

 (a)  $O/F = 2.2$ .

 (a)  $O/F = 2.2$ .

 (b)  $O/F = 3.0$ .

 (b)  $O/F = 3.0$ .

 (c)  $O/F = 3.4$ .

 (c)  $O/F = 3.4$ .

 Figure 5.28: Comparative evaluation on *average density gradient* for different  $O/F$ .

 Figure 5.29: Comparative evaluation on *average temperature shape* for different  $O/F$  by *thresholding* post-processing technique.

Flame instability translates in gradient dispersion (see Fig.5.28c), while increasing  $O/F$  ratio the shape of flames appears more inclined towards the centre (see Fig.5.29).

The first question one should answer is if temperature distribution shows any evident dependence on  $O/F$  ratio. As first step, one could compare the overall increase in temperature along the entire x,y-plane. The results, accordingly to outputs from *Matlab® Image Analysis Routine*, are reported in Tab.5.4.

O/F	2.2	3.0	3.4
$T_{mean}$	477.88 K	490.08 K	517.38
$\Delta T_{mean}$	+189.73 K (+65.84 %)	+201.93 K (+70.08 %)	+229.23 K (+79.55 %)

Table 5.4: Comparative evaluation on *average temperature overall mean value* for different O/F,  $\Delta T$  and percentage results with respect to  $T_{amb} = 288.15 K$ .

The coherent tendency to increase overall temperature with  $O/F$  value confirms the sensitivity of the schlieren optical system to this parameter. On the other hand, data reported in Tab.5.4 is a simple evaluation of temperature mean value along the entire x,y-plane. In order to investigate further flame properties, a comparative between temperature distribution along x-axis has been carried on. Results are reported in Tab.5.5.

O/F	2.2	3.0	3.4
[mm]	[K]	[K]	[K]
0	713	834	827
5	676	742	764
10	596	606	660
15	502	487	538
20	410	393	426
25	336	326	343
30	296	293	299
35	288	288	288

Table 5.5: Comparative evaluation on *average temperature distribution along x-axis* for different O/F at specific x-coordinates.

One could distinguish the results in three categories: *green* for results in accordance with theory and expectations; *red* for results that contradict expectations; *orange* for results that in appearance seem to contradict expectations but have a physical explanation. In this case, the increase in temperature seems in good accordance with expectations, with notable results in  $x = 5 mm, 10 mm$  (where wider differences in temperature occur). The *red* results in  $x = 0 mm$  could be due to numerical errors that manifest at the base of

the burner, due to its presence in the integration flow-field<sup>7</sup>. Instead, the region of *orange*

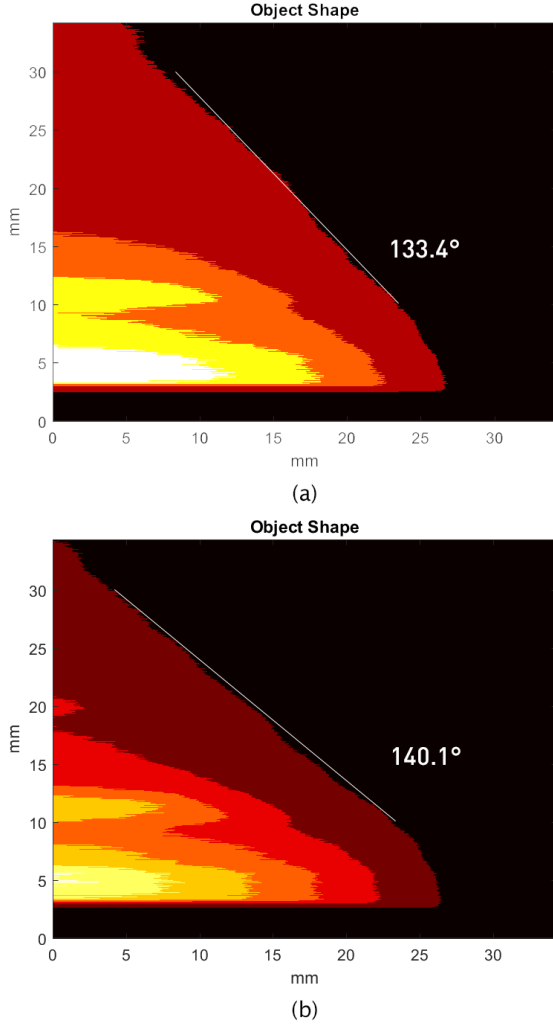


Figure 5.30: Comparative between flame inclination angles (in average) for  $O/F = 2.2$  (a) and  $O/F = 3.0$  (b) respectively.

results seems to contradict our expectations, patently showing higher temperature levels for the  $O/F = 2.2$  ratio despite of  $O/F = 3.0$ , but this phenomenon could find a physical explanation if one considers the effects of a flame more inclined towards the central region (see Fig.5.30). The results in Tab.5.5 are evaluation of mean values along y-axis of average temperature for specific x-coordinates, which implies lower temperature results for x-coordinates away from the centre for a more inclined flame (on average) and a much more rapid increase for x-coordinates closer to centre, which explains the higher overall temperature on x,y-plane for  $O/F = 3.0$  with respect to  $O/F = 2.2$ . A similar dependence on average inclination appears undetectable in  $O/F = 3.4$ , due to instability on flame emission, that translates into dispersion of temperature gradient along the x,y-plane, which unavoidably leads to a fictitious representation of the shape of flame in an *average temperature* comparative through *thresholding* post-processing technique (see Fig.5.30).

<sup>7</sup>This kind of numerical errors should not manifest in MoRaP future applications, because the only region of interest will be the flow-field itself, excluding any presence of external body nor surfaces.

## Conclusions

The schlieren optical system proved great sensitivity to slight refractive-index variations due to inhomogeneities in the flow-field along the optical path, together with reduced astigmatism and diffraction effects and almost null comatic aberrations. At higher cut-off amounts, even wind effects on still air and human body heat become. A correct exposure of the image can offer a powerful instrument for qualitative evaluation on a wide range of phenomena. The system is fully compatible with MoRaP and its previous investigation instrumentation, providing a support system for chemiluminescence analysis. Moreover, thanks to its versatility, the optical system could find many applications in different projects of interest for LFA.

The step-by-step calibration guide offered to the operator, which includes a specific section dedicated to most common practical issues and alternative solutions, is an useful tool that can speed up any calibration procedure with guaranteed results of success. For future applications, the optical system could be improved even further by adopting some of the possible solutions drafted in the brief list offered to the reader at the end of the chapter dedicated to project design.

The preliminary test session on the flat flame burner outlined a standard setting for a correct calibration of the system and highlighted the system sensitivity to changes in temperature and density due to mixture ratio variations. The Matlab® routine for image-processing has been heavily improved and adapted to analyses based on schlieren technique. Unfortunately, because of many over-simplified hypotheses, the quantitative evaluation is inevitably affected by errors, which penalize the realism of the solution for density and temperature distribution. To overcome these simplified results, it will be necessary (for future applications on MoRaP) to describe the fluid properties into the observable volume by average values along the optical axis, which will require in-depth understanding of the fluid dynamics of the problem, involving different research tools, like measurements from thermocouples and pressure transducers, CFD modelling and chemiluminescence diagnostics.

Despite its flawed numerical results, the optical system currently constitutes an useful tool for quantitative evaluation in comparative tests, such as sensitivity to mixture ratio and species concentrations variations, and an extremely powerful diagnostic tool for qualitative evaluation, such as shape of flame evaluation, fluid dynamic behaviour, boundary layer study and detection of recirculation regions.

# References

- [1] BARNES, N.F. & Bellinger S.: Schlieren and Shadowgraph Equipment for Air Flow Analysis. In: *Journal of the OPTICAL SOCIETY of AMERICA* Vol.35, n.8 (August 1945), S. 1–22
- [2] BAUER, C. & Schlieben G. & Eiringhaus D. & Haidn O.: *Design and commission of a mobile GOX/GCH<sub>4</sub> rocket combustion test bed for education and collegiate research*. Institute for Flight Propulsion (LFA) & Scientific Workgroup for Rocketry and Spaceflight (WARR), Technische Universität München, Munich, Germany, June 2013
- [3] BORN, M. & Wolf E.: *Principles of optics: electromagnetic theory of propagation, interference and diffraction of light*. 7th Ed. Georg-August-Universität, Göttingen, Germany and University of Edinburgh : Cambridge University Press, 1999
- [4] BROWN, C.: *Introduction to the Flat Flame Burner and its use in Combustion Diagnostics applications*. – Business Manager, ERC (Webinair Series)
- [5] BURTON, R.A.: *The application of schlieren photography in fluid flow and heat transfer analysis*. M.S.M.E. Thesis, University of Texas. 1951
- [6] CRANZ, C.: *Lehrbuch der Ballistik*. Vol. 3. Springer-Verlag, Berlin 1927
- [7] DALZIEL, S.B. & Hughes G.O. & Sutherland B.: *Whole-field density measurements by 'synthetic schlieren'*. The University of Cambridge, Silver Street, Cambridge CB3 9EW, England, 27 Oct. 1998
- [8] DUGGER, P.H. & Hill J.: A new dimension in front-light laser photography. In: *AIAA J.*, 1972
- [9] EDMUND.OPTICS, Inc: *Fixed Focal Length Lens C-Mount Spacer Kit*. <https://www.edmundoptics.com/f/fixed-focal-length-lens-c-mount-spacer-kit/12400>, 2019. – 101 East Gloucester Pike, Barrington, NJ 08007-1380 USA
- [10] FLATFLAME.COM: *Holthuis & Associates - Flat Flame Burners: Burner Description*. <http://www.flatflame.com/burner-description.html>. – 2013
- [11] HARGATHER, M.J. & Settles G.: A comparison of three quantitative schlieren techniques Opt. Lasers. In: *Eng. 50*, 8-17 (2012)
- [12] HOLDER, D.W. & North R.: *Schlieren methods*. NPL notes on applied science no.31. London : Her Majesty's Stationery Office, 1963
- [13] HOSCH, J.W. & J.P. W.: *High spatial resolution schlieren photography*. Ed.I. 1977
- [14] HUANG, C. & Gregory J.W. & Sullivan J.: *A modified schlieren technique for micro flow visualization*. School of Industrial Engineering, Purdue University, West Lafayette, IN 47907, USA - Department

- of Aeronautics, US Air Force Academy, USAF Academy, CO 80840, USA - School of Aeronautics and Astronautics, Purdue University, West Lafayette, IN 47907, USA, April 2007
- [15] HYZER, W.G.: *Engineering and scientific high-speed photography*. Ed.I. New York : The Macmillan Company, 1962
  - [16] JENKINSON, L.R. & Simpkin P. & Rhodes D.: *Jet Aircraft Design*. I Ed. American Institute of Aeronautics and Astronautics, 1999
  - [17] KAISER, S.A. & Salazar V.M. & Hoops A.: *Schlieren measurements in the round cylinder of an optically accessible internal combustion engine*. University of Duisburg-Essen, Duisburg 47048, Germany, 10 May 2013
  - [18] KEAN, L.: A contribution to the theory of schlieren sensitivity and quantitative evaluation. In: *USAF Systems Command Report ASD-TDR-62-924* (1962)
  - [19] LUTUS, P.: *OpticalRayTracer*. <https://arachnoid.com/OpticalRayTracer>
  - [20] MANDARINO, J.A.: The Gladstone-Dale Relationship: Part IV. The Compatibility Concept and its Application. In: *Canadian Mineralogist* Vol. 19, pp. 441-450 (1981)
  - [21] MAZUMDAR, A.: *Principles and Techniques of Schlieren Imaging Systems*. Columbia University, Department of Computer Science, July 2011
  - [22] MEIER, G.E.A.: *Computerized background-oriented schlieren*. DLR-Institute of Aerodynamics and Flow Technology, Bunsenstr. 10, 37073, Göttingen, Germany, June 2002
  - [23] NEWPORT.COM: *20DC1000ER.1*. <https://www.newport.com/p/20DC1000ER.1>
  - [24] NEWPORT.COM: *20SJ00ER.3*. <https://www.newport.com/p/20SJ00ER.3>
  - [25] OKUGAWA, S.: Method of and apparatus for detecting defect of transparent sheet as sheet glass. In: *US Patent 5*, Sept. 1995
  - [26] OPPENHEIM, A.K. & Urtiew P.A. & Weinberg F.: On the Use of Laser Light Sources in Schlieren-Interferometer Systems. In: *Proceedings of the Royal Society of London. Series A, Mathematical and Physical Sciences* Vol. 291, N. 1425 (Apr. 1966), S. 279–290
  - [27] OWENS, J.C.: Optical Refractive Index of Air: Dependence on Pressure, Temperature and Composition. In: *APPLIED OPTICS 51* Vol. 6, No. 1 (Jan. 1967)
  - [28] PANIGRAHI, P.K. & K. M.: *Schlieren and Shadowgraph Methods in Heat and Mass Transfer*. Ed.I. Dep. of Mech. Eng., Indian Institute of Technology, Kanpur, Uttar Pradesh, India : Springer New York Heidelberg Dordrecht London, 2012 (In *Springer Briefs in Applied Sciences and Technology · THERMAL ENGINEERING AND APPLIED SCIENCE*)
  - [29] PIERCE, A.J. & Lu F.: Laser Alignment Method for Portable Schlieren System. In: *39th AIAA Fluid Dynamics Conference*. San Antonio, Texas, 22-25 June 2009
  - [30] PRAST, G.: Quantitative measurements by the Schlieren method. In: *Philips Tech. Rev.* 43 No. 7 (July 1987), S. 184–191
  - [31] QIOPTIQ.COM: *WinLens3D Basic*. <https://www.qioptiq-shop.com/en/Optics-Software/Winlens-Optical-Design-Software/Free-Winlens-Basic/Free-software-Winlens-Basic.html>

- 
- [32] SCHARDIN, H.: *Das Toeplersche Schlierenverfahren: Grundlagen für seine Anwendung und quantitative Auswertung*. 1934 (VDI-Forschungsheft No.367)
  - [33] SCHARDIN, H.: *Die Schlierenverfahren und ihre Anwendungen*. 1942 (*Ergebnisse der Exakten Naturwissenschaften*, English translation available as NASA TT F12731)
  - [34] SETTLES, G.S.: *Schlieren and Shadowgraph Techniques: Visualizing Phenomena in Transparent Media*. Ed.I. 301 D Reber Building, University Park, PA 16802, USA : Springer-Verlag Berlin Heidelberg New York, 2001 (In *Experimental Fluid Mechanics*)
  - [35] SETTLES, G.S. & Hargather M.: A review of recent developments in schlieren and shadowgraph techniques. In: *Meas. Sci. Technol.* N. 28 (Feb. 2017), S. 25pp
  - [36] SFBTR40.DE: *Division K: Thrust Chamber*. <http://www.sfbtr40.de/index.php?id=divisionk>
  - [37] SHAFER, H.J.: *Physical optic analysis of image quality in schlieren photography*. Ed.I. 1949 (*Journal of the SMPE*, 53(11))
  - [38] SHAMPINE, L.F. & Reichelt M.: The MATLAB ODE Suite. In: *IAM Journal on Scientific Computing* Vol. 18 (1997), S. 1–22
  - [39] SICO.TECHNOLOGY, GmbH: *Synthetic Fused Silica SQE, SQ0, SQ1, SQ2: Datasheet*. <http://www.sico.at/en/quartz.html>
  - [40] SIVESTRI, & Haidn O. S. & Celano M.P. & Schlieben G. & Kirchberger C C. S. & Celano M.P. & Schlieben G. & Kirchberger C: *Characterization of a COX-GCH<sub>4</sub> Single Element Combustion Chamber*. 7TH EUROPEAN CONFERENCE FOR AERONAUTICS AND SPACE SCIENCES (EUCASS), 2017
  - [41] SPEAK, G.S. & Walters D.: *Optical considerations and limitations of the schlieren method*. ARC R&M 2859, British Aero, Research Council, 1950
  - [42] STEEMKR.COM: *Aperture - Digital Photography*. <https://steemkr.com/photography/@apteacher/aperture-digital-photography>
  - [43] TAYLOR, H.G. & Waldram J.: *Improvements in the schlieren method*. J. Sci. Inst., 1933
  - [44] TOEPLER, A.: *Optischen Studien nach der Methodeder Schlierenbeobachtung*. 7th Ed. Poggendorfs Annalen der Physik und Chemie N. 131, 1867. – 33–55 S.
  - [45] TOSHIBA.TELI, Corporation: *BU Series-CMOS Camera*. <http://www.toshiba-teli.co.jp/index.htm>, 2013-2014. – 7-1,4-chome Asahigaoka, Hino-shi,Tokyo,191-0065, Japan
  - [46] VASILIEV, L.A.: *Schlieren methods*. New York : Ed. A. Baruch., 2001 (In *Israel Program for Scientific Translations*)
  - [47] VERSLUIS, M.: High-speed imaging in fluids. In: *Exp. Fluids* N. 54 (2013), S. 1458
  - [48] WELLS, C.B.: Knife-Edge Controller for a Schlieren System. In: *APPLIED OPTICS* Vol. 4, No. 7 (July 1965), S. 815–818
  - [49] WERNET, M.P. & Stiegemeier B.: *Application of Background Oriented Schlieren for Altitude Testing of Rocket Engines*. Glenn Research Center, Cleveland, Ohio & Axiometix, Shawnee Mission, Kansas, Oct. 2017

- [50] WIKIPEDIA.ORG: *Image Sensor Format*. [https://en.wikipedia.org/wiki/Image\\_sensor\\_format](https://en.wikipedia.org/wiki/Image_sensor_format)
- [51] WIKIPEDIA.ORG: *Infinity Focus*. [https://en.wikipedia.org/wiki/Infinity\\_focus](https://en.wikipedia.org/wiki/Infinity_focus)
- [52] WILLERT, C.E. & Stasicki B. & Klinner J. & Moessner S.: Pulsed operation of high-power light emitting diodes for imaging flow velocimetry. In: *Meas. Sci. Technol.* N. 21 (2010)
- [53] WILSON, S. & Gustafson G. & Lincoln D. & Murari K. & Johansen C.: Performance evaluation of an overdriven LED for high-speed schlieren imaging. In: *J. Vis.* N. 18 (2015), S. 35–45
- [54] WINTER, F. & Silvestri S. & Celano M.P. & Schlieben G. & Haidn O.: *High-speed and Emission Imaging of a Coaxial Single Element GOX/GCH<sub>4</sub> Rocket Combustion Chamber*. 7TH EUROPEAN CONFERENCE FOR AERONAUTICS AND SPACE SCIENCES (EUCASS), July 2017
- [55] WOLTER, H.: Schlieren-, Phasenkontrast- und Lichtschnittverfahren. In: *S. Flüge, Handbuch der Physik* Bd. 24, Springer (Berlin 1956), S. 555–645

## **Appendix A**

# **Matlab<sup>®</sup> Image Analysis Routine**

## A.1 Program Structure Tree

### MATLABImageAnalysisROUTINEv1\_0<sup>1</sup> (November 2018)

- **Images\_Import** This Matlab Script is meant to collect all data from a set of images previously taken and collected in a specific folder. Prints RAW IMAGES, ROTATED IMAGES and WINDOWED&ROTATED IMAGES on screen and video file.

– INPUT

- Images FOLDER
- Images CUTTING BOUNDARIES
- ANGLE OF CORRECTION
- Video FRAMES PER SECOND

– SECTIONS

- PRE-ROUTINE
- IMAGE IMPORT ROUTINE
- OUTPUT ROUTINE

– OUTPUT

- 'Images\_Windowed.mat' → WINDOWED&ROTATED IMAGES on a 3D matrix
- 'map.mat' → COLOR PROFILE on a 2D matrix

- **Images\_Processing** This Matlab Script is meant to extract raw images in a specific temporal interval from 'Images\_Windowed.mat' (in test folder) and removes video noise by subtracting a REFERENCE IMAGE (wind-off). Prints REFERENCE IMAGE, RAW IMAGES and DIFFERENCE IMAGES on screen.

– INPUT

- Images FOLDER
- EVALUATION TIME FACTOR
- EVALUATION WINDOW

– SECTIONS

- PRE-ROUTINE
- IMAGE PROCESSING ROUTINE

– OUTPUT

- RAW IMAGES → unmodified raw images from test session
- DIFFERENCE IMAGES → difference between RAW and REFERENCE
- REFERENCE IMAGE → "wind-off" test image

---

<sup>1</sup>Matlab<sup>®</sup> Image Analysis Routine (v1.0 November 2018)

Created by: Giuseppe Scarlatella

Date: 13/11/2018

Version: 1.0 (November 2018)

Software based on Matlab<sup>®</sup> 2017a (Image Processing Toolbox<sup>TM</sup> required)

Software system based on Windows 10 OS (Apple and Linux compatible)

Terms of Use: all intellectual rights reserved to Lehrstuhl für Turbomaschinen und Flugantriebe - Fakultät für Maschinenwesen - TUM. Any resource relative to the Matlab<sup>®</sup> Image Analysis Routine must be shared under specific authorization by Lehrstuhl für Turbomaschinen und Flugantriebe - Fakultät für Maschinenwesen - TUM and for specific research purposes only. Any other purpose will violate this Terms of Use and TUM policies. Any software material, including developer tools and sample code (collectively "Software"), are subject to this specific Terms of Use, unless TUM has provided those items to final user under more specific terms, in which case, those more specific terms will apply to the relevant item.

- **Schlieren\_\_Technique** This Matlab Script conducts a Schlieren Analysis on processed images. Prints IMAGE DIFFERENCE and CONTRAST on screen. Then evaluates density gradient along a specific axis, integrates this gradient through differential equation for density and temperature, prints on screen these results and saves them in the test folder.

– **INPUT**

- Images FOLDER
- RAW IMAGES
- DIFFERENCE IMAGES
- REFERENCE IMAGE

– **SECTIONS**

- PRE-ROUTINE
- SCHLIEREN IMAGE PROCESSING ROUTINE
- SCHLIEREN FLUID DYNAMIC ANALYSIS ROUTINE
- OUTPUT ROUTINE

– **OUTPUT**

- 'Contrast.mat' → CONTRAST IMAGES on a 3D matrix
- 'Density.mat' → AVERAGE DENSITY IMAGE
- 'Temperature.mat' → AVERAGE TEMPERATURE IMAGE
- 'X-Axis.mat' → Current X-AXIS info vector
- 'Y-Axis.mat' → Current Y-AXIS info vector

- **Chemiluminescence\_\_Technique** This Matlab Script conducts Chemiluminescence Analysis on processed images. Prints REFERENCE IMAGE, RAW IMAGES and DIFFERENCE IMAGES on screen.

– **INPUT**

- Images FOLDER
- RAW IMAGES
- DIFFERENCE IMAGES

– **SECTIONS**

- PRE-ROUTINE
- CHEMILUMINESCENCE IMAGE PROCESSING ROUTINE

## A.2 Flow-field Models

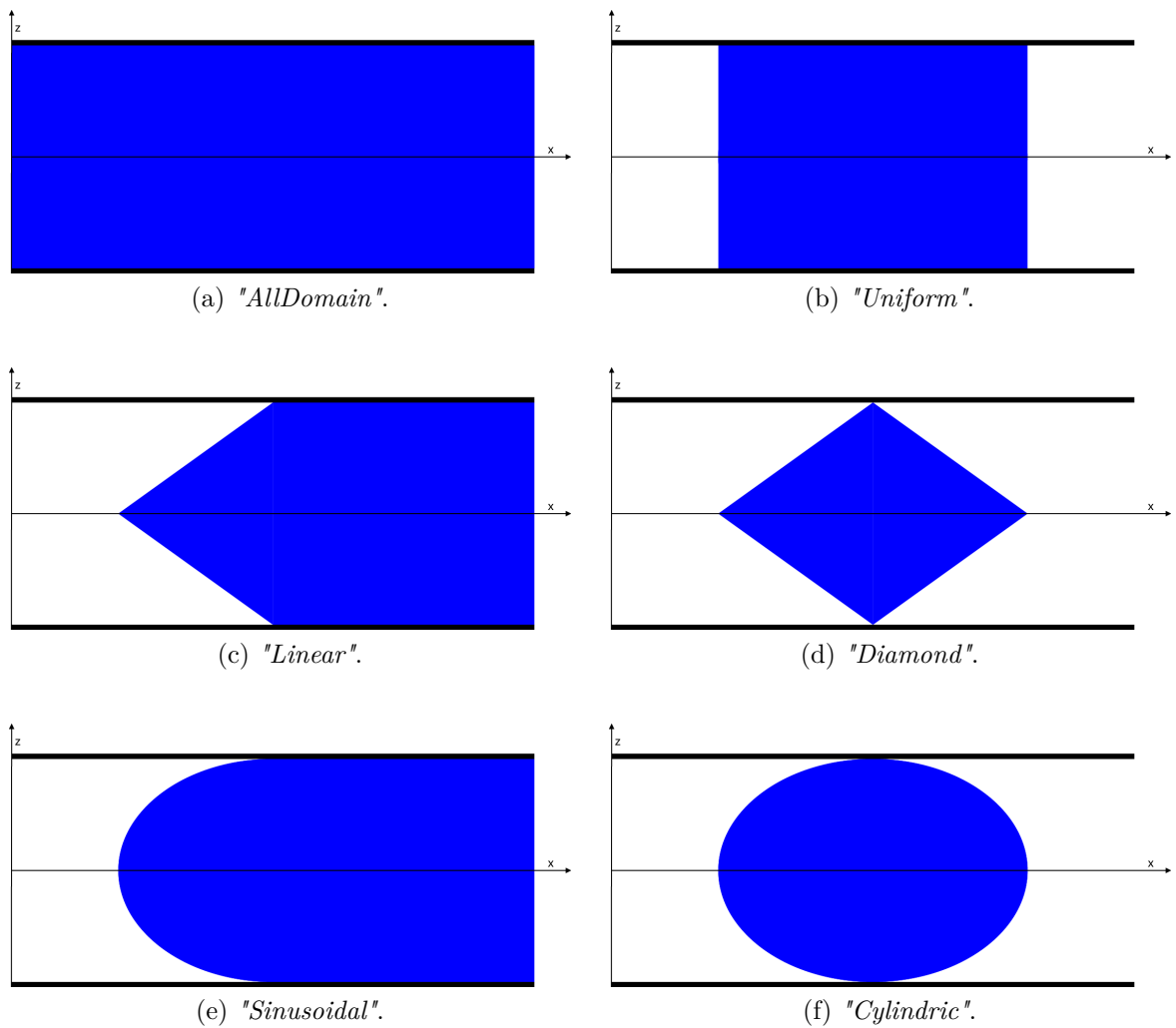
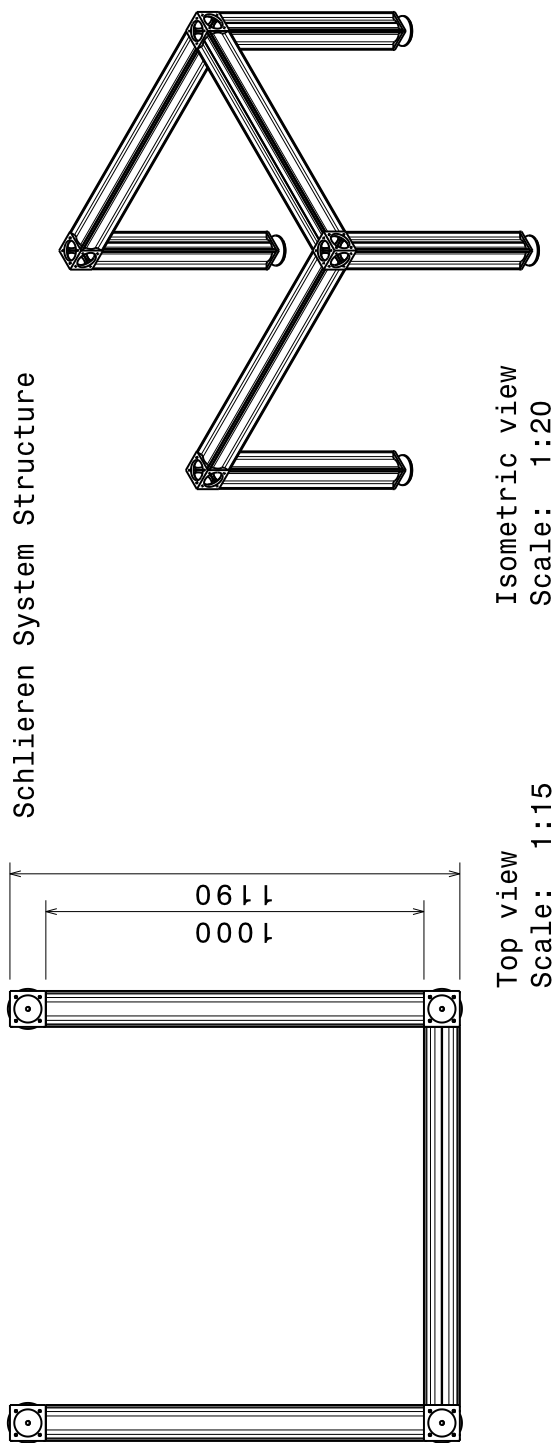


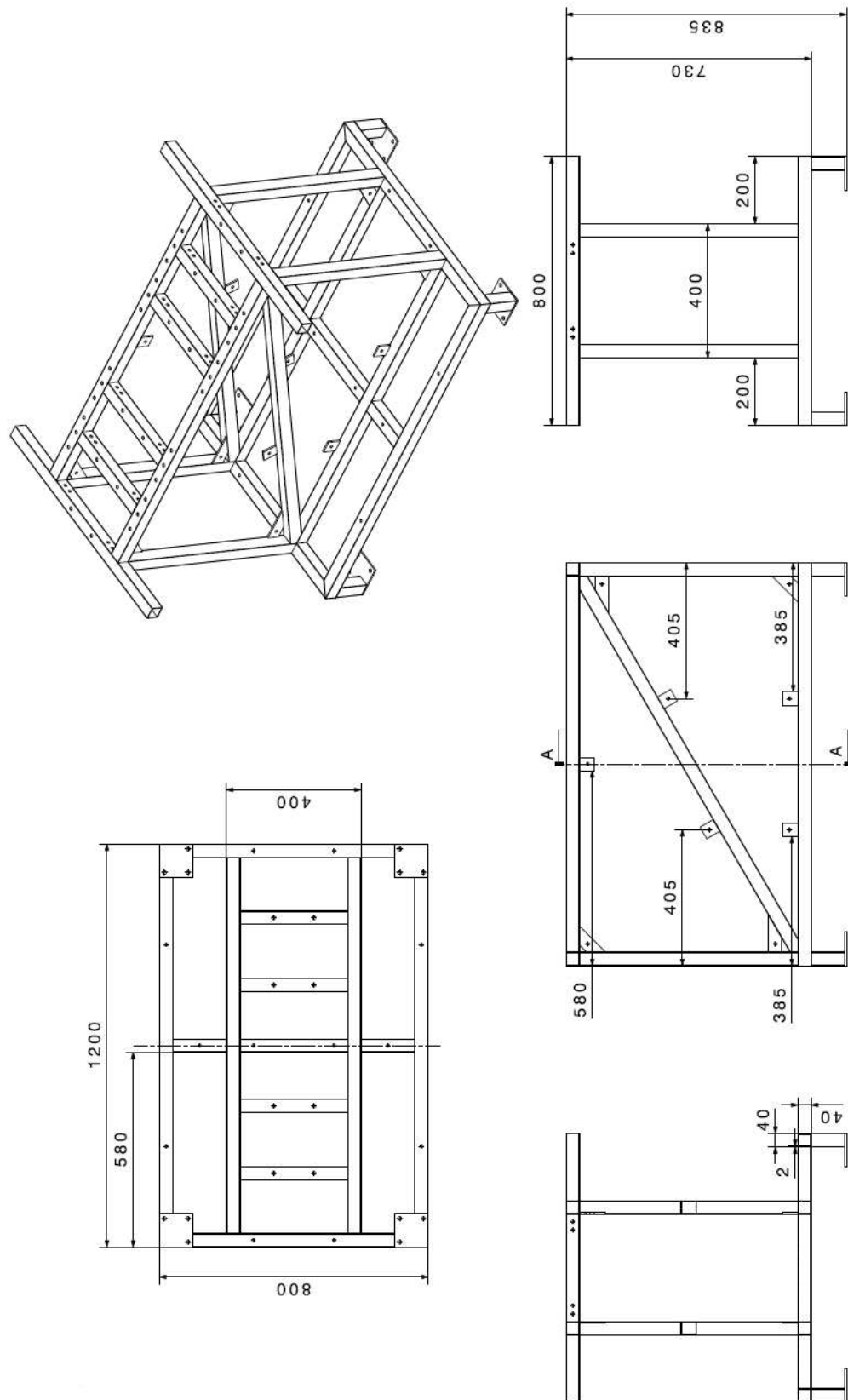
Figure A.1: Pictures covering 6 types of flow-field models included in the Matlab<sup>®</sup> Image Analysis routine, optical axis along  $z$ .

## **Appendix B**

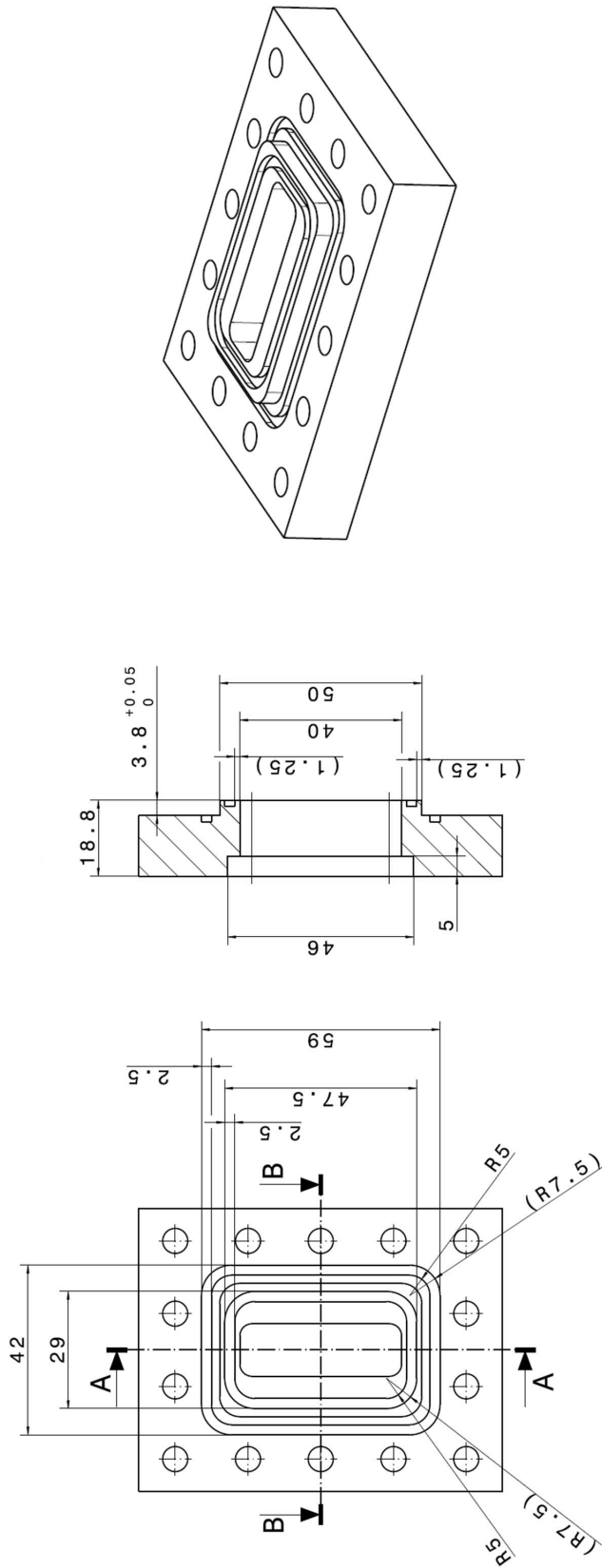
# **Technical Drawings**



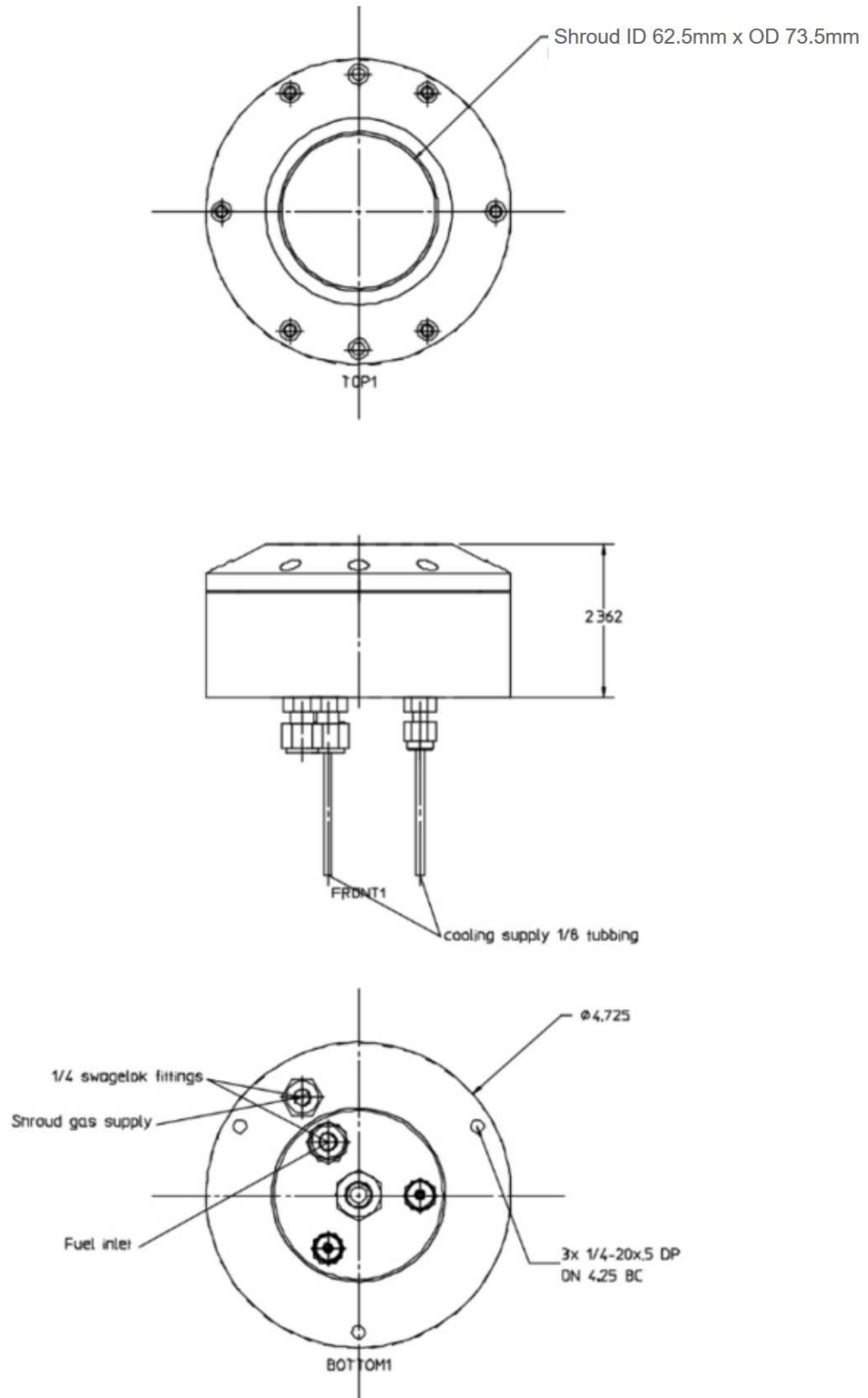
MoRaP Support Structure



Combustion Chamber Windows



# McKenna Standard Bronze Burner



## **Appendix C**

### **Components List**

Component	(Code)	Qty
Concave Mirror	(20DC1000ER.1)	2
Alt. Flat Mirror	(75J00ER.3)	-
Adjustable Height Column 75mm		3
M3 Bolt		+30
M6 Bolt		+20
Carrier 50x95x50mm		5
Carrier 50x95x80mm		1
CMOS Camera	(TM-BU-205)	1
CMOS Camera Mount		1
Condenser Lens		1
Connecting Clamp Orthogonal 14mm		2
Flat Mirror		1
Focusing Lens		1
Knife-Edge Filter		1
Light Regulator	(ID12)	1
LED Light Source		1
Lens Support		1
Levelling Foot		4
Light Source Rotating Support		1
Breadboard Plate	(LINOS 120x120mm)	1
Alt. Flat Mirror Mount	(M1-RQ)	-
Concave Mirror Mount	(M2)	2
Mounting Column 14 50mm		1
Mounting Column 14 80mm		7
Mounting Plate	(220x140-M)	1
Mounting Plate	(MB1545-M)	1
Angle Regulator	(MSRP01-M)	1
Angle Regulator	(PR01-M)	1
Rods 14 40mm		5
Rods 14 120mm		9
Source Slit		1
Post	(TR75-M)	1
Post	(TR100-M)	1
M3 Screw 10mm		+30
M4 Screw 30mm		+20
M6 Screw 10mm		+100
M6 Screw 30mm		+100
X95 250mm		2
X95 500mm		6
X95 750mm		4
X95 1000mm		3
X95 Clamping Carrier		10
X95 Corner Connector		4
X95 End Plate		8